

AN EXTENSIONAL MODE RESONATOR
FOR VIBRATION HARVESTING

By

JOHN M^c KAY YOUNGSMAN

A dissertation submitted in partial fulfillment of
the requirements for the degree of

DOCTOR OF PHILOSOPHY

WASHINGTON STATE UNIVERSITY
College of Engineering and Architecture

MAY 2009

To the Faculty of Washington State University:

The members of the Committee appointed to examine the dissertation of John M^c Kay Youngsman find it satisfactory and recommend that it be accepted.

David F. Bahr, Ph.D., Chair

Michael J. Anderson, Ph.D.

David P. Field, Ph.D.

M. Grant Norton, Ph.D.

ACKNOWLEDGEMENT

A dissertation is never accomplished by an individual. There is always a tremendous supporting cast. I have been very fortunate to be surrounded by incredibly supportive people. I would like to express my gratitude and appreciation to the following people for their efforts in helping me achieve the production of this work:

Professor David Bahr, my advisor, for accepting me into his group, providing sage advice, and giving me the opportunity to work on such an interesting project.

Professor Michael Anderson, committeeman, for the hours of assistance and direction in this work.

Professors David Field, and Grant Norton, my committee, for their time and interest in my work.

Dr. Dylan Morris for his inspiration and creation of the first prototype XMR.

Tim Luedeman, summer intern, for his outstanding assistance and dedicated work.

Bob Ames, my friend and golfing partner, who provided sanity checks through the last half of this work.

Finally, to Cheryl, Abby, and Max for their love and patience to endure my absence for much longer than originally planned.

Financial support was provided through the US Navy under a subcontract to an SBIR project with TPL Incorporated; contract number N68335-08-C-0098.

AN EXTENSIONAL MODE RESONATOR
FOR VIBRATION HARVESTING

ABSTRACT

By John M^c Kay Youngsman, Ph.D.

Washington State University

May 2009

Chair: David F. Bahr

In an effort to identify techniques for harvesting energy from ambient vibrations, a prototype device that utilizes stretching piezoelectric film to support a proof mass, with an adjustable support that allows the resonant frequency of the device to be easily altered has been developed. This extensional mode resonator (XMR) device is described by a model developed in this work that predicts the power that is harvested as a function of the frequency and amplitude of the external vibration, the elastic and piezoelectric materials properties, and the device geometry. The model provides design guidelines for the effects of device geometry and applied tension through an adjustable support that suggest a strong dependence on mechanical damping and a weak dependence on frequency, as opposed to a bending cantilever device. The model predictions are compared to experimental measures from multiple configurations of the prototype device for frequencies between 60 Hz and 180 Hz, and at accelerations between 0.1 m/s^2 and 25 m/s^2 . Up to 22 mW is generated from a device with a mass of ~82 g at

25 m/s² acceleration, and over the range of frequencies tested the power harvested at 4 m/s² is between 3 mW and 4 mW. The developed models are used as design tools for various configurations that are capable of over 100 mW at less than 3 m/s² in one case to another that can generate more than 10 mW at 1 m/s². Prototype configurations have been successfully tested as high as 80 m/s² with power generated on the order of 40 mW.

TABLE OF CONTENTS

ACKNOWLEDGEMENT.....	iii
ABSTRACT.....	iv
TABLE OF CONTENTS.....	vi
LIST OF TABLES.....	x
LIST OF FIGURES.....	xi
CHAPTER ONE.....	1
1 INTRODUCTION.....	1
1.1 Power Requirements.....	2
1.2 Principle of Piezoelectricity.....	3
1.3 Polymer Piezoelectric Materials.....	6
1.4 Conformation Effects.....	7
1.5 Poling Techniques.....	9
1.6 Review of Cantilever Type Devices.....	10
1.7 Stretching Mode.....	11
CHAPTER TWO.....	13
2 PVDF POLING AND TESTING TECHNIQUES.....	13
2.1 Introduction.....	13
2.2 Poling.....	13
2.3 Evaluating Phase.....	16

2.4 Measuring Compliance s_{11}^E	21
2.5 Measuring Piezoelectric Coefficient, d_{31}	27
2.6 Amplitude Measurements.....	31
2.7 Damping	33
CHAPTER THREE.....	39
3 XMR BASICS.....	39
3.1 Introduction	39
3.2 The Extensional Mode Resonator	41
3.3 Prototype Device Fabrication and Experimental Measures	43
3.4 Frequency Tunability	45
3.5 Power Results of the XMR.....	49
3.6 Conclusions	51
CHAPTER FOUR.....	52
4 MODEL DEVELOPMENT OF THE RXMR.....	52
4.1 Introduction	52
4.2 Dynamic Model.....	55
4.3 Electric Circuit Analysis and Energy Harvesting Capability	60
4.4 Prototype Device	63
4.5 Electrical Impedance	63
4.6 Mechanical Vibration and Power Output.....	64
4.7 Results	66

4.8 Mechanical Vibration and Power Output	68
4.9 Uncertainty Discussion.....	73
4.10 Conclusions	74
CHAPTER FIVE.....	75
5 EXCESS FILM MODEL DEVELOPMENT	75
5.1 Introduction	75
5.2 Geometric Effects.....	75
5.3 Development of Power Equations	79
5.4 Experimental Results of Excess Model.....	85
CHAPTER SIX	92
6 APPLICATIONS OF THE DEVELOPED MODELS TO DESIGN	92
6.1 Introduction	92
6.2 Matchbox Device	93
6.3 CD Jewel Case Device	97
6.4 ½ Pint Carton Device	102
6.5 Conclusions	106
CHAPTER SEVEN.....	108
7 CONCLUSIONS	108
REFERENCES	113
APPENDIX	117
A1 Materials Properties Information.....	118

A2 RXMR Excess Model Development Equations from *Mathematica*..... 122

A3 Composite Material Thickness Derivation 151

A4 Uncertainty Analysis 155

LIST OF TABLES

Table 1 Typical physical, piezoelectric, and pyroelectric properties of various materials [34]	7
Table 2 Results from impedance sweep curve-fit	35
Table 3 Device geometry constants and PVDF film properties.	63
Table 4 Configuration, impedance measurements, and theoretical predictions for nominal natural frequency of $f_n=120$ Hz, 150 Hz, and 180 Hz. (119 μm film)	67
Table 5 Configuration, impedance measurements, and theoretical predictions for nominal natural frequency of $f_n=70$ Hz, 80 Hz, and 90 Hz. (28 μm film)	72
Table 6 Configuration, impedance measurements, and theoretical predictions for nominal natural frequency of $f_n=332$ Hz, 354 Hz, and 370 Hz. (119 μm film).	87
Table 7 Configuration, impedance measurements, and theoretical predictions for nominal natural frequency of $f_n=362$ Hz, and two at 370 Hz. (119 μm film).	89
Table 8 Predicted results for the matchbox device at various u_p dimensions and film thicknesses. Calculations assume a constant R_m value of 1.7 Ns/m.	97
Table 9 Predicted results for the CD jewel case device at various u_p dimensions and film thicknesses. Calculations assume a constant R_m value of 1.7 Ns/m.	99
Table 10 Predicted results for the CD jewel case device at various u_p dimensions from films of PZT on brass. Calculations assume a constant R_m value of 1.7 Ns/m.	101
Table 11 Predicted results for the 1/2 pint carton device at various u_p dimensions and film thicknesses. Calculations assume a constant R_m value of 6.5 Ns/m.	104
Table 12 Device performance for various prototype configurations.....	109

LIST OF FIGURES

Figure 1 Examples of noncentrosymmetric crystal structures [28].....	3
Figure 2 Schematic detailing the 31 and 33 mode of piezoelectric materials [29].....	4
Figure 3 Schematic detailing the composite structure of piezoelectric fibers embedded in an epoxy matrix with interdigitated electrodes configured to take advantage of the higher d_{33} coefficient of piezoelectricity [30].....	5
Figure 4 SEM image of a MEMS curved cantilever with an interdigitated electrode design to utilize the d_{33} coefficient [31].....	6
Figure 5 Stress strain curve for PVDF [33].....	7
Figure 6 Schematic depiction of the two most common crystalline chain conformations in PVDF: (a) tg^+tg^- and (b) <i>all-trans</i> . The arrows indicate projections of the $-CF_2$ dipole directions on planes defined by the carbon backbone. The tg^+tg^- conformation has components of the dipole moment both parallel and perpendicular to the chain axis, while the <i>all-trans</i> conformation has all dipoles essentially normal to the molecular axis [34].....	8
Figure 7 Schematic showing the random distribution of amorphous material and small crystallites in cast PVDF (top). Application of strain (middle) orients the crystallites along a single axis. Poling (bottom) aligns the dipoles of the crystallites [32].....	9
Figure 8 RXMR device. A proof mass is suspended by PVDF films which stretch rather than bend during vibratory motion. Adjustment screws change tension.	12
Figure 9 Cross section view of conical XMR.	12
Figure 10 Poling apparatus. Top left: hot plate with sample in dielectric bath. Top right: sample on conductive base and copper contact pad. Bottom: Bertran power supply and ammeter.	14

Figure 11 Current vs. time for the poling process of sample AM75 13B. Each step increase in current at time < 20 minutes represents a 50 V step in the applied field.	15
Figure 12 FTIR spectra from 28 μm Measurement Specialties film. The peak at $\sim 840\text{ cm}^{-1}$ indicates presence of β -phase. Peaks at ~ 615 and $\sim 763\text{ cm}^{-1}$ indicate α -phase.	17
Figure 13 FTIR spectrum from TPL, Inc. cast film. The peak at $\sim 840\text{ cm}^{-1}$ indicate β -phase while the broad peak below 700 cm^{-1} hides most information regarding α -phase.	18
Figure 14 FTIR spectrum from TPL, Inc. cast film sample AM75-21A.....	19
Figure 15 FTIR spectra for stretched (red) vs. unstretched (blue) PVDF-HFP 10% sample from TPL (AM75-49A).....	20
Figure 16 FTIR spectra for stretched (red) vs. unstretched (blue) PVDF-HFP 10% with 20 vol% PZT sample from TPL (AM75-13B).....	20
Figure 17 Stress vs. strain results from a DMA test on samples of 9 μm biaxial stretched PVDF film.	22
Figure 18 Linear region of stress vs. strain results from a DMA test on samples of 9 μm biaxial stretched PVDF film showing curve fit of samples.....	22
Figure 19 Zoomed in region of stress vs. strain results from a DMA test on samples of 9 μm biaxial stretched PVDF film showing a curve fit of the sample data that corresponds to the materials modulus.	23
Figure 20 Schematic of bulge test apparatus used for measuring film modulus.	24
Figure 21 Pressure vs. deflection data with curve fit of Measurement Specialties 28 μm film used to calculate film modulus.	25
Figure 22 Schematic of the force-deflection experiment using the 4-point bend apparatus.	26
Figure 23 Force-displacement measurement relationship of the RXMR used as a method to determine compliance. (Data file 10140816 corrected load plot.)	27
Figure 24 Schematic of d_{31} gravity test.	28

Figure 25 Schematic of d_{31} experiment using the bulge test apparatus.	30
Figure 26 Drawing of the electrode generated by the shadow mask used in the RMM d_{31} bulge test. .	31
Figure 27 Typical plot showing the displacement vs. acceleration of the mass and base. The displacements between the mass and base differ by more than an order of magnitude.	32
Figure 28 Plot showing the measured mass amplitude vs. base acceleration of the XMR at resonant frequencies of 152 Hz and 178 Hz.	33
Figure 29 Initial impedance sweep, $ Z $ vs. f , (left) and curvefit (right) of impedance data of the XMR device nominally tuned to 180 Hz.	34
Figure 30 Image of the XMR device with binder clips attached.	34
Figure 31 Impedance sweep, $ Z $ vs. f , (left) and curvefit (right) of impedance data of the XMR device after the attachment of additional mass.	35
Figure 32 Mechanical damping R_m vs. u_p+u_{xs} generated from data sets. Blue data are from 119 μm films, red data are from 28 μm films, diamonds are from a regular model device, triangles are from an xs -model device.	38
Figure 33 (a) Schematic of the displacement u of a rectangular string of non-deformed length $2l$, thickness h and width w (out of the plane of the figure) at the center by a force F . (b) Pre-tensioning two extensional elements by a rigid link of length $2u_p$. (c) Displacement of the link by an external force F by an amount Δu	42
Figure 34 (a) Section view of the XMR (b) Photograph of an assembled XMR device	44
Figure 35 Cross-sectional schematic of the XMR device driven by base excitation. In this schematic, the seismic mass has moved upwards relative to the base, causing the top piezoelectric membrane to shorten and the bottom membrane to lengthen. Continued vibratory motion causes the membranes to alternately lengthen and shorten [24].	45

Figure 36 Frequency response functions from a frequency-tuning experiment in which each symbol indicates the same adjustment position. Different experiments at each adjustment position have different shading. The adjustment was varied between the three positions in a random sequence. This demonstrates the reproducibility of the frequency tuning mechanism. 46

Figure 37 Resonant frequency, determined by the frequency response function, as a function of relative preloading displacement. The placement of the preloading screw at 212 Hz is an arbitrary datum. The solid line is a least-squares linear fit, and the dashed lines indicate a 95 % confidence interval [24]. 47

Figure 38 Compressive beam technique (a) schematic of technique (b) device under test [19]. 48

Figure 39 Magnetic assist by Challa *et al* (a) magnet configuration that increases the effective stiffness of the beam (b) magnet configuration that decreases the effective stiffness of the beam. (c) Device schematic showing positions of components [20]. 48

Figure 40 Schematic of Hu *et al* method to load a bimorph cantilever [54]. 49

Figure 41 Power vs. acceleration for the prototype XMR. 50

Figure 42 Power vs. acceleration of the prototype XMR at low acceleration amplitudes. 51

Figure 43 Schematic for mechanical function of the XMR device. 54

Figure 44 Schematic for electrical function of the device. 55

Figure 45 A free-body diagram for the mass m 56

Figure 46 Equivalent circuit diagram for the device (Equations (4.13) and (4.20)). 61

Figure 47 Measurement of electrical impedance and curve fit for circuit parameters R , L , C , C_o and k^2 64

Figure 48 Apparatus used to perform power output experiment from a controlled vibration source. .. 65

Figure 49 Transfer function vs. frequency of the XMR device. Peak indicates the resonant frequency of the oscillator. 66

Figure 50 Comparison of predicted power output vs. acceleration for the XMR configured with nominal natural frequencies of 120, 150, and 180 Hz..... 69

Figure 51 Power output vs. acceleration for the XMR across a broad range of frequencies. Device was constructed with 119 μm films..... 70

Figure 52 Power output vs. acceleration for the XMR configured with nominal natural frequencies of 40, 48, and 59 Hz. Device was constructed with 9 μm films. 71

Figure 53 Comparison of predicted power output vs. acceleration for the XMR configured with nominal natural frequencies of 70, 80, and 90 Hz. Device was constructed with 28 μm films. 72

Figure 54 XS model geometric configuration (left) unstrained configuration, (middle) static strained film due to u_p tension, (right) dynamic strained films due to base motion Δu 76

Figure 55 Plot of power function vs. u_{xs} . Acceleration normalized power variation with changes in excess film length for a device configured with 119 μm film, 82.3 g mass, and dimensions of $L_0= 22$ mm, $w= 24$ mm, and $u_p= 3.59$ mm. 81

Figure 56 Dimensionless term $RC_o\omega_n$ vs. u_{xs} . Variation of the $RC_o\omega_n$ term with additions to the film length..... 82

Figure 57 Resonant frequency response to changes in excess film length..... 82

Figure 58 Device stiffness vs. changes in excess film length. 83

Figure 59 Predicted frequency response of *xs*-model versus changes in u_{xs} at several values of u_p . (red (long dash): $u_p=3$ mm, green (short dash): $u_p=4$ mm, black (solid): $u_p=5$ mm) 84

Figure 60 Predicted frequency response of *xs*-model versus changes in u_p at several values of u_{xs} . (red (long dash): $u_{xs}=0$, green (short dash): $u_{xs}=10$ mm, black (solid): $u_{xs}=20$ mm) 85

Figure 61 Measured power vs. acceleration data with theoretical predictions for an *xs*-model device. 88

Figure 62 Measured power vs. acceleration data with theoretical predictions for an *xs*-model device. 89

Figure 63 Power vs. acceleration plot of *xs*-model device from two separate data runs. The dimension u_p is the same between the 354 Hz measurement and the 362 Hz measurement indicating potential

creep. Blue data set was taken approximately two weeks before the red set. Two different u_p settings generated 378 Hz data in the latter set. 90

Figure 64 Power vs. acceleration plot of *xs*-model device (blue) contrasted with the regular model (red). Mass and film thickness are the same. Film length is the significant variation between the two results. 91

Figure 65 Model of the matchbox size device..... 93

Figure 66 Front view of the matchbox device showing device configuration and clearance..... 94

Figure 67 Partial section view of the matchbox device..... 95

Figure 68 Predicted power vs. acceleration for the matchbox device showing performance from a device constructed with two sizes of PVDF film. Results of 31, 62 and 92 Hz are from 28 μm film, the remaining are from 119 μm film. 96

Figure 69 Model of the CD jewel case device. 98

Figure 70 Front view of the CD jewel case device showing device configuration and clearance. 98

Figure 71 Predicted power vs. acceleration for the CD jewel case device showing performance from a device constructed with two sizes of PVDF film. Results of 3.7, 5.6 and 7.4 Hz are from 28 μm film, the remaining are from 119 μm film. 99

Figure 72 Predicted power vs. acceleration for the CD jewel case device showing performance from a device constructed with PZT on brass foils. Results of 3.7 Hz (PVDF 28 μm film) and 8 Hz (PVDF 119 μm film) are shown for comparison. 101

Figure 73 Model of the 1/2 pint carton device designed with a copper mass and PVDF films. 102

Figure 74 Front view of the 1/2 pint carton device showing relationship between components. 103

Figure 75 Section view of the 1/2 pint carton device showing additional relations between components..... 103

Figure 76 Predicted power vs. acceleration for the 1/2 pint carton device showing performance from a device constructed with two sizes of PVDF film. Results of 62.4, 63.7 and 64.3 Hz are from 28 μm film, the remaining are from 119 μm film..... 106

CHAPTER ONE

1 INTRODUCTION

Improvements in wireless communication and sensing techniques, along with the reduction of power consumption in current microelectronics, have provided the opportunity for structural health monitoring systems. Although power consumption is low, battery life remains a critical factor in installation of distributed sensor networks. Techniques are under investigation that can charge batteries, super capacitors, or other storage mediums, as a means to extend the service life of installed networks. Solar power is ubiquitous; however it is not a universal solution. Ambient vibrations are available in many instances and provide the critical energy input for the piezoelectric class of materials.

Researchers are investigating vibration harvesting utilizing various self energizing techniques including electromagnetic in both a cantilever configuration [1-3] and single membrane form [4, 5], and piezoelectric, principally as cantilevers [6, 7]. A number of recent reviews discuss harvesting theory, techniques, and performance [8-11]. The frequencies and accelerations discussed in the aforementioned reviews typically focus on the available vibrations from common machinery and appliances. Infrastructure monitoring falls into different vibration spectra than the typical machinery installation because buildings and bridges are so much larger. While not exhaustive, spectra have been reported for small span bridges (including pedestrian walkways) in the 2-10 Hz range [12-15], large span bridges report typical resonant frequencies below 2 Hz [12, 15], and a 27 story apartment building ranged between 0.4 and 3.3 Hz depending on the wind.

A critical issue with most resonating harvesters is their best performance occurs at a single frequency or over a very narrow range. Therefore, many designs appear limited to fixed frequency or

known environments. Adjustable resonant tuning provides flexibility in a device and the opportunity to maximize power generation. Literature shows limited cases of resonant tuning and are described as external electrical control [16, 17], beam compression technique [18, 19], beam stiffness change through piezoelectric effect [18], beam stiffness change through magnetic field application [20], decoupling [21, 22] or frequency rectification [23], and this work on the extensional mode resonator [24].

1.1 Power Requirements

Wireless sensor nodes installed in remote or difficult access locations allow for continuous monitoring of structures and events. For example, sensors (strain gages) installed on the main cables of a suspension bridge can provide strain information of the cables during high winds. This information is critical to the health of the structure and safety of the public as the sensor may determine the bridge had been exposed to an unsafe stress condition. This type of sensor would require continuous operation or perhaps operation during wind storms only. Another recent example is the collapse of the 35W highway bridge in Minnesota on August 1, 2007. Preliminary findings from the NTSB suggest that during recent roadwork, the structure was subjected to an overload condition due to excessive construction materials and equipment on the bridge deck. This overload may have caused undersized gusset plates to fail [25].

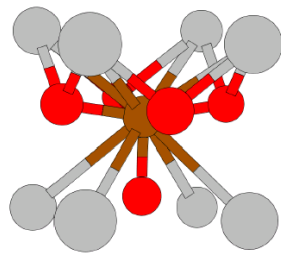
A critical problem to wide deployment is the issue of a suitable power source. Batteries have a limited life and require considerable time and energy to exchange. A larger concern is the installation that is either dangerous or no longer accessible for battery exchange. Solar energy can be used to recharge batteries or super capacitors and has many research dollars invested but a solution is required for installations that may not have or may not want solar exposure.

An example of the power requirements for a sensor node is presented in Ching *et al.* [5] in which a 100 μ W generator can operate a sensor, controller and transmitter system that measures and transmits temperature data to a receiver 25 meters away every 30 seconds. Charge is continuously

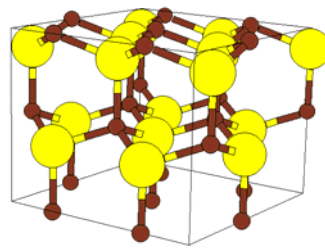
accumulated in a storage capacitor and used as required. A Navy SBIR program has called for energy harvesters that can provide 1 mW/cm^3 . The purpose of this study is to examine the piezoelectric and mechanical properties of certain piezopolymers and copolymers, some of which incorporate piezoceramic materials [26, 27], in an effort to optimize materials composition and tailor the properties for application to a novel vibration harvesting device.

1.2 Principle of Piezoelectricity

Certain crystalline materials exhibit the property of piezoelectricity. A requirement for the effect is a noncentrosymmetric crystal structure such that, under a strain, the center of charge of the positive and negative elements of the structure is separated. This creates a polarization or dipole moment. When a piezoelectric material (ZnO in Figure 1) is clad with electrodes, the effect of the dipole is to induce charge to move from one electrode surface of the crystal to the other electrode surface through a conductor. This is known as the direct piezoelectric effect. When the strain is cyclical, the mechanical energy from strain is converted into electrical energy that can be used to power electronics. The classification of a ferroelectric (BaTiO₃ in Figure 1) is that of a structure that has spontaneous polarization, i.e. the structure has charge separation without deformation and the magnitude of polarization changes with strain. So a ferroelectric is piezoelectric but the opposite does not hold.



BaTiO₃ structure



Wurtzite structure, ZnO

Figure 1 Examples of noncentrosymmetric crystal structures [28]

The complementary effect of piezoelectricity is the ability to displace a material with the application of voltage across the structure and is used in small speakers (i.e. cell phone and iPod) and

transducers. This is known as the converse piezoelectric effect and is equal in efficiency but opposite in direction to the direct effect. In this study it is utilized in the impedance measurement to extract electrical properties of the piezoelectric films. When the alternating voltage signal is put into the extensional mode resonator (XMR) device, the displacement of the piezoelectric films causes the device to resonate. The electrical properties of the film are assumed to be conserved in both modes of operation so the impedance test allows an efficient technique to capture the electrical properties of the films and device.

One of the principle measurements utilized in piezoelectric structures is the piezoelectric coefficient defined as d_{ij} where i and j refer to the direction of applied strain generated by a force and the direction of the electric field respectively detailed in Figure 2.

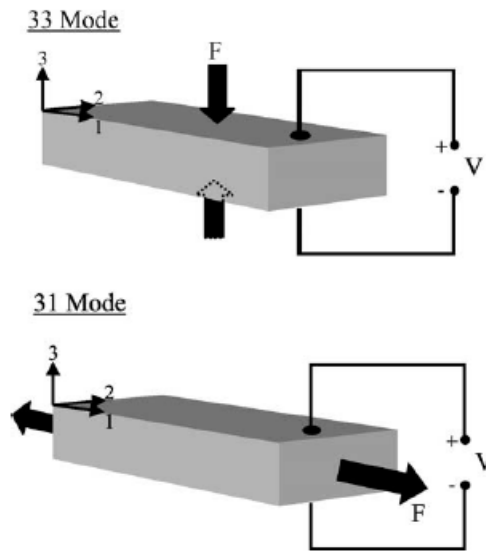


Figure 2 Schematic detailing the 31 and 33 mode of piezoelectric materials [29].

As stated above, the piezoelectric effect works in either direction. The direct piezoelectric effect generates a charge across the material when a strain is applied. The converse piezoelectric effect strains the material when a field is applied across the material. Because the effect is reversible, a single coefficient can be used to report the property.

The potential improvement in performance that the higher value of the d_{33} mode suggests has prompted some unique structures to try and utilize this mode. Two notable cantilever applications are

shown in Figure 3 and Figure 4. Both utilize an interdigitated electrode design on the surface of the cantilevers. The interdigitated design allows the field to lie in the 3 direction which is the same direction as the resulting strain. The composite structure in Figure 3 incorporates piezoelectric fibers embedded in an epoxy matrix. As the structure flexes, the fibers are stretched in the 1 direction. The arrangement of the electrodes induces the electric field along the 1 direction as well.

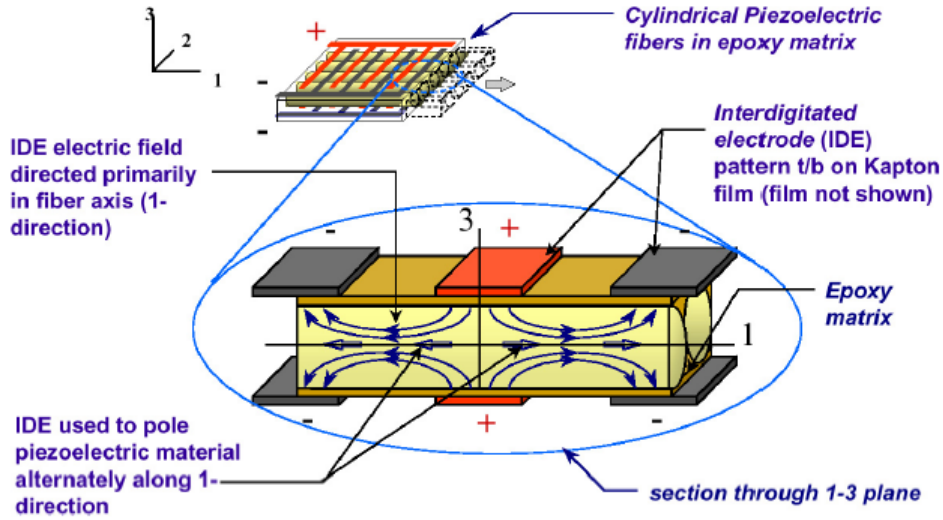


Figure 3 Schematic detailing the composite structure of piezoelectric fibers embedded in an epoxy matrix with interdigitated electrodes configured to take advantage of the higher d_{33} coefficient of piezoelectricity [30].

The structure depicted in Figure 4 undergoes a strain along the 1 direction when the radius of curvature changes due to excitation of the base. The interdigitated electrodes are configured to extract the charge induced along the 1 direction. It should be noted that the numbered directions of the reference frame are arbitrary and what is critical to understand is that d_{11} is equivalent to d_{33} as the directions are the same. However, d_{31} is not the same as d_{32} . This is an important distinction because often there is anisotropy in the materials or composite structure.



Figure 4 SEM image of a MEMS curved cantilever with an interdigitated electrode design to utilize the d_{33} coefficient [31].

1.3 Polymer Piezoelectric Materials

The polymer with the highest piezoelectric properties (Table 1) is that of polyvinylidene difluoride (PVDF), and its copolymers, although other polymer materials exhibit this property.

Polarization occurs due to separation of charge across the carbon backbone of the chain from either atoms or molecular groups [32]. While polymers have a much lower piezoelectric coefficient and smaller coupling than piezoceramics, the higher compliance (from 1/modulus) provides an opportunity to utilize these materials. The geometry of the XMR device benefits from the ability of polymer films to support tensile loads.

PVDF is also pyroelectric where temperature changes cause polarization. However, a large area is required for any significant change to performance in a harvester device. Temperature can affect the elasticity of the material which does impact device performance.

Figure 5 shows a typical stress strain curve for the PVDF material. It is seen that the material is capable of handling large strains relative to piezoceramic materials, with an elastic region of about 6%. Beyond this, a broad yield point is observed with a yield strength of approximately 43 MPa, consistent with the reported properties from Measurement Specialties.

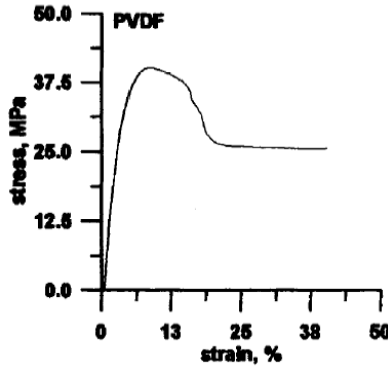


Figure 5 Stress strain curve for PVDF [33].

Table 1 Typical physical, piezoelectric, and pyroelectric properties of various materials [34]

Material	Piezoelectric coefficient, d (pC/N)	Pyroelectric coefficient, p ($\mu\text{C}/\text{K}\cdot\text{m}^2$)	Density, ρ (g/cm^3)	Elastic modulus, c (GN/m^2)	Dielectric constant, ϵ/ϵ_0	Electro-mechanical coupling coefficient, k (%)
PVF ₂ (β -phase)	$d_{31} = 20\text{--}30$ $d_{32} = 2\text{--}3$ $d_{33} = -30$	30–40	1.8	1–3	10–15	11
PVF ₂ (δ -phase)	$d_{31} = 10\text{--}17$ $d_{32} = 2\text{--}3$ $d_{33} = 10\text{--}15$	10–15				
Other polymers						
VF ₂ -trifluoroethylene copolymers	$d_{31} = 15\text{--}30$	30–40	~ 1.9		15–20	~ 20
Poly(vinyl fluoride)	$d_{31} = 1$	10	1.4	~ 1		
Poly(vinyl chloride)	$d_{31} = 1$	1–3	1.5	~ 4	3	
Nylon 11 (γ -phase)	$d_{31} = 3$	3	1.1	1.5	4	
Ceramics and single crystals						
Lead zirconate titanate	$d_{31} = 100\text{--}300$	50–300	7.5	80	1200	30
Barium titanate	$d_{31} = 80$	200	5.7	110	1700	21
Quartz	$d_{11} = 2$		2.7	80	5	10

1.4 Conformation Effects

Typical cast PVDF materials result in the α -phase chain conformation (Figure 6a) with the long polymer chains randomly oriented throughout the film [35]. This effectively contributes to the polarization neutrality of the bulk material as neighboring dipoles influence one another [36].

Mechanical drawing breaks down the original structure of the cast films and at high temperatures ($\sim 140^\circ\text{C}$) allow the chains to slide over one another while maintaining the α -phase conformation.

However, if the drawing occurs at an intermediate temperature ($\sim 50^\circ\text{C}$), there is not enough room for the chains to slide by one another and they are instead stretched, resulting in the β -phase [34, 36]. The

β -phase or all-*trans* phase, aligns the domains in a complementary fashion which maximizes the energy harvesting potential (Figure 6b). Drawing is one step in the process but does not align the dipole domains; it converts the alternate ordered domains to an ordered arrangement.

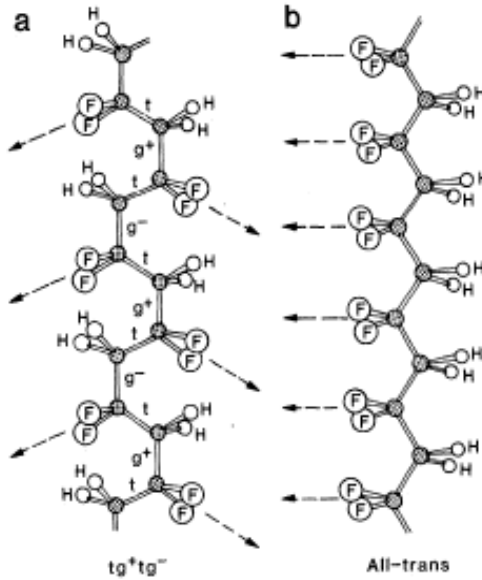


Figure 6 Schematic depiction of the two most common crystalline chain conformations in PVDF: (a) tg^+tg^- and (b) all-*trans*. The arrows indicate projections of the $-CF_2$ dipole directions on planes defined by the carbon backbone. The tg^+tg^- conformation has components of the dipole moment both parallel and perpendicular to the chain axis, while the all-*trans* conformation has all dipoles essentially normal to the molecular axis [34].

As stated above, the cast material is composed of randomly oriented α -phase material which also includes about 50% crystallites as shown in the top image of Figure 7. The crystallites are supported in the amorphous region and align along a single axis when mechanically stretched up to 500%. Finally, the sample is poled to align the dipoles of the crystallites in the same direction. This allows the material to generate a field across the surface when strained.

For the best performance, PVDF films should be drawn before poling. In the case where drawing is not feasible, literature suggests techniques to cast β -phase through alternate chemistries [35, 37, 38]. Additionally, the film can still be improved through poling at a modest temperature [34]. The purpose of poling is to align all the dipole domains along a common axis.

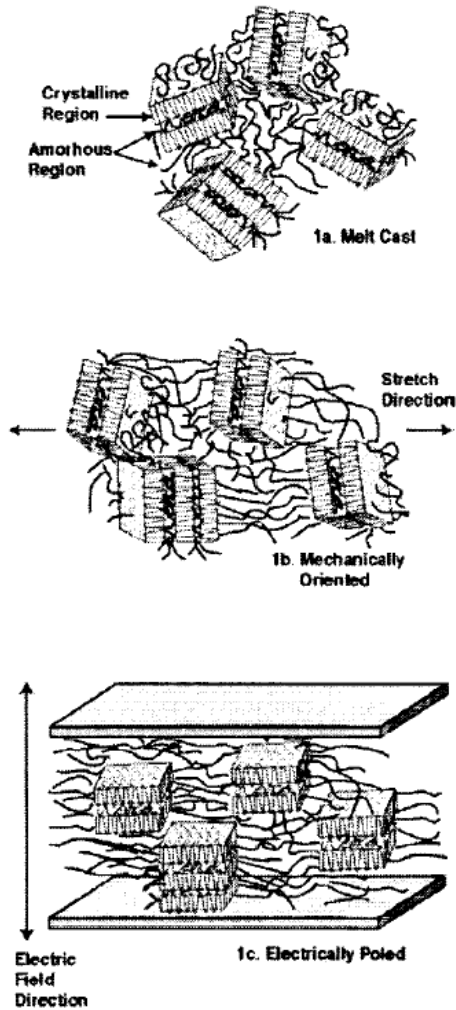


Figure 7 Schematic showing the random distribution of amorphous material and small crystallites in cast PVDF (top). Application of strain (middle) orients the crystallites along a single axis. Poling (bottom) aligns the dipoles of the crystallites [32].

1.5 Poling Techniques

The ability to maximize the piezoelectric effect relies on highly polarized materials. The chains of the PVDF polymer, as well as the individual grains of the incorporated piezoceramic, are arranged in a random distribution after casting. By subjecting the films to an elevated temperature (~80°C) in the presence of a large electric field (23kV/mm), the dipole moments of the components align. Cooling the film with the field applied locks in the dipole orientation [32, 34, 36, 39].

Relaxation of the structure occurs and is termed aging [32]. Typically this effect is completed after a

day. Poling can be accomplished most directly by applying a DC field across the film. This is an appropriate technique provided the film is of a modest thickness. Electric field is inversely proportional to the thickness of the sample so as the sample thickens, the voltage potential required may quickly surpass the limits of the power supply. An alternate technique called corona discharge poling may also be used. Because contact with the film is not necessary, corona discharge poling is effective for continuous processing of sheet stock and avoids the need of electrode deposition [32].

1.6 Review of Cantilever Type Devices

The conventional cantilever vibration energy harvester, which can be modeled as a spring mass damper system, is constrained to a very narrow frequency range in order to perform effectively. The equation for resonant frequency (ω_n) is [40]

$$\omega_n = \sqrt{\frac{k}{m}} = \sqrt{\frac{3EI}{ml^3}}. \quad (1.1)$$

The stiffness term, k , varies with the geometry of the beam (width, thickness, length, and moment of inertia, I) as well as the material from which the beam is constructed (E is the modulus of the material). Changes to the resonant frequency can be made by altering either the proof mass (m) or the stiffness of beam. These are not simple adjustments and as such, the typical cantilever harvester must be designed for an application rather than “tuned” for an installation. This requires the frequency and amplitude of the environmental vibration be known beforehand and the device designed to match the frequency.

Cantilevers are used primarily in one of two configurations. The first is as the oscillating member that moves a magnetic field across a coil [1]. The second is the oscillating member that supports a layer (or bilayer) of a piezoelectric material [29]. In this case the area of highest strain and maximum piezoelectric conversion occurs at the root of the beam where it joins the support structure. The stress diminishes linearly with length along the cantilever such that the tip has no stress [41]. As a result, a strain gradient forms and the efficiency of piezoelectric conversion declines. In an attempt to

more uniformly apply the strain, researchers have suggested a tapered cantilever where the root or attachment point is wide and tapers to the tip. The authors suggest this configuration will more uniformly distribute the strain along the length of the cantilever and realize a doubling of energy per unit volume of PZT (lead-zirconate-titanate, a common piezoceramic) thereby reducing production costs and real estate requirements in a device [6].

Another issue with the cantilever design is the reduction in power output as the frequency increases. The accepted model for the maximum power of the cantilever harvester as postulated by a number of researchers [1, 8, 11, 29, 42] is written in simple form as

$$|P| = \frac{m\zeta_e A^2}{4\omega\zeta_T^2}, \quad (1.2)$$

where A is the acceleration and ζ_e and ζ_T are the electrical and total dimensionless damping coefficients. The equation assumes that the natural frequency, ω_n , equals the driving frequency, ω . From this relationship it is apparent that as the driving frequency ω increases, the power generated is reduced. Initial experiments with the XMR device appear to contradict this relationship however, because stretching the films alters the stiffness, and therefore the mechanical damping (a component of ζ_T in the equation) of the device.

1.7 Stretching Mode

An advantage of the XMR device (Figure 8) is the ability to utilize stretching rather than bending mode for generating the piezoelectric effect. In the case of the rectangular version (RXMR), all strains are uniaxial and uniform. Because there is no strain gradient, as in the cantilever, the entire active area of the films produce power effectively. The conical model (Figure 9) is more complex and is composed of biaxial strain; principally a radial component through the film and a secondary tangential component. A strain gradient is also present through the film due to the change in cross sectional area, with the maximum strain occurring at the central hub and the minimum strain at the edge.

Piezopolymers typically have lower stiffness (higher compliance) and lower d_{31} than traditional

piezoceramics used in many harvesting techniques (Table 1), but that allows a much smaller force to displace the material. Piezoelectricity is generated by the strain of the material, and the voltage is a function of the piezoelectric coefficient, d_{31} . High compliance is beneficial, however low d_{31} limits the performance of a harvesting device. Incorporating high d_{31} piezoceramics into the piezopolymer should increase both the d_{31} and the stiffness. The tradeoff between performance, due to increased stiffness, and d_{31} in the piezocomposite materials will be examined.

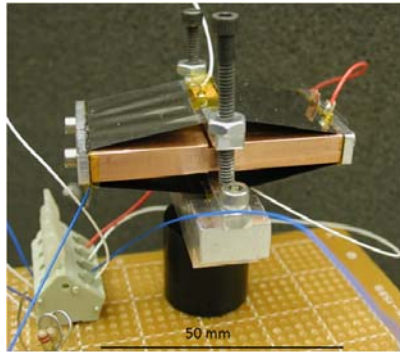


Figure 8 RXMR device. A proof mass is suspended by PVDF films which stretch rather than bend during vibratory motion. Adjustment screws change tension.

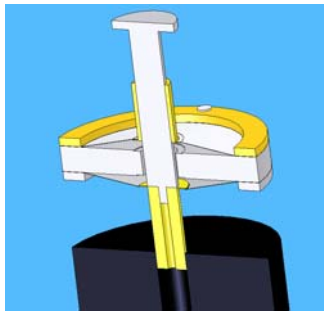


Figure 9 Cross section view of conical XMR.

CHAPTER TWO

2 PVDF POLING AND TESTING TECHNIQUES

2.1 Introduction

Through the course of this research a number of miscellaneous techniques were used to evaluate, measure, or otherwise condition the samples to achieve a particular objective. This chapter is broken into sections to address these techniques.

2.2 Poling

This section provides details on the poling procedure applied to samples received at various points in the research. The equipment is owned by the Center for Materials Research (CMR) and, with permission, was used when needed. The settings required were modified to suit the PVDF samples, these included temperature, voltage steps and dwell time.

All samples subjected to poling in this research use the DC electric field approach. This requires electrodes to be available on the film surfaces. For simplicity, gold electrodes are applied to both sides of the film using DC magnetron sputtering in a BOC Edwards Auto 306 Sputter System. In some cases, a shadow mask was used to define the geometry of the electrodes. It is imperative that no short circuits are present between the electrodes through either pits in the film or sputtered material that wraps around the edge. Prior to putting power to the films, a resistance and capacitance measurement are recorded to check for the short circuit condition. Additionally, it is best to trim the film to size after the electrodes are applied to avoid the second possibility above.

The process setup is shown in Figure 10. The sample was immersed in Fluorinert FC-40 (3M product), a dielectric solution to prevent premature breakdown of the film. The process was controlled by a *Labview* program running on a desktop computer. Inputs to the program include voltage step size, maximum voltage, step time, and maximum voltage dwell time.

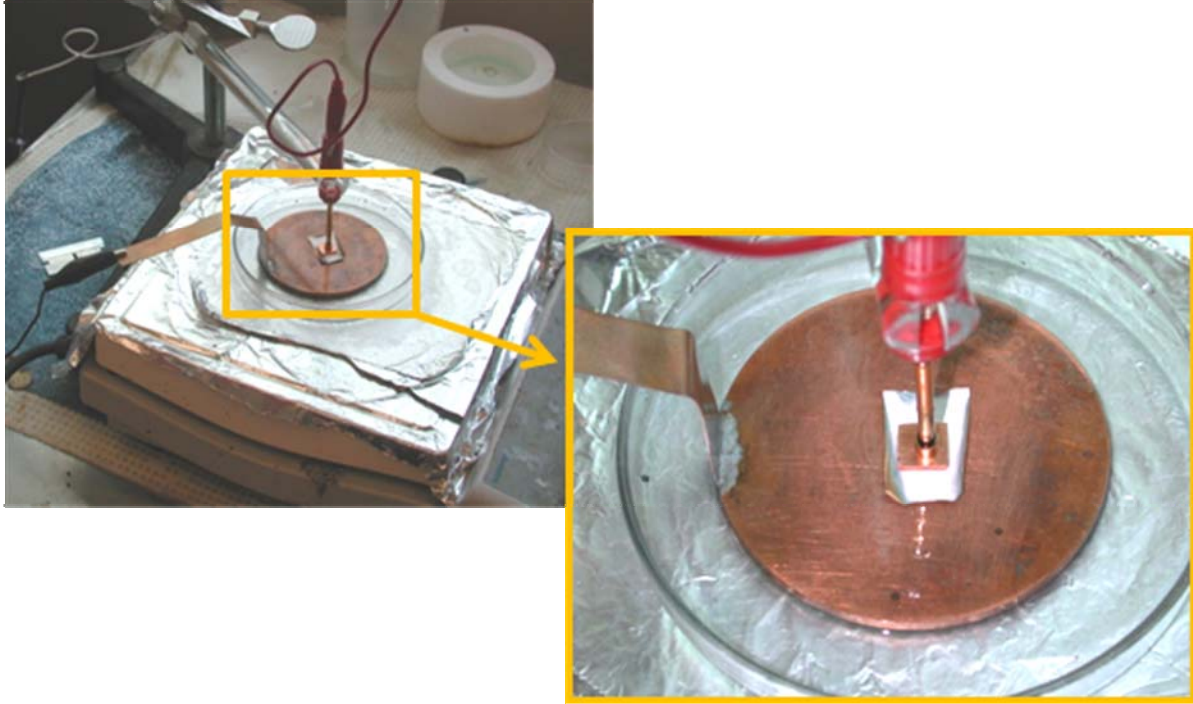


Figure 10 Poling apparatus. Top left: hot plate with sample in dielectric bath. Top right: sample on conductive base and copper contact pad. Bottom: Bertran power supply and ammeter.

The PVDF samples require a very large poling field. Literature suggests poling at just below the breakdown field, typically 30-120 kV/mm [36], however a practical poling field is limited to about 50 kV/mm [32]. The samples in this research were subjected to a field on the low end of the reported spectrum, 23 kV/mm, to avoid damage to the poling equipment. Using the sample thickness and applied field, calculations determined the power supply needed to supply up to 1100 V.

Figure 11 shows the poling profile of current versus time conducted on the films. The film was heated to $\sim 90^{\circ}\text{C}$, which is just below the Curie temperature T_c , while immersed in a dielectric solution bath to prevent breakdown. This additional energy allows the electric domains to reorder more easily. Each increasing step change in current represents a 50 VDC change in the applied field voltage with a peak (in this case) at 1050 VDC. The field was held through the following events: the current reduction leveled then dropped precipitously ($t=30$ minutes), reduction in current leveled off again ($t=40$ minutes), the heat was removed and the sample was allowed to cool to room temperature which further reduced the current. When the sample reached $\sim 40^{\circ}\text{C}$, the field was reduced at 50 VDC intervals every 30 seconds ($t=60$ minutes).

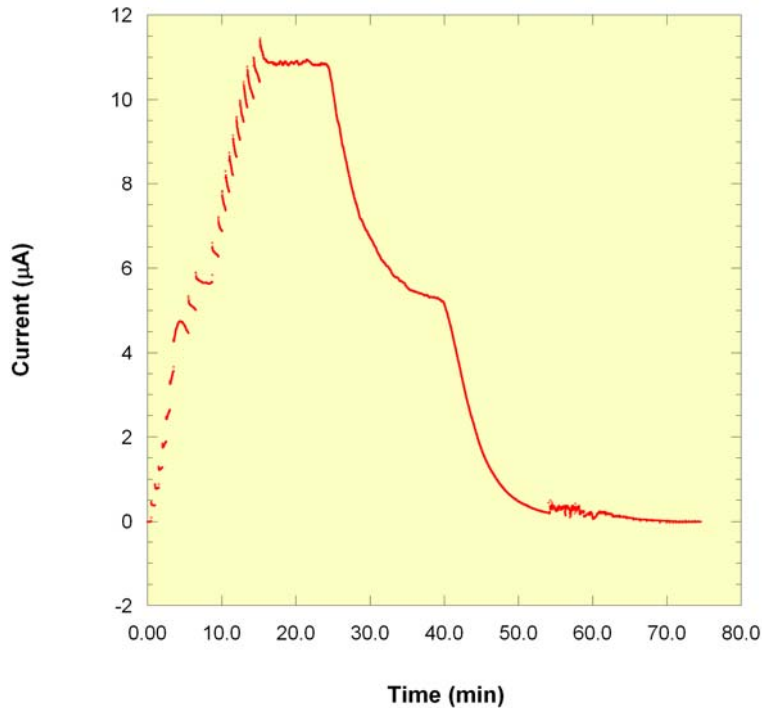


Figure 11 Current vs. time for the poling process of sample AM75 13B. Each step increase in current at time < 20 minutes represents a 50 V step in the applied field.

Although the technique used in this research is applicable to poling a single material such as PVDF or PZT, some of the samples were composites that included both PVDF and PZT. The d_{31} value of PVDF is opposite that of PZT, as such, a poling field would tend to polarize one material while it depoled the other. Zeng *et al* [43] describes a technique to pole both components which would

maximize the performance of a composite film when subjected to strain. The procedure involves poling the piezoceramic portion at a temperature above the polymer's Curie temperature for an extended period, up to 2 hours. The field is then removed and the sample is cooled to approximately 60°C and subjected to an AC poling field of 10 Hz. The field strength varied as a function of composition. This would be a useful technique to apply to some of the PVDF-PZT composite films used in this work.

2.3 Evaluating Phase

Fourier Transform Infrared Spectroscopy (FTIR), a non-destructive characterizing method, is used to determine the phase of the PVDF polymer films. The useful phase, in this case β -phase, is important to generate the piezoelectric effect. Cast PVDF films are typically α -phase and converted to β -phase through additional process steps. The measurement instrument used in this work is a Nicolet Nexus 870 FTIR ESP.

The FTIR technique measures a materials vibration response to an energy input. Laser light is applied to the sample which absorbs the energy. This energy absorption causes the molecules of the sample to vibrate. Analysis of the transmitted or reflected vibration frequencies is used to determine the types of bonds and atoms present. Modes include stretching, bending and torsion between neighboring atoms. Each atom pair and vibration mode has a specific vibration frequency. Spectra are typically reported in wave number (cm^{-1}).

A number of researchers have studied the PVDF and the PVDF-copolymer systems. Optical wave numbers of interest for phase determination are listed below [27, 37, 44, 45].

- 895 to 885 cm^{-1} : vinylidene ($>\text{C}=\text{CH}_2$)
- 840 and 510 cm^{-1} : β -phase PVDF
- 766, 795, 856, and 976 cm^{-1} : α -phase PVDF

Many of the films investigated were PVDF with HFP copolymer (hexafluoropropene). The addition of HFP is to produce β -phase rather than α -phase in the as cast condition. Another variant is the

incorporation of PZT particles into the PVDF copolymer. As pointed out in the previous chapter, this was done to try and improve the piezoelectric performance of the films. FTIR results of the PZT films contain a very broad peak below 700 cm^{-1} which inhibits the ability to identify the β -phase peak at 510 cm^{-1} .

The FTIR spectrum in Figure 12 is from a Measurement Specialties $28\text{ }\mu\text{m}$ film. Peaks show the presence of both α -phase (615 and 763 cm^{-1}) and β -phase (840 cm^{-1}).

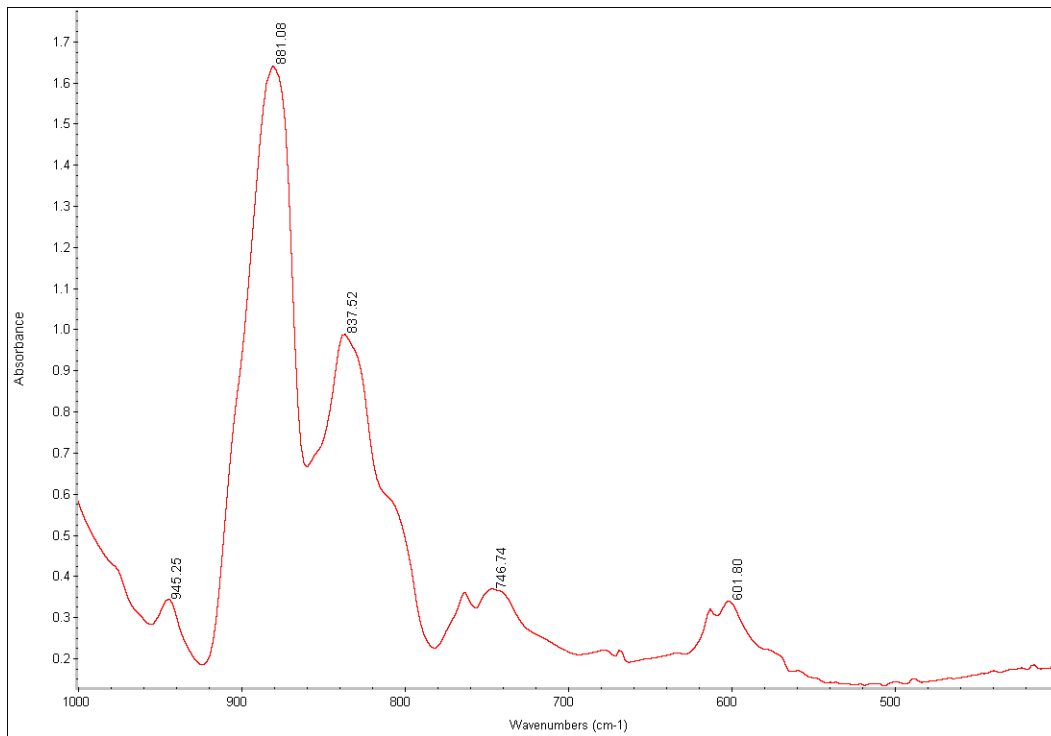


Figure 12 FTIR spectra from $28\text{ }\mu\text{m}$ Measurement Specialties film. The peak at $\sim 840\text{ cm}^{-1}$ indicates presence of β -phase. Peaks at ~ 615 and $\sim 763\text{ cm}^{-1}$ indicate α -phase.

The presence of α -phase would be expected as it would be difficult to convert all the material to β -phase. The dominant peak at $\sim 882\text{ cm}^{-1}$ indicates the presence of vinylidene groups which are composed of two carbon atoms double bonded with a pair of single bound hydrogen atoms and single bonds to two other atoms; in the case of PVDF they are fluorine.

A number of PVDF-copolymer samples were cast by TPL, Inc. and sent for evaluation. The intention was to develop a technique to tailor the piezoelectric properties of PVDF films by

incorporating copolymers and PZT. The spectrum shown in Figure 13 below is from sample AM75-13B #3 which is PVDF with 10% HFP and 20 volume % PZT. The broad peak due to the PZT is evident below 700 cm^{-1} and the sample shows a strong peak $\sim 840\text{ cm}^{-1}$ which would indicate the presence of β -phase. Unfortunately, the broad PZT peak obscures any information regarding the presence of α -phase.

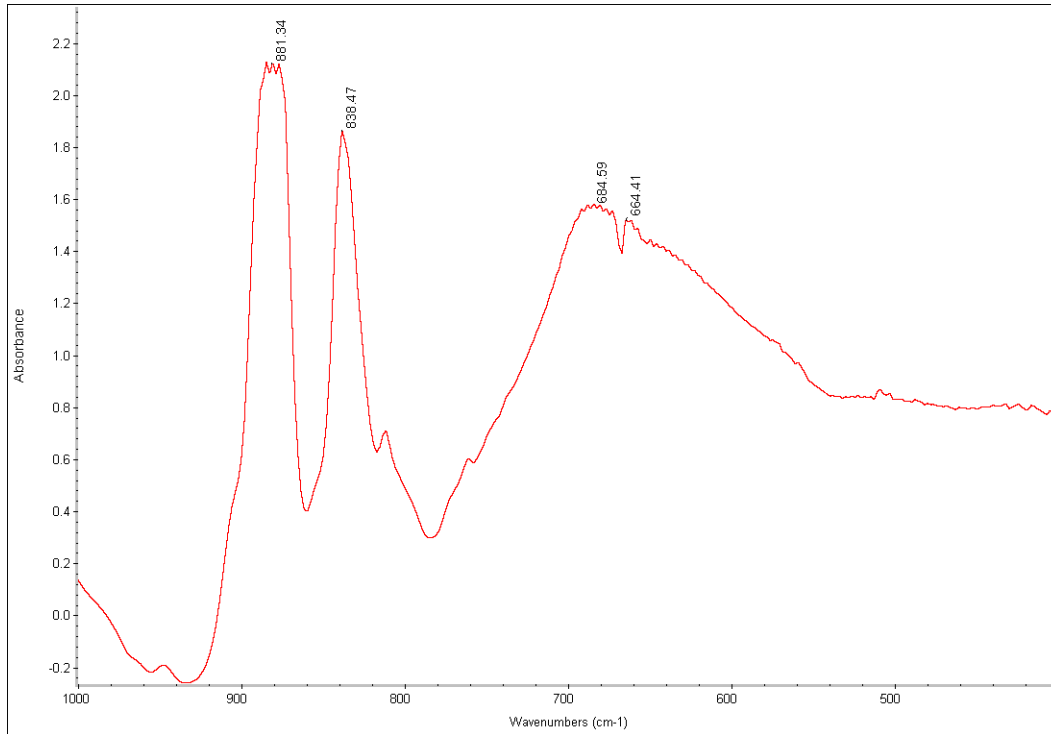


Figure 13 FTIR spectrum from TPL, Inc. cast film. The peak at $\sim 840\text{ cm}^{-1}$ indicate β -phase while the broad peak below 700 cm^{-1} hides most information regarding α -phase.

Another sample produced by TPL, AM75-21A, was cast without PZT. It is composed of PVDF with 10% HFP. Its spectrum is shown in Figure 14 and has a strong resemblance to the Measurement Specialties film in Figure 12 above. The TPL films presented here show β -phase in an as cast condition while the Measurement Specialties film was stretched to develop β -phase.

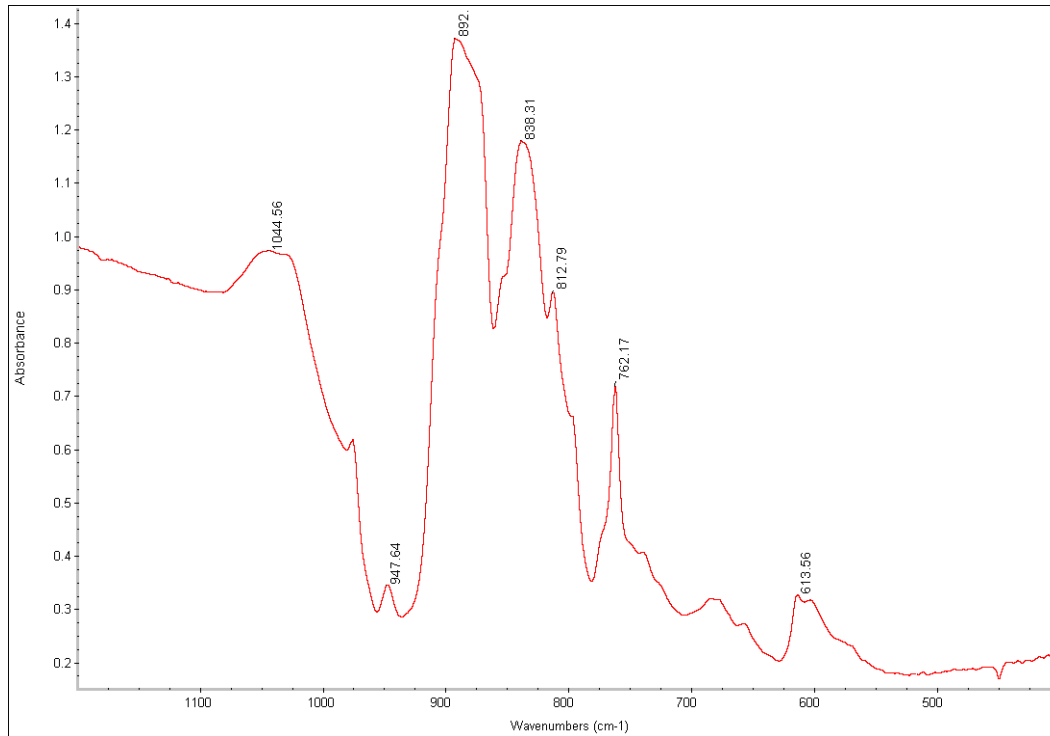


Figure 14 FTIR spectrum from TPL, Inc. cast film sample AM75-21A.

Samples were received from TPL that had been stretched as well. Unfortunately their technique was not able to stretch PVDF-PZT composite films; the samples tended to break before much strain was imposed. A technique tried at WSU was able to stretch films both with and without PZT. The technique involved rolling the samples in a pinch roller at room temperature. Sample AM75-49A, composed of PVDF-HFP 10%, was successfully stretched from 30.5 mm to 53 mm, a strain of 74%. The spectra are shown in Figure 15. The results show a small improvement in the β -phase indicator at 840 cm^{-1} .

improvement is seen, it is at a level much lower than literature suggests. Typically strain values to generate β -phase occur at levels around 400-500% [36].

2.4 Measuring Compliance s_{11} ^E

2.4.1 DMA Method

Dynamic Mechanical Analysis (DMA) is a useful technique to extract compliance data from materials. The DMA is a very sensitive instrument which simultaneously applies a static and dynamic load to a sample mounted in an insulated chamber then measures the resulting displacement. The compliance is calculated from the load and displacement data. The insulated chamber allows variations in temperature so that other measurements can be conducted such as loss modulus. This technique was used to determine whether a sample of 9 μm biaxial stressed film with no published data would have the same properties as the typical uniaxial stressed film from Measurement Specialties.

Two samples were cut from the parent sheet such that the test direction of the samples would be orthogonal. The samples were identified as longitudinal and transverse. Each sample was subjected to the same test conditions:

- Static load 2055 μN
- Dynamic load ramped from 1 μN to 323 μN
- Frequency 1 Hz
- Temperature constant~30°C

Results of the experiments are shown in Figure 17 below. The biaxial material was assumed isotropic, however the results depicted in the plot seem to contradict that assumption. The shift may also be explained by slippage of the longitudinal sample in the clamping jaws during the experiment. The samples were very thin and difficult to mount in the instrument. Slippage was also observed on another experiment.

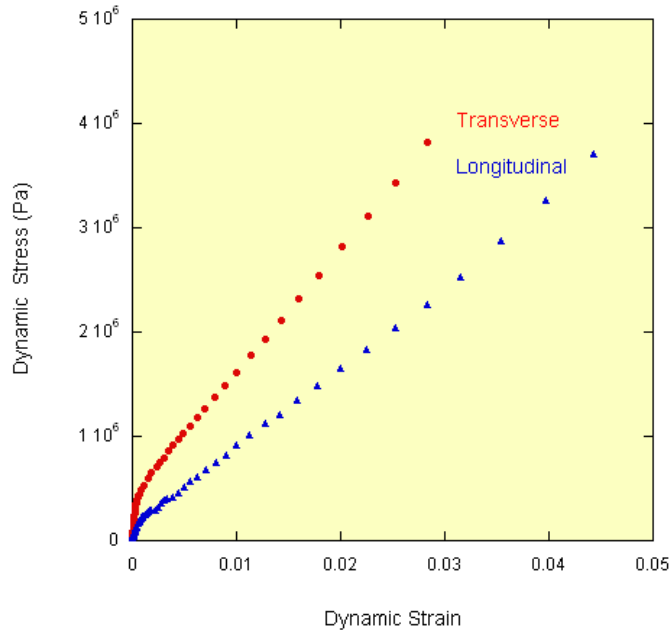


Figure 17 Stress vs. strain results from a DMA test on samples of 9 μm biaxial stretched PVDF film.

The shape of the curves are similar, with very steep sections near the origin that bend to a wide linear region with a slope that matches the reported 180 MPa tensile strength of biaxial PVDF [46]. A curve fit of the linear region is shown in Figure 18 with a slope of ~120 MPa.

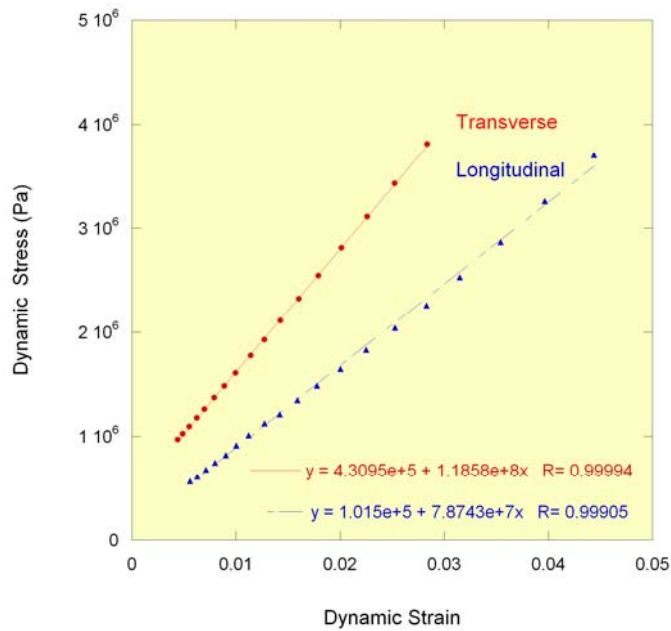


Figure 18 Linear region of stress vs. strain results from a DMA test on samples of 9 μm biaxial stretched PVDF film showing curve fit of samples.

The plot is consistent with the events in the experiment. As the stress is increased, the sample reaches the elastic limit and then begins to deform. Figure 5 shows a broad peak at the elastic limit for PVDF and that is assumed to explain the length of the linear portion in Figure 18.

Close examination of the results near the origin are shown in Figure 19 which captures the data at very low strains. The curve fit for the transverse sample is ~1.2 GPa which is somewhat lower than the reported Young's modulus of 2 GPa for a biaxial sample [46].

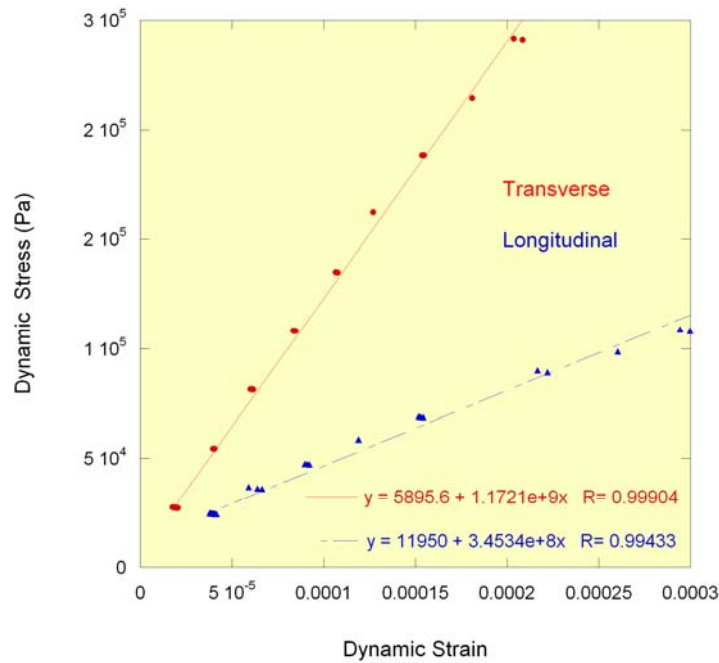


Figure 19 Zoomed in region of stress vs. strain results from a DMA test on samples of 9 μm biaxial stretched PVDF film showing a curve fit of the sample data that corresponds to the materials modulus.

Overall, the technique is useful for exploring the properties of the PVDF films. Caution must be used when mounting the samples and thicker samples may provide better results.

2.4.2 Bulge Testing

In bulge testing, a uniform stress is applied to a thin film material by introducing a pressure gradient on the two faces of the film. Figure 20 is a schematic of the test apparatus. The film (gray rectangle) is centered and adhered to a rigid puck (blue circle) that contains a rectangular feature (blue dashed line) with an aspect ratio (l/w) greater than 5. The puck is mounted to a bellows apparatus that applies vacuum to one side of the film through the slot feature. The vacuum causes the film to deflect

which is measured with a laser vibrometer centered over the film. Through the geometry restriction, the Rectangular Membrane Method (RMM) limits the strain to a uniaxial state [47]. The strain developed in the film through the pressure deflection is written as:

$$\varepsilon_1 = \frac{2\delta^2}{3a^2} \quad (2.1)$$

where ε , δ and a are the strain, center deflection of the film, and one half the side length of the short side of the film, respectively.

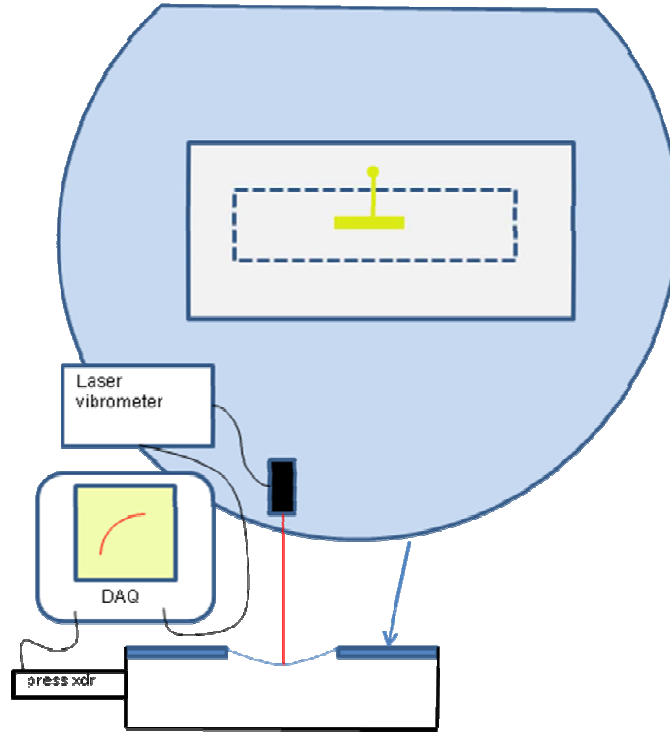


Figure 20 Schematic of bulge test apparatus used for measuring film modulus.

The modulus of the film is determined by curve fitting the pressure-deflection data to the following equation:

$$P(x) = C_1(x - x_{offset}) + C_2(x - x_{offset})^2 - P_{offset} \quad (2.2)$$

$$C_1 = \frac{3.4\sigma_0 t}{a^2}$$

$$C_2 = \frac{1.82E_B t}{a^4}$$

where P and x are the measured pressure and deflection. Coefficient C_1 has units $\text{kPa}/\mu\text{m}$ while C_2 has units of $\text{kPa}/\mu\text{m}^3$. The *offset* terms allow for corrections to be inserted if the pressure-deflection curve does not track through the origin [48]. Modulus is determined by solving the C_2 equation for E_B

$$E_B = \frac{C_2 a^4}{1.82t} \quad (2.3)$$

and substituting the known and measured values. The pressure-deflection curve shown in Figure 21 results in a modulus of 3.02 GPa. Measurement Specialties publishes a range for this value between 2-4 GPa.

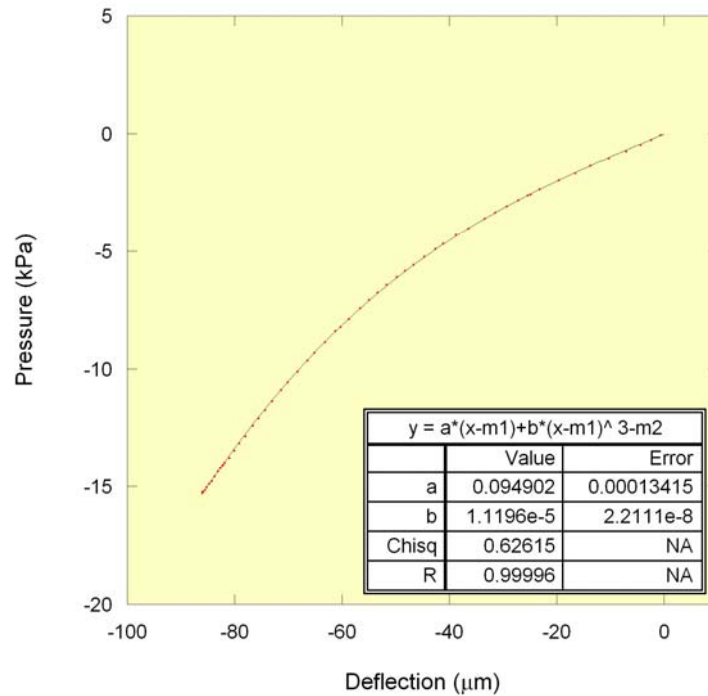


Figure 21 Pressure vs. deflection data with curve fit of Measurement Specialties 28 μm film used to calculate film modulus.

2.4.3 Force Deflection Measurement

The force-deflection experiment conducted with the 4-point bend apparatus provides another means to measure the compliance of the film elements. The apparatus is designed to measure force (in Newtons) through a transducer head, while it steps the head at fixed intervals of distance and time.

The device under test is assumed to be a simple mass-spring system so it obeys the following relationship:

$$F_{\delta} = s\delta \quad (2.4)$$

where s is the spring stiffness and δ is the displacement. Equation (2.5) calculates the device stiffness using a relationship between the device geometry and materials properties. The equation is used here but developed in detail in Chapter 4.2.

$$s = \frac{4wh}{s_{11}^E} \left(1 - \frac{1}{\left[1 + \left(\frac{u_p}{L_0} \right)^2 \right]^{\frac{3}{2}}} \right) \frac{1}{L_0} \quad (2.5)$$

The terms w , h , and L_0 , refer to the film width, thickness and non-deformed length while u_p is a pretensioning dimension. The material compliance is represented by s_{11}^E .

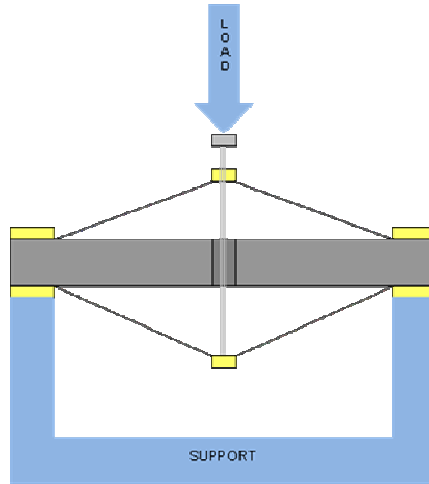


Figure 22 Schematic of the force-deflection experiment using the 4-point bend apparatus.

Solving Equation (2.5) for s_{11}^E and substituting the other geometric parameters with the device stiffness result from the force-deflection experimental plot, shown in Figure 23, returns a value of $1.15\text{E-}9 \text{ m}^2/\text{N}$ for the material compliance. This value is about an order of magnitude higher than the reported value of $3.65\text{E-}10 \text{ m}^2/\text{N}$ from Measurement Specialties.

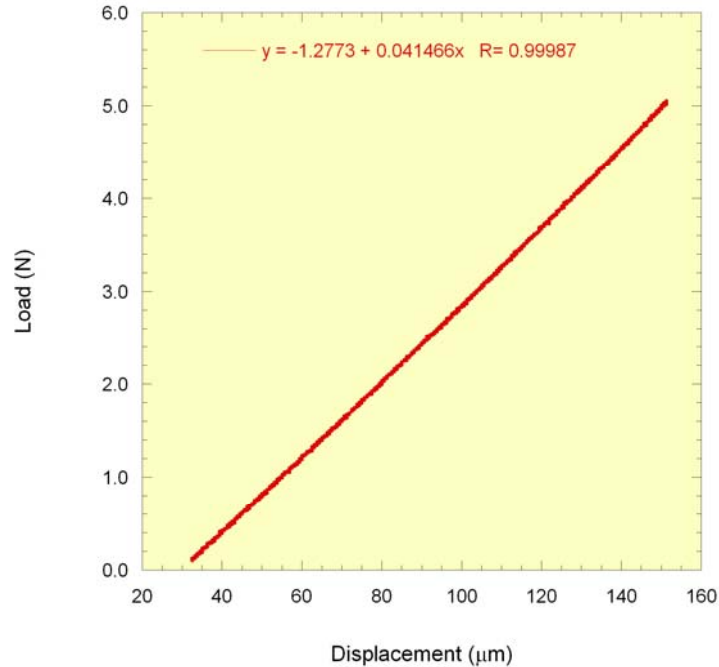


Figure 23 Force-displacement measurement relationship of the RXMR used as a method to determine compliance. (Data file 10140816 corrected load plot.)

2.5 Measuring Piezoelectric Coefficient, d_{31}

The piezoelectric coefficient, d_{31} , is calculated experimentally by measuring the charge accumulated on the electrode surface of the film during an applied stress. An electrometer, which measures charge (in coulombs), is connected across the films. When stress is applied to the film, the dipoles in the film change. This induces the charge to move from the electrode on one side of the film to the electrode on the other side of the film. The conduction pathway is through the electrometer which then provides a measure of the charge transported. Two techniques are detailed in the following sections that include a straightforward gravity test and a more controlled test using the bulge test apparatus.

2.5.1 Gravity Test

Figure 24 below is a schematic of the d_{31} gravity test. In the test, the film is stressed by the alternate application of a load onto the mounted film. The film is attached to a frame by the upper clamp while a lower clamp is attached to the other end of the film. The mass is connected to the lower

clamp by a string. The mass is raised and lowered to load and unload the film. Charge transfer between the electrodes is measured by the electrometer with each load application.

The value for d_{31} is calculated using the expression [32]

$$d_{31} = \frac{Q/A_e}{mg/A_x} \quad (2.6)$$

where Q is the measured charge transfer, m is the mass, g is gravity, A_e is the electrode area and A_x is the cross sectional area of the film.

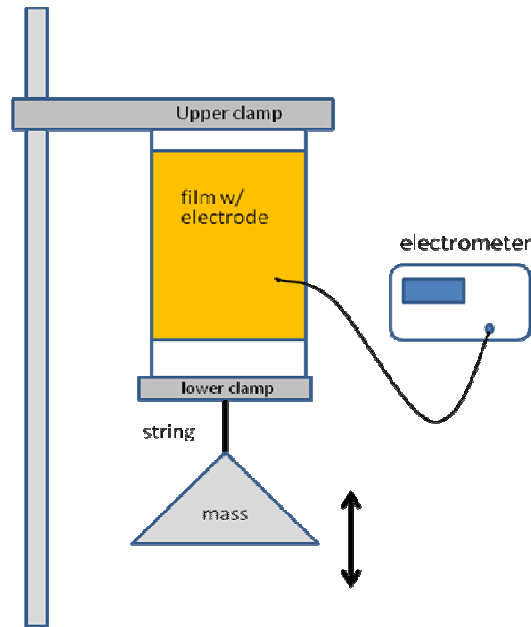


Figure 24 Schematic of d_{31} gravity test.

Samples of commercially available film from Measurement Specialties, with a published d_{31} value of 22 pC/N, were evaluated and produced values of $d_{31}=20$ pC/N. As a consequence, this film was used as a standard for evaluating performance of the apparatus when evaluating other film samples. Measurements conducted on d_{32} resulted in a similar confirmation of published values for the Measurement Specialties product.

2.5.2 Bulge Testing

As stated above, the piezoelectric coefficient, d_{31} , is calculated experimentally by measuring the charge transfer between the electrodes of the film during a stress cycle. The gravity test provides

an easy, although low precision, technique of measuring d_{31} while the bulge test apparatus provides a more controlled method to stress the films. An electrometer, which measures charge (in coulombs), is connected across the films. When stress is applied to the film, the dipoles in the film change. This induces the charge to move from the electrode on one side of the film to the electrode on the other side of the film. The conduction pathway is through the electrometer which then provides a measure of the charge transported.

The experimental measures are used with some geometric parameters of the film element in the following equation [47]:

$$d_{31} = \frac{3}{2} \frac{Q \left[(1 - \nu^2) a^2 \right]}{E_f h^2 A} \quad (2.7)$$

where Q , ν , a , E_f , h , and A are the measured charge, Poisson's ratio, half the short side length of the film, measured Young's modulus, film thickness and the electrode area respectively. The geometric values can be measured while the Poisson ratio can be found in literature. The bulge test apparatus provides the measures for charge and modulus as described in Section 2.4.2. Figure 25 below is a schematic detailing the experimental apparatus for measuring d_{31} with the bulge test apparatus. The setup is the same as that used for measuring compliance but includes the electrometer.

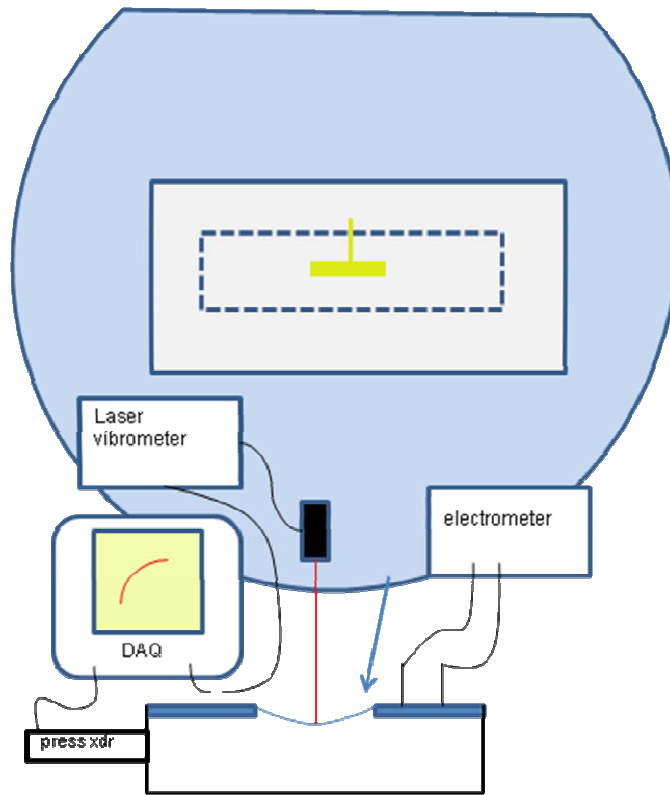


Figure 25 Schematic of d_{31} experiment using the bulge test apparatus.

The rectangular membrane method requires the length/width ratio of the electrode to be greater than 5 [47]. In keeping with this constraint shadow masks were constructed in order to define the electrode on one side of the film (see Figure 26). While the experiments were able to produce satisfactory results in compliance measurements, the d_{31} measures were less successful. Use of Equation (2.7), the pressure-deflection plot from Figure 21, and charge measurements from the electrometer resulted in $d_{31}=4.78$ pC/N which is much lower than the published value of ~ 22 pC/N. This may be attributed to the partial depolarization of the films during the mounting step as the wax used to mount the films melts at the Curie temperature of the PVDF material. This results in minimal charge transfer when strained. Consequently, the mounting was done using lacquer (clear fingernail polish) which resulted in a very thick adhesion layer that caused the films to sag.

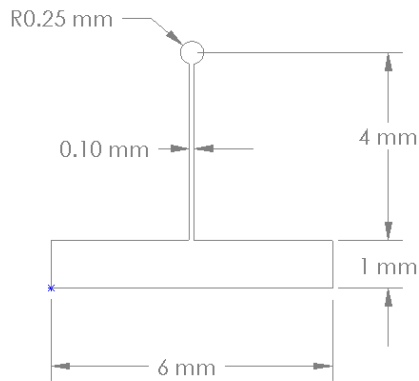


Figure 26 Drawing of the electrode generated by the shadow mask used in the RMM d_{31} bulge test.

Another source of error arose with centering the laser vibrometer on the sample at a region that would reflect an adequate signal. As the film was drawn down (with vacuum) into the puck feature, the concave surface of the film would tend to reflect the laser signal away from the detector reducing the signal strength. Additionally, the film surfaces were rough which caused the sputtered gold electrode material to reflect poorly. Although this would provide a more precise measure of d_{31} , there are issues that must be overcome before the technique is effective.

2.6 Amplitude Measurements

This section describes an experiment to measure the displacements of the base motion of the XMR and the displacement of the mass due to inertial motion. The displacements were measured using a laser vibrometer with small pieces of a polished silicon wafer attached to the frame and mass to act as reflectors. The XMR was driven at several resonant frequencies. Figure 27 shows the typical results for a displacement versus acceleration experiment. In this particular case the difference between the base and mass displacement is featured. This demonstrates the importance of operating an oscillating device at resonance: the very small base motion causes very large excursions of the resonant device. This results in larger strains in the compliant films which produce power in proportion to the strain.

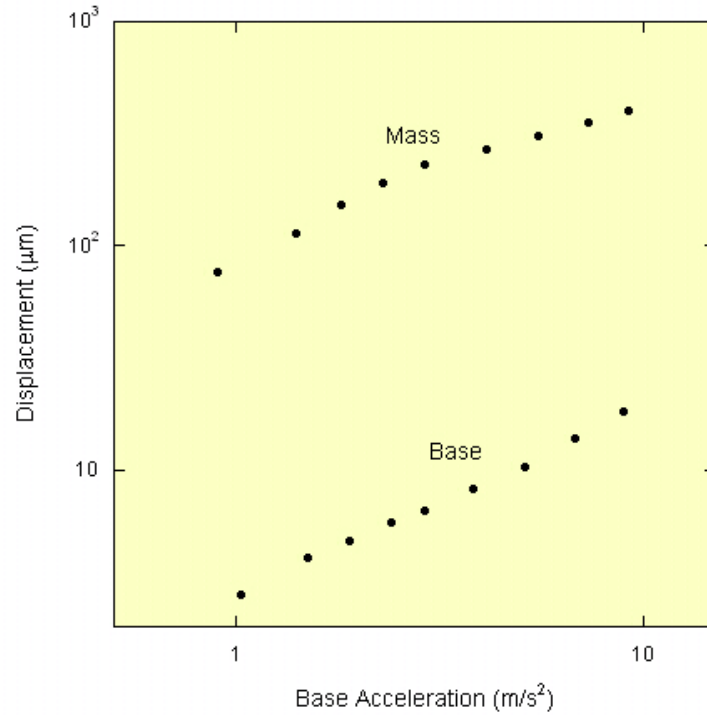


Figure 27 Typical plot showing the displacement vs. acceleration of the mass and base. The displacements between the mass and base differ by more than an order of magnitude.

Figure 28 shows the mass amplitude versus base acceleration at resonant frequencies of 152 Hz and 178 Hz. The interesting feature is the similarity in this plot to the power versus acceleration plots shown elsewhere. This indicates that power roll-off and limitation is due to reductions in vibration amplitude rather than a reduction in piezoelectric conversion.

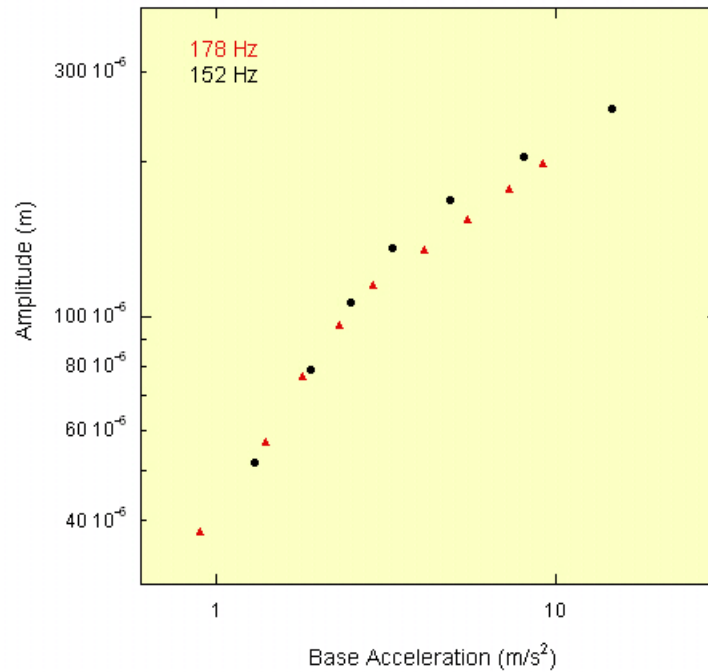


Figure 28 Plot showing the measured mass amplitude vs. base acceleration of the XMR at resonant frequencies of 152 Hz and 178 Hz.

2.7 Damping

At one point, the question of the effect of a mass change on device performance at a constant geometry was asked because of an assumption of constant mechanical damping. Before investing a lot of time on design and manufacture for a variable mass XMR, the following experiment was conducted to see if there was any change to the damping term.

Experiment

The hypothesis is that with an unchanged geometry, the change in mass should not affect mechanical damping. From the model development and mechanical analogue presented in Chapter 4, and the equivalent electrical circuit parameter R , the damping term R_m is defined by the relationship $R_m = R\Psi^2$, where Ψ , an electromechanical coupling term, is entirely composed of materials properties and geometry terms.

An impedance sweep was measured on the XMR tuned nominally to 180 Hz. The sweep and subsequent *Matlab* curve fit are shown Figure 29.

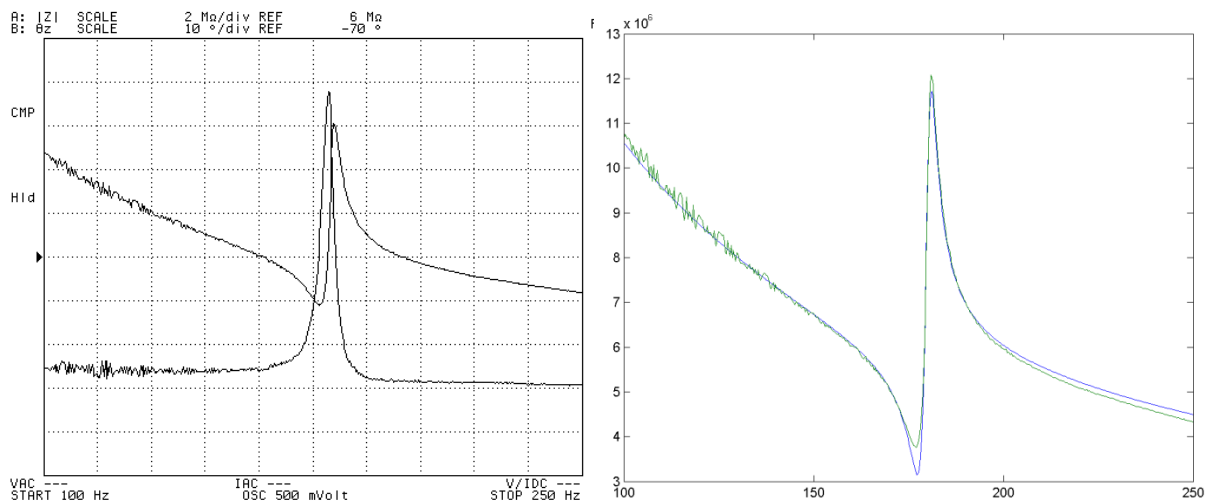


Figure 29 Initial impedance sweep, $|Z|$ vs. f , (left) and curvefit (right) of impedance data of the XMR device nominally tuned to 180 Hz.

An easy method to add additional mass was to affix large binder clips onto the ends of the XMR as shown in Figure 30. The total increase in mass was ~ 51.5 g. The clips were carefully attached to ensure symmetry in order to minimize a significant change in the moment about the center of mass.

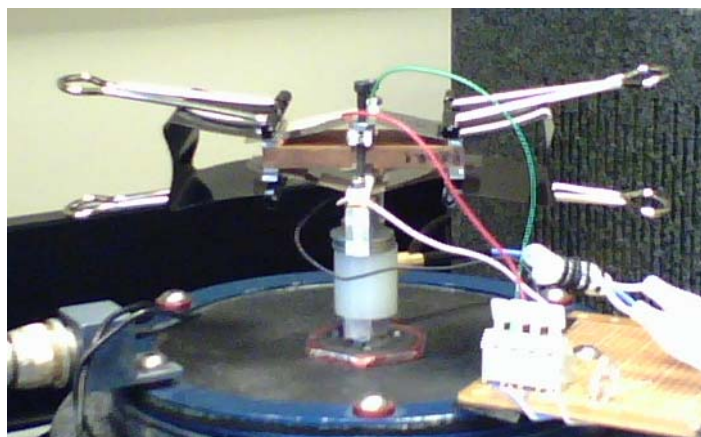


Figure 30 Image of the XMR device with binder clips attached.

After affixing the clips, another impedance sweep was taken. The results are shown in Figure 31.

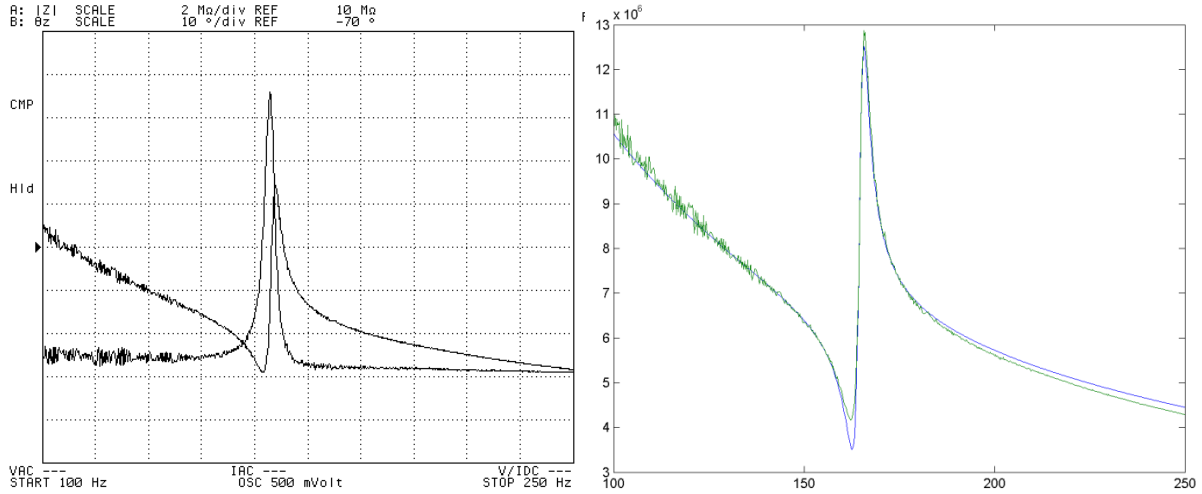


Figure 31 Impedance sweep, $|Z|$ vs. f , (left) and curvefit (right) of impedance data of the XMR device after the attachment of additional mass.

Comparing the plots in Figure 29 with the plots of Figure 31, the expected shift in frequency is apparent. The fit (blue line) to the data (green line) seemed to be less satisfactory than fits conducted on prior data sets, however it appeared to be consistent through both tests. The curve fit parameters are shown in Table 2.

Table 2 Results from impedance sweep curve-fit.

Parameter	XMR	XMR + 52 g	% Change
C_o	1.45E-10	1.45E-10	0.1
R	4.25E+06	4.82E+06	13.4
L	2.23E+05	2.95E+05	32.3
C_m	3.58E-12	3.22E-12	-10.1
k^2	0.024	0.022	-10.0
f_n	178	163	-8.3
Ψ (elec)	6.06E-04	6.74E-04	11.1
s (elec)	1.03E+05	1.41E+05	37.4
R_m (elec)	1.6	2.2	40.0
Ψ (geo)	7.53E-04	7.53E-04	0.0
s (geo)	1.31E+05	1.31E+05	0.0
R_m (geo)	2.4	2.7	13.4
C_m (geo)	4.3E-12	4.3E-12	0.0
Q	58.4	62.9	7.8

(elec) indicates values from impedance data using $\Psi^2=m/L$, $s=\Psi^2/C_m$ and $R_m=R\Psi^2$
 (geo) indicates values from geometry using equations for s and Ψ below

Analysis

The additional 52 g mass resulted in a 13% increase in R , and according to the mechanical-electrical relationship from the model would suggest that the mechanical damping has increased. Now consider the other terms, L and C_m . The mechanical analogs are $L = m/\Psi^2$ and $C_m = \Psi^2/s$. One would expect a change to L , as the mass has changed but geometry has not, and results indicate a change of 32%. The change to C_m is 10%, however one would not expect a change to this value as the assumption was that s and Ψ would remain constant with geometry. The model equations for the terms s and Ψ do not contain a mass term anywhere.

Frequency is calculated in the curve fit as $f_n = 1/2\pi\sqrt{LC_m}$, however frequency is also defined as $f_n = \sqrt{s/m}$. From the assumption of constant device stiffness, s , the following relationship should be true: $f_1^2 m_1 = f_2^2 m_2$ where the subscripts indicate the two test conditions. The initial mass was 82 g. The additional mass added was 52 g, a 63% increase. Substituting values produces:

$$(178^2)(82) = 2.6E6,$$

$$(163^2)(82 + 52) = 3.6E6.$$

The significant inequality between the results strongly suggests that s did not remain constant with the additional mass.

The following equations for s and Ψ are developed in detail in Chapter 4 but are placed here for convenience:

$$s = 4 \frac{wh}{s_{11}^E L_o} \left\{ 1 - \frac{1}{\left[1 + \left(\frac{u_p}{L_o} \right)^2 \right]^{3/2}} \right\}, \text{ and } \Psi = 2 \frac{d_{31} w u_p}{s_{11}^E L_o} \frac{1}{\left[1 + \left(\frac{u_p}{L_o} \right)^2 \right]^{1/2}}.$$

Using the mechanical analog from the impedance result ($\Psi^2 = m/L$) provides a means to calculate the coupling term, Ψ . The result was used to find s and R_m . Inspection of the geometric equation for Ψ indicates a dependence on geometric terms and materials properties, namely, compliance and piezoelectric coefficient. The mass is known and the inductance is measured, however the coupling term does not remain constant. The two terms that can change (because geometry did not change) in Ψ are d_{31} and s_{11}^E . The calculation of C_m using Ψ and s from the electrical measures returns essentially the measured value. This may be good in that Ψ and s are accurate or it may indicate that this relationship is used to derive the values. Because the experiment was conducted with constant geometry, using the relationship for $C_m = \Psi^2/s$ and substituting the equations for Ψ and s above should provide $C_m \sim \text{const}(d_{31}^2/s_{11}^E)$.

The plot shown in Figure 32 is generated from measured data taken from the regular model and the *xs*-model RXMR devices. In this case, the mass is constant with changes made to either the geometry or the material. The difference in the mechanical damping term R_m is seen to vary with changes in film thickness as well as film length. Film length (L_o) in the regular model is ~22 mm and the *xs*-model has a film length of ~46 mm. While some of the data (119 μm regular) appear to be linear, other data appear more clustered about a region. However a general trend seems to present itself, damping is increased by both material thickness and geometry.

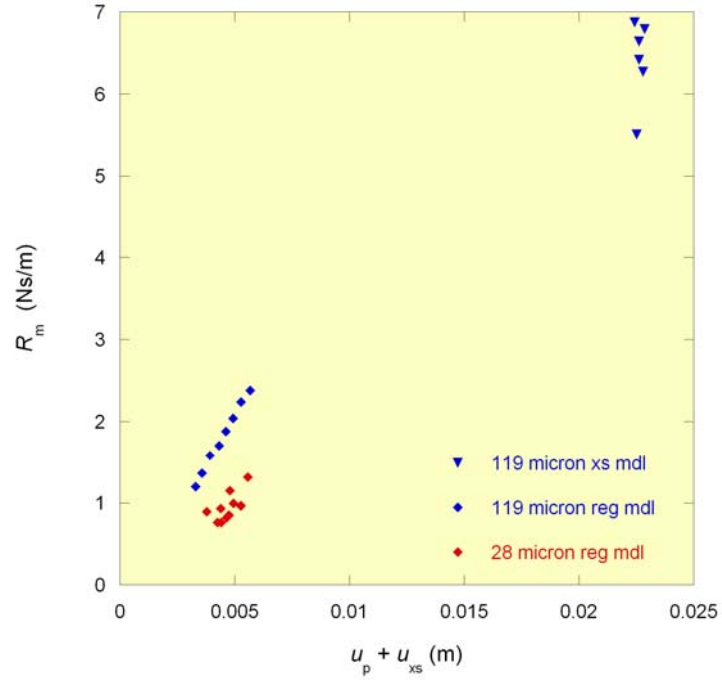


Figure 32 Mechanical damping R_m vs. $u_p + u_{xs}$ generated from data sets. Blue data are from 119 μm films, red data are from 28 μm films, diamonds are from a regular model device, triangles are from an xs-model device.

CHAPTER THREE

3 XMR BASICS

This chapter is principally a reproduction of a paper published in *Smart Materials and Structures* (Morris, D.J., Youngsman, J.M., Anderson, M.J., and Bahr, D.F., *A resonant-frequency tunable, extensional mode piezoelectric vibration harvesting mechanism*. *Smart Materials and Structures*, 2008. **17**). Sections written by co-authors have been paraphrased but the structure and derivations are mostly duplicated. The content has been expanded to address the additional figures that relate this work to prior literature.

3.1 Introduction

The three principal methods of electromechanical energy conversion in vibration harvesting devices are electrostatic, electromagnetic and piezoelectric. A number of reviews have been compiled recently that present the theory and performance of these methods [8, 29, 49]. Electrostatic harvesters have been demonstrated in different configurations [6]. Electromagnetic devices have been successfully demonstrated for a variety of structures and designs [1, 3, 50]. Piezoelectric configurations, principally fabricated as cantilevers of ceramic lead – zirconate – titanate (PZT), are demonstrated in several publications; e.g. [6, 16, 51], and Kim *et al* present a unique compression method with a piezoceramic structure [52].

Regardless of the particular electromechanical energy conversion technique, the entire vibration harvesting device may be viewed as a simple oscillator (mass and spring), excited externally by a vibration source, with mechanical and electrical dissipative paths. Electrical dissipation in this sense is good; this is the power delivered to an electrical load or stored for use later. The mechanical dissipation is the losses in the conversion due to friction, bending, or damping. It is generally recognized that the most electrical power may be extracted when the mechanical device is at, or near,

resonance. Even good electromechanical converters convert a small fraction of the strain (piezoelectric converters) or kinetic (electromagnetic or electrostatic converters) energy at each pass. Therefore, high mechanical gain increases the effective transduction efficiency of input mechanical power to output electrical power.

An array of simple cantilevers may have a difficult job harvesting power from what might be viewed as a typical structural installation where a variety of frequencies are present. Even if each cantilever was constructed for a particular frequency [49], such that it was harvesting at resonance, there would be many devices operating at much less than optimal conditions. If a volume or weight constraint is enforced, this configuration becomes even less appealing. It is possible to increase the harvesting bandwidth of an individual cantilever such that a single or smaller array would capture more vibration energy by introducing additional damping, but this also reduces the electrical output of the device as the energy would be dissipated through the mechanical rather than the electrical path.

The issue of matching devices to environments leads to the interest in tunability. If a technique were available to adjust a harvester to match the environment into which it is placed, power production would occur at the efficient resonant frequency. This would allow less rigorous manufacturing tolerances and the ability for a single device to be used in a variety of installations. It is a straightforward extension to envision “smart” devices that could track the frequencies available in the installation and adjust themselves to maximize power output.

The literature shows a few implementations of frequency tuning in resonant devices for vibration harvesting. In general, the stiffness of the device is controlled as this is easier to implement than a dynamic change in the effective mass. These methods fall into two main categories:

1. Control of the stiffness of a piezoelectric beam by adaptive capacitive loading or other electrical control schemes; for example, as in [6, 16, 17];
2. Bias loading of a piezoelectric beam, which can decrease the stiffness by application of a compressive end load [19] or, application of magnetic forces to increase or decrease the beam stiffness [20].

Another class of wide band vibration harvesting mechanisms decouples the vibration frequency from the resonant frequency of the piezoelectric element by pulse-excitation of a high-natural-frequency generator by a low-frequency resonator [21, 23].

In this chapter a new mechanism that is capable of resonant frequency tuning will be detailed. The device can utilize any piezoelectric material or structure capable of supporting a tensile load. For simplicity the initial device designs utilize polyvinylidene fluoride (PVDF) films of varying thicknesses, but the theory outlined is applicable to other families of materials, for example, piezoceramics on metal foils. The device couples two nonlinear spring elements into a configuration that becomes an oscillator with wider ranges of linear motion. The spring elements, in this case PVDF films, are affixed on one end to a central mass and on the other end, to an adjustable frame element. By changing the length of the frame element, the effective stiffness of the spring element is changed which alters the resonant frequency of the system. Electrical power is observed to scale with acceleration as expected, however it is relatively insensitive to changes in the natural frequency.

3.2 The Extensional Mode Resonator

In this chapter the device described utilizes stretching rather than bending of the piezoelectric element. The device is constructed of films or membranes which by definition cannot support bending or compressive loads. Consider a film element of width, w , length $2l$, and thickness h , firmly anchored to a frame. The force, F , required to deflect the center of the single film element a distance, u , shown in Figure 33(a) can be described by the following equation for small excursions where $u/l \ll 1$

$$F = \frac{Ewh}{l^3} u^3. \quad (3.1)$$

This exhibits a cubic relationship between force and displacement.

Now if two identical films are attached with a rigid link of length $2u_p = u_1 + u_2$ as shown in Figure 33(b) the films act as spring elements and the structure will be in a state of static equilibrium. A force balance equation can be written as

$$F_{\text{TOT}} = \frac{Ewh}{l^3}u_1^3 + \frac{Ewh}{l^3}u_2^3 = 0, \quad (3.2)$$

and recognizing in the presented configuration u_1 is opposite in sign to u_2 and consequently equal to u_p . Finally introduce an arbitrary excursion Δu to the structure. This results in a force balance equation written as

$$F_{\text{TOT}} = \frac{Ewh}{l^3}(u_p + \Delta u)^3 + \frac{Ewh}{l^3}(-u_p + \Delta u)^3, \quad (3.3)$$

which simplifies to

$$F_{\text{TOT}} = \frac{Ewh}{l^3}(6u_p^2\Delta u + 2\Delta u^3). \quad (3.4)$$

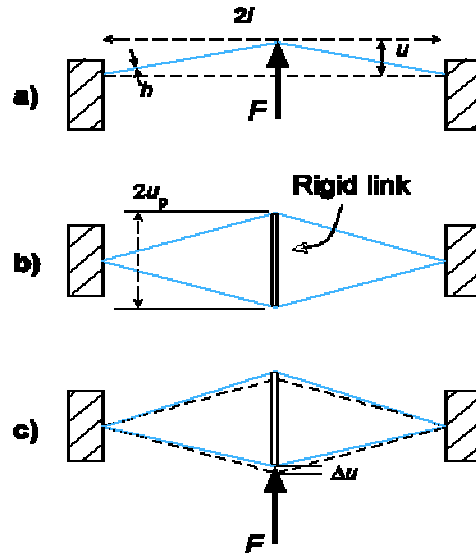


Figure 33 (a) Schematic of the displacement u of a rectangular string of non-deformed length $2l$, thickness h and width w (out of the plane of the figure) at the center by a force F . (b) Pre-tensioning two extensional elements by a rigid link of length $2u_p$. (c) Displacement of the link by an external force F by an amount Δu .

This demonstrates a force-deflection relationship of the structure with both linear and cubic terms in Δu . For sufficiently small displacements of Δu , the cubic portion contributes very little to the total force, F_{TOT} , and can be neglected. The effective stiffness of the structure can be found through the following equation

$$k = \frac{dF_{\text{TOT}}}{d(\Delta u)} \approx 6 \frac{Ewh}{l^3} u_p^2. \quad (3.5)$$

This demonstrates that a geometric change to the structure should allow an increase or decrease in the force required to displace the link. Substitution of Equation (3.5) into Equation (1.1) allows the derivation of an equation that demonstrates a linear relationship of frequency to the geometric change of the spring elements.

$$f_N = u_p \frac{1}{2\pi} \sqrt{6 \frac{Ewh}{ml^3}} \quad (3.6)$$

The next section describes the construction and testing of a device to validate the equations presented to this point.

3.3 Prototype Device Fabrication and Experimental Measures

For proof-of-concept testing the first prototype of the XMR used a full circular diaphragm geometry made from metalized 28 μm -thick piezoelectric polyvinylidene fluoride (PVDF) (Measurement Specialties, Inc), and a seismic mass largely constructed from an alloy of 90 % tungsten, 6 % copper, and 4 % nickel (Marketch International). The tungsten alloy has a density of 17,000 kg m^{-3} , which is close to the density of pure tungsten (19,300 kg m^{-3}) but is easy to machine with conventional tooling. The total live mass was 26.4 g. Other rigid parts of the XMR were constructed of brass. The PVDF was glued to the clamping rings and attached to both sides of the seismic mass with nylon screws. The W-alloy and brass components were electrically isolated from the metalized PVDF film by applying a lacquer coating where they might contact the PVDF, and etching the electrodes from the PVDF using a peroxy-sulfuric acid solution. The electrodes may also be etched using a ferric chloride solution. The electromechanical properties of the PVDF, as reported by the manufacturer, are $d_{31} = 23 \text{ pC N}^{-1}$, $\varepsilon = 106\text{-}113 \text{ pF m}^{-1}$, and $E = 2\text{-}4 \text{ GPa}$; the films were chosen for ease of use in verification of the model and initial device construction, and should not be considered as either upper or lower bounds on the range of materials that could be used in this device.

The PVDF elements were suspended at the center with flanged brass spools. The rigid link between the spools is an 8-32 screw, the effective length of which may be changed by turning the screw relative to the spools. This is the mechanism by which u_p , and therefore the resonant frequency, is controlled. Figure 34(a) is a cross section view of the XMR detailing the relationship between the components. Figure 34(b) a photograph of the assembled XMR in preparation for testing. The volume of the XMR (excluding testing fixtures) is about 10 cm^3 (0.6 in^3).

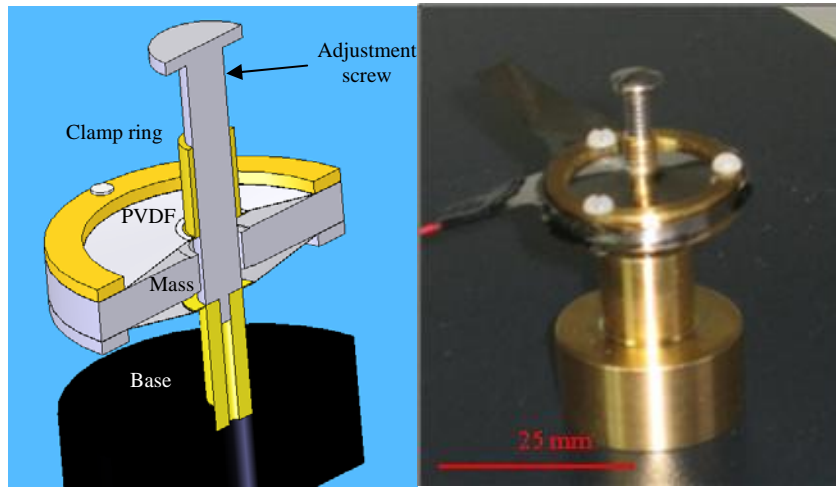


Figure 34 (a) Section view of the XMR (b) Photograph of an assembled XMR device

Figure 35 is a cross-sectional schematic that demonstrates the operation of the XMR. In this figure, the base to which the device is attached is considered the reference frame and is rigidly attached to the page. The membrane suspension spools are also rigidly attached to the base. Vibration excitation of the base induces motion of the seismic mass relative to the base. This in turn causes each piezoelectric membrane to alternately lengthen and shorten. Electrodes on both sides of the piezoelectric material collect charge developed through the direct piezoelectric effect.

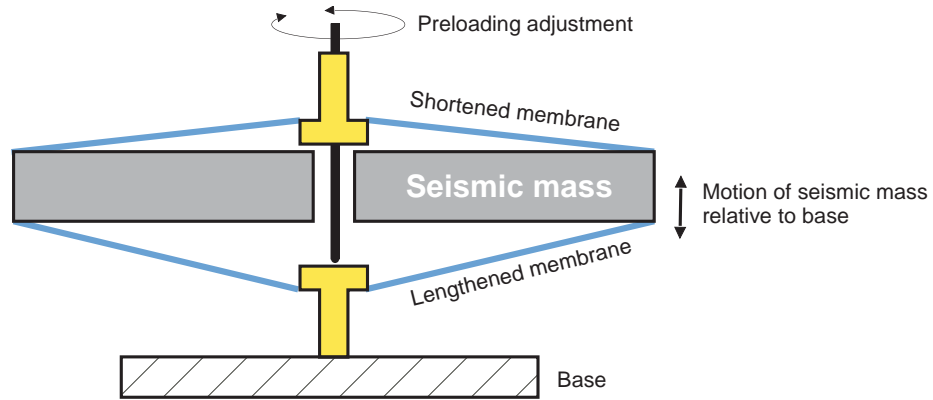


Figure 35 Cross-sectional schematic of the XMR device driven by base excitation. In this schematic, the seismic mass has moved upwards relative to the base, causing the top piezoelectric membrane to shorten and the bottom membrane to lengthen. Continued vibratory motion causes the membranes to alternately lengthen and shorten [24].

The XMR was mounted to a vibration table (Brüel and Kjaer 4801) for testing. The driving signal was typically white noise (to observe a frequency spectrum) or a sine wave from the signal source on a dynamic signal analyzer (DSA) (Agilent 35670A). The open-circuit voltage from the XMR, and an accelerometer that was mounted to the vibration table, were input to the DSA. The data were collected using either an oscilloscope (Tektronix TDS 2002) or the DSA. A convenient method of characterizing the spectrum of dynamic behavior is the frequency response function (FRF), defined here as the open circuit voltage across one or both of the piezoelectric membranes divided by the acceleration measured from the vibration table.

3.4 Frequency Tunability

Figure 36 is a plot of several FRFs acquired from the XMR in open-circuit conditions after changing the pretension displacement between three tuning screw positions in random order. Position 2 was the initial point. Position 1 had an u_p of 0.1 mm less than Position 2 and Position 3 had an u_p of 0.2 mm greater than Position 2. In general the resonant frequency was repeatable within the ability to reposition the tuning screw to the same location. The ability to reproduce the specific frequency of interest was possible to within 1% of the frequency; this is limited by the sensitivity of the adjustment screw used in the current study and not a fundamental limit on the device. Long term static loads with

this level of pre-tension did not cause the device resonant frequency to drift. In a complementary experiment, an XMR was tuned to a resonant frequency that was measured to be 81.5 Hz. The XMR was then driven at this frequency for four hours with a 9 m/s^2 acceleration amplitude. Every hour the resonant frequency of the XMR was measured using an impedance sweep technique [53], and found to be within the experimental uncertainty of the measurement (0.3 Hz). The prototype system demonstrated the ability to adjust to and maintain a specific resonant frequency. Furthermore, the voltage to acceleration ratio at resonance is effectively constant, even when doubled in frequency.

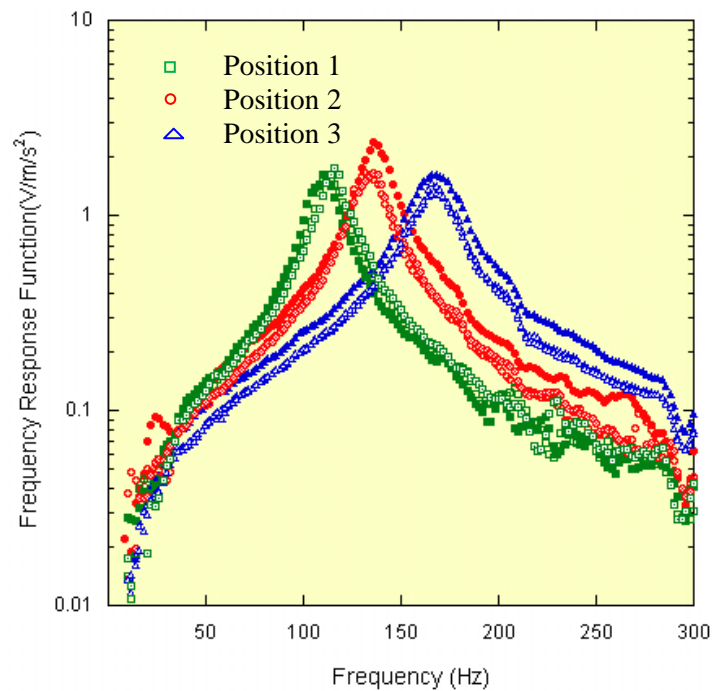


Figure 36 Frequency response functions from a frequency-tuning experiment in which each symbol indicates the same adjustment position. Different experiments at each adjustment position have different shading. The adjustment was varied between the three positions in a random sequence. This demonstrates the reproducibility of the frequency tuning mechanism.

A second resonant frequency tuning experiment was undertaken to examine the prediction of linearity of frequency to geometric changes to the device. The results in Figure 37 provide support for the assumption presented in Equation (3.6). The XMR was adjusted through a range of preloads which varied the dimension u_p by approximately 1.25 mm which resulted in resonant frequencies that ranged from 80 Hz to 235 Hz. The red line represents a least squares linear fit of the data that lies within a

95% confidence interval. This broad range of frequencies encompasses almost the entire spectrum of low level vibration sources suitable for energy harvesting as reported by Roundy [29]. By comparison this range of tuning, on the order of 66% calculated as $(f_{\max} - f_{\min}) / f_{\max}$, is far greater than others reported in the literature.

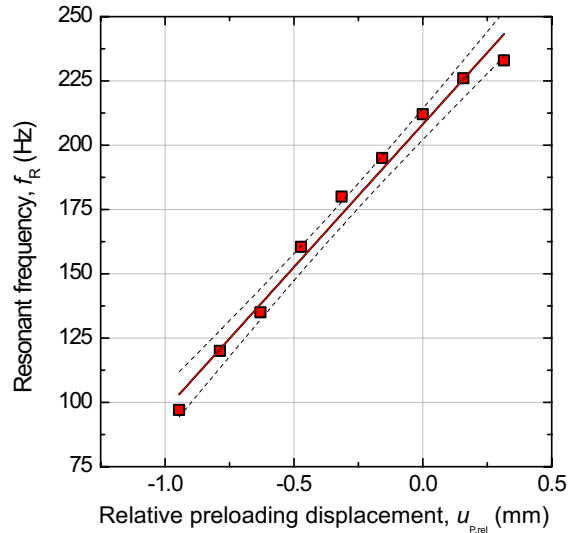


Figure 37 Resonant frequency, determined by the frequency response function, as a function of relative preloading displacement. The placement of the preloading screw at 212 Hz is an arbitrary datum. The solid line is a least-squares linear fit, and the dashed lines indicate a 95 % confidence interval [24].

Leland and Wright achieved a reduction in resonant frequency from 250 Hz to 200 Hz and from 190 Hz to 160 Hz (two different seismic masses) by applying a compressive axial load to a beam that supported a seismic mass midspan as shown in Figure 38 [19]. The lower limit occurred at the buckling point of the column due to the large loads required, up to 65 N. They report a tuning range of 20% for a 7.1 g mass and 16% for a 12.2 g mass.

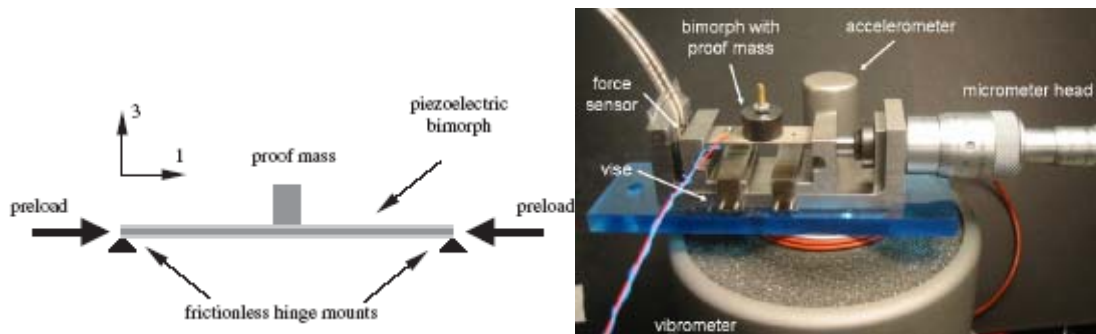


Figure 38 Compressive beam technique (a) schematic of technique (b) device under test [19].

Challa *et al* [20] has shown a technique using permanent magnets attached to a cantilever harvester and the frame to either increase or decrease the resonant frequency. The adjustment depends on the orientation of the poles of the magnets. Like poles cause a relative increase of the beam stiffness and consequently an increase in the resonant frequency while opposing poles reduce the stiffness but also present a problem of attachment in the event of over-travel by the beam. The cantilever/mass assembly has a natural frequency of 26.2 Hz. Through application of the magnets and adjustment of the separation distance d_x of the magnets, they were able to tune the frequency between 22 Hz and 32 Hz. Using the same calculation above, this results in a reduction of 31%.

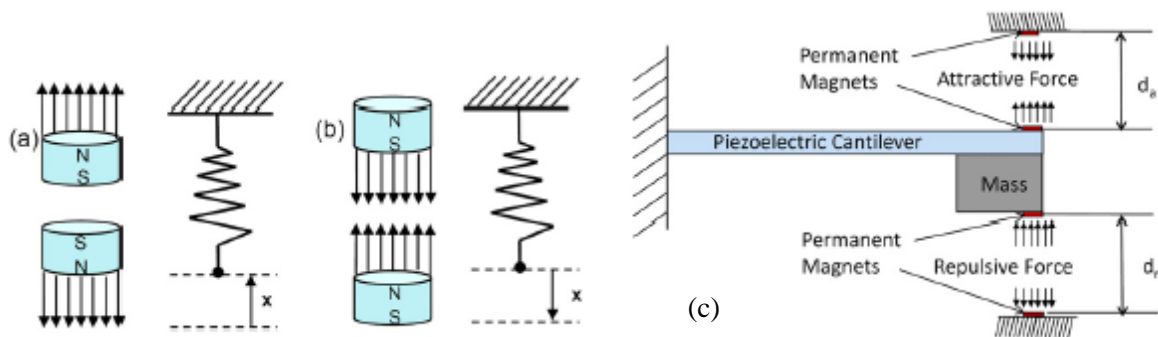


Figure 39 Magnetic assist by Challa *et al* (a) magnet configuration that increases the effective stiffness of the beam (b) magnet configuration that decreases the effective stiffness of the beam. (c) Device schematic showing positions of components [20].

Hu *et al* [54] describes a model for a piezoelectric cantilever capable of applying a tensile or compressive loads to the end much like the device demonstrated by Leland and Wright. The model

demonstrates that if such a device were constructed it would have a very broad tuning range, 60 Hz to 170 Hz, with power densities on the order of $40 \mu\text{W}/\text{cm}^3$. Frequency tuning is accomplished by adjusting a screw that is integrated or coaxial with the support layer in a bimorph piezoelectric cantilever. Figure 40 shows the authors suggested design.

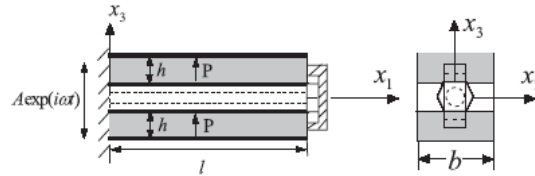


Figure 40 Schematic of Hu *et al* method to load a bimorph cantilever [54].

3.5 Power Results of the XMR

Figure 41 shows the power output of the original prototype device at several frequencies and accelerations. The power is calculated as $P = V_{rms}^2 / R_L$ where R_L is a fixed load resistance of 490 k Ω . It should be noted that the load was not impedance matched and only a single film was producing power. With both films operating, the power doubles. Impedance matching, where the load resistance is equal to the internal resistance of the piezoelectric device will allow the device to produce its maximum power.

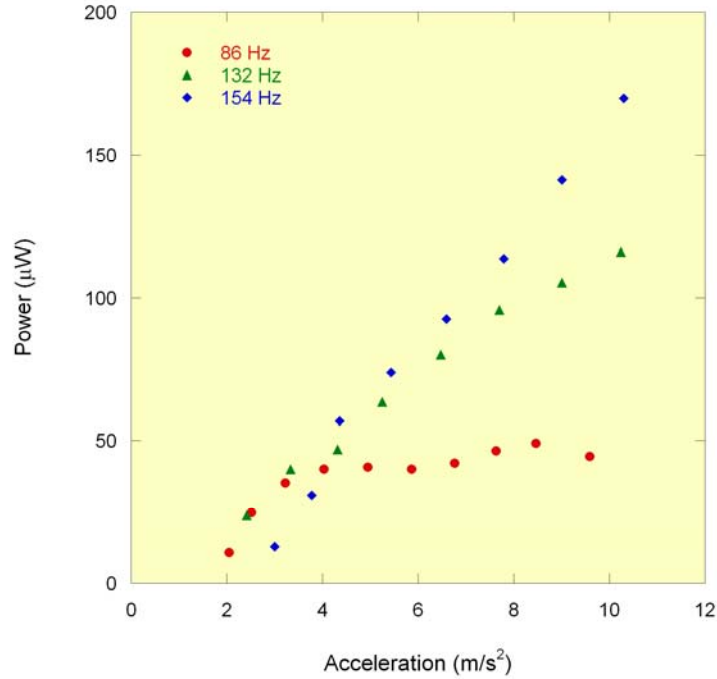


Figure 41 Power vs. acceleration for the prototype XMR.

Initial results at the lower acceleration amplitudes indicate a lesser dependence on frequency. The results in Figure 42 show the data from the linear region of the power-acceleration relationship. A statistical regression was performed on the data in this plot using *Minitab* software (State College, Pa.) to determine the primary influence on power production. The two inputs evaluated are acceleration amplitude and resonant frequency. The results report a *p*-value which is a measure of probability that a hypothesis of a particular regression coefficient should be rejected. Typically, *p*=0.05 is taken as the boundary between large and small. Regression of the data in Figure 42 to a model

$$\log P = \log(K) + \beta \log(A^2) \quad (3.7)$$

where $\log(K)$ and β are arbitrary constants returns $\log(K)=0.627$ and $\beta=0.818$ with $p=0.000$ for both terms. This implies that the terms are likely significant. Now if the data are regressed to

$$\log P = \log(K) + \alpha \log(f_N) + \beta \log(A^2) \quad (3.8)$$

where α is a constant for the $\log(f_N)$ regression term relating to resonant frequency, the results are *p*-values of $p=0.000$ for β , and $p=0.427$ for α . This means that the power output term may be

significantly related to the acceleration amplitude but not significantly related to the resonant frequency [24].

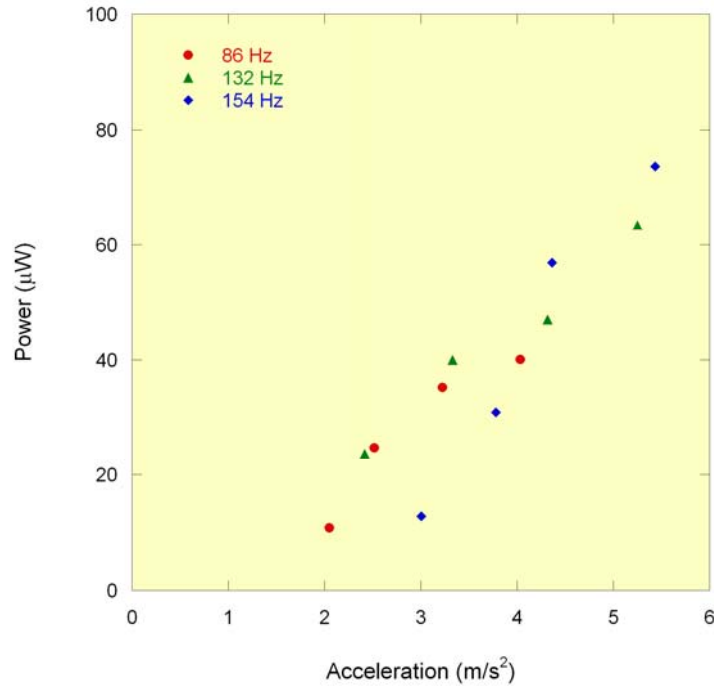


Figure 42 Power vs. acceleration of the prototype XMR at low acceleration amplitudes.

3.6 Conclusions

The extensional mode resonator (XMR) described in this chapter exploits the nonlinear force-deflection characteristics of a membrane to create a highly tunable piezoelectric vibration harvesting device. By rigidly coupling two piezoelectric membranes in the manner described, the nonlinearities cancel to create a linear spring with a highly variable spring constant. A piezoelectric vibration harvesting device with a repeatable frequency adjustment range greater than 150 Hz has been demonstrated. The large natural frequency adjustment range is beneficial in that a single vibration harvester model can generate substantial power in many different vibration environments. Analysis of power output demonstrates a strong dependence on acceleration amplitude with less dependence upon resonant frequency.

CHAPTER FOUR

4 MODEL DEVELOPMENT OF THE RXMR

This chapter is principally a reproduction of a paper submitted for publication in Journal of Sound and Vibration in 2009. Sections written by co-authors T. Luedeman, D. Morris, M. Anderson, and D. Bahr, have been paraphrased where possible but the structure and derivations are mostly duplicated.

4.1 Introduction

Improvements in wireless communication and sensing techniques, along with the reduction of power consumption in current microelectronics are driving demand for structural health monitoring systems. Although power consumption is low, battery life remains a critical factor in installation of distributed sensor networks. Because battery exchange requires considerable manpower, techniques are under investigation that can charge batteries or alternatively super capacitors as a means to extend the service life of installed networks. A larger concern is the installation that is either dangerous or no longer accessible for battery exchange. Solar generated power is ubiquitous, but is not a universal solution. A solution is required for installations that may not have or may not want solar exposure. Vibrations are available in many instances and can provide the critical energy input for the piezoelectric class of materials. Researchers are investigating vibration harvesting utilizing various self energizing techniques including electromagnetic in both a cantilever configuration [1-3] and single membrane form [4, 5], and piezoelectric, principally as cantilevers [6, 7]. A number of recent reviews discuss harvesting theory, techniques, and performance [8-11, 55].

A critical issue with most resonating harvesters is their best performance occurs at a single or very narrow frequency range. Therefore, many devices must be designed for and limited to a known environment. Adjustable resonant tuning provides flexibility in a device and the opportunity to

maximize power generation. Literature shows limited cases of resonant tuning and can be described as external electrical control [16, 17], beam compression techniques [18, 19, 54], beam stiffness change through piezoelectric effect [18], beam stiffness change through magnetic field application [20], decoupling [21], cantilever arrays [22], or frequency rectification [23].

An issue with the cantilever design is the reduction in power output as the driving frequency increases. An accepted model predicting the maximum power of a cantilever harvester as postulated by a number of researchers [1, 8, 11, 29, 42] is shown in Eq. (4.1) and a conditional form, as suggested by Morris *et al.* [24] is written as Eq. (4.2)

$$|\Pi| = \frac{m\zeta_E A^2}{4\omega\zeta_T^2} = \frac{b_E m^2 A^2}{2(b_E^2 + 2b_E b_M + b_M^2)}, \quad (4.1)(4.2)$$

where A is the acceleration amplitude, ζ_E and ζ_T are the electrical and total dimensionless damping coefficients, and b_E and b_M are the electrical and mechanical damping coefficients. The equation assumes that the natural frequency, ω_n , equals the driving frequency, ω . From Eq. (4.1) it is apparent that as the driving frequency increases, the power generated is reduced if the damping coefficients remain constant with frequency. The conditions of Eq. (4.2) assume the damping terms b_E and b_M remain constant with changes in device stiffness. This removes the dependence on frequency for electrical power generation.

The extensional mode resonator (XMR) [24] is constructed of piezoelectric films, in this case polyvinylidene fluoride (PVDF), that suspend a mass to a rigid frame. As the frame vibrates, the compliance of the films permits the mass to oscillate about a neutral axis which alternately stretches the films. The alternating strain cycle applied to the films generates electricity through the direct piezoelectric effect. The unique geometry of the XMR permits simple adjustability of the resonant frequency through a change in stiffness rather than a change in mass. Initial experiments with the XMR device appear weakly dependant upon resonant frequency and more strongly affected by mechanical damping (b_M in Eq. (4.2)).

An advantage of the XMR design (Figure 43) is the ability to utilize stretching rather than bending mode for generating the piezoelectric effect. The initial prototype device presented in the previous chapter utilized circular membranes. During the development of the following model it was determined that although the circular XMR model is more structurally stable, it had lower power output due to a strain gradient as a result of its circular design. In the case of the rectangular version, all strains are uniaxial and uniform. Because there is no strain gradient as in the circular XMR or a cantilever [6], the entire active area of the films produce power effectively. The implications of geometry changes to the device stiffness and frequency are shown in the following model section followed by verification of the model with an experimental prototype device.

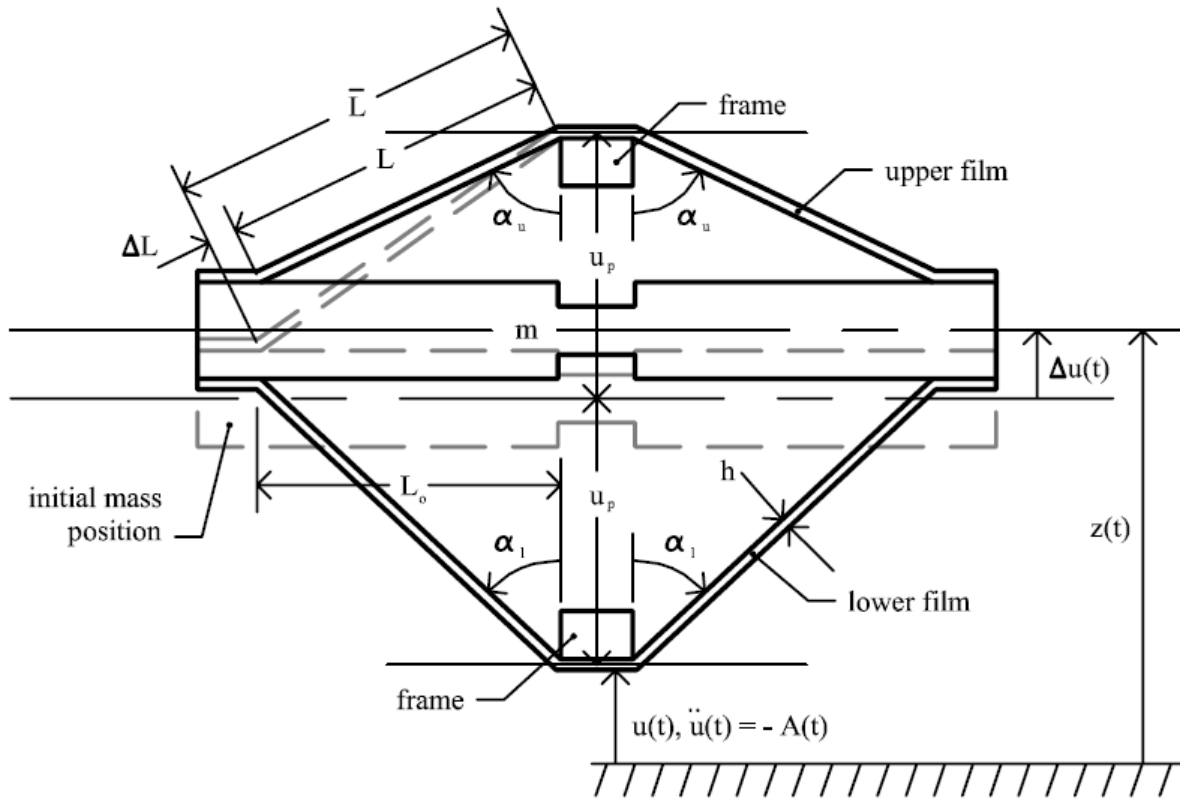


Figure 43 Schematic for mechanical function of the XMR device.

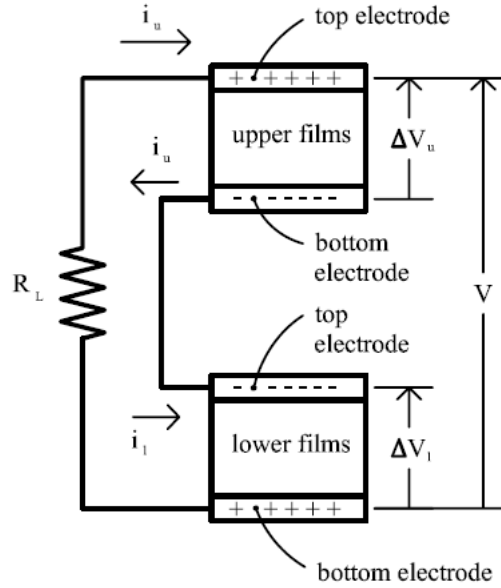


Figure 44 Schematic for electrical function of the device.

4.2 Dynamic Model

Consider the schematic diagrams of the eXtentional Mode Resonator shown in Figure 43 and Figure 44. They illustrate the mechanical and electrical function of the device. As shown in Figure 43, the device consists of a moving mass m and adjustable frame. Four PVDF films, of unstretched length L_0 , width w (into the plane of the figure), and thickness h are fixed to the moving mass and the central hub of the frame. The central hubs are moved vertically a distance u_p from the moving mass to preload the films and deform them to the dimension \bar{L} . The frame is moved at a specified inertial acceleration \ddot{u} , while the inertial displacement of the mass is z , and the displacement of the mass relative to the moving frame is Δu . While m executes relative movements Δu , the instantaneous length L of each film is $L = \bar{L} + \Delta L$, where ΔL is the stretch of each film caused by the movements Δu . In Figure 44 the electrical function of the upper and lower films are shown symbolically. The top and bottom electrodes on the upper and lower sections are connected, so as to form the potentials ΔV_u and ΔV_l respectively. The polarity of the upper and lower films are indicated by “+” and “-”, where the polarity is referenced to the free charge attracted to the electrode. The currents i_u and i_l flow into the top

electrodes of the upper and lower films. A load resistor R_L is placed as shown to model harvesting of electrical energy, and the remaining electrodes will be connected such that $i_u=i_l$.

The objective is to develop a model that will predict the time-averaged power Π dissipated in a resistor placed across the electrodes of the XMR given a specified acceleration \ddot{u} . In what follows, Newton's second law will be derived for the vertical motion of m , and the electromechanical coupling of the PVDF film to a load resistor placed across the electrodes will be determined.

To derive the mechanical response of the device, consider the free-body diagram of the mass in the deflected condition shown in Figure 45. Neglecting gravity, the only forces on the mass originate from the stretching of each PVDF film. Denote N as the axial force of a PVDF film on m , and F_v as the vertical component of the axial force N .

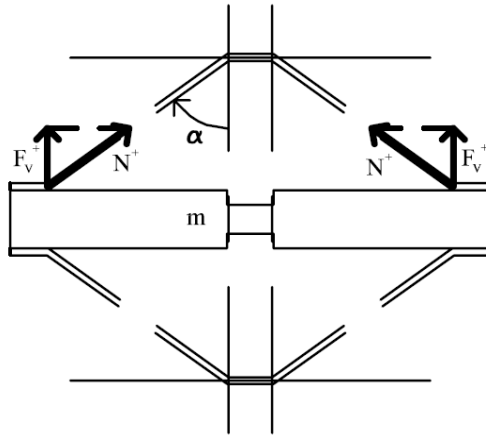


Figure 45 A free-body diagram for the mass m .

Furthermore, the vertical reactions are subdivided in F_v^+ and F_v^- depending upon whether they originate from the upper or lower films respectively. The force F_v can be computed from $F_v=N\cos\alpha$, where the angle α is subscripted as α_u and α_l for the upper and lower films shown in Figure 43 and Figure 45. The axial force N can be computed from the constitutive equations for the film [56]

$$S_1 = -d_{31}E_3 + s_{11}^E T_1, \quad (4.3)$$

$$D_3 = \varepsilon_{33}^T E_3 - d_{31} T_1, \quad (4.4)$$

where S , T , E , and D are strain, stress, electric field and electric displacement; d_{31} , s_{11}^E , and ε_{33}^T are the piezoelectric coefficient, mechanical compliance and electric permittivity; the 1-direction is along the film axis and the 3-direction is in the film thickness direction. In Equations (4.3) and (4.4), the upper films are assumed to be oriented such that a release in tension associated with positive movements Δu of m cause a positive voltage at the top electrode, consistent with Figure 44. Consequently, the piezoelectric coefficient d_{31} is taken to be negative. The constitutive model, Equations (4.3) and (4.4), assumes that the stress in the 2-direction is zero ($T_2=0$), and that the films are free to contract in the 2-direction. This is a simplifying assumption in the model, and its quantitative effect will be neglected at this point in time. Given that $T_1=N/wh$ because a tension on an upper film is a force F_v in the opposite direction on m , $F_v=N\cos\alpha$, $S_1=\Delta L/L_o$, and $\Delta V = -\int_0^h E_3 dz$, Equation (4.3) can be rewritten for the upper and lower films as

$$F_v^+ = \frac{wh \Delta L}{s_{11}^E L_o} \cos \alpha_u + \frac{d_{31} w}{s_{11}^E} \cos \alpha_u \Delta V_u \quad (4.5)$$

$$F_v^- = \frac{wh \Delta L}{s_{11}^E L_o} \cos \alpha_1 - \frac{d_{31} w}{s_{11}^E} \cos \alpha_1 \Delta V_1 \quad (4.6)$$

The component of the force F_v^- induced by the voltage ΔV_1 on m from the lower film is negative because the polarity of the lower films are opposite that of the upper films. To obtain a linear model, it is assumed that Δu of m is small, and linearization of Equations (4.5) and (4.6) results in

$$F_v^+ = \frac{wh u_p}{s_{11}^E L_o} \left\{ 1 - \frac{1}{\left[1 + \left(\frac{u_p}{L_o} \right)^2 \right]^{1/2}} \right\} - \frac{wh}{s_{11}^E L_o} \left\{ 1 - \frac{1}{\left[1 + \left(\frac{u_p}{L_o} \right)^2 \right]^{3/2}} \right\} \Delta u - \frac{d_{31} w u_p}{s_{11}^E L_o} \frac{1}{\left[1 + \left(\frac{u_p}{L_o} \right)^2 \right]^{1/2}} \Delta V_u, \quad (4.7)$$

$$F_v^- = -\frac{wh u_p}{s_{11}^E L_o} \left\{ 1 - \frac{1}{\left[1 + \left(\frac{u_p}{L_o} \right)^2 \right]^{1/2}} \right\} - \frac{wh}{s_{11}^E L_o} \left\{ 1 - \frac{1}{\left[1 + \left(\frac{u_p}{L_o} \right)^2 \right]^{3/2}} \right\} \Delta u - \frac{d_{31} w u_p}{s_{11}^E L_o} \frac{1}{\left[1 + \left(\frac{u_p}{L_o} \right)^2 \right]^{1/2}} \Delta V_1. \quad (4.8)$$

The terms in Equations (4.7) and (4.8) above are caused by static extension of the films, displacements Δu caused by movement of the mass, and the voltages ΔV_u and ΔV_1 induced across the electrodes of the upper and lower films. The total vertical force F on m from all four films then is

$$F = 2F_v^+ + 2F_v^- = -s\Delta u - \Psi\Delta V_u - \Psi\Delta V_1, \quad (4.9)$$

where

$$s = 4 \frac{wh}{s_{11}^E L_o} \left\{ 1 - \frac{1}{\left[1 + \left(\frac{u_p}{L_o} \right)^2 \right]^{3/2}} \right\} \quad (4.10)$$

$$\Psi = 2 \frac{d_{31} w u_p}{s_{11}^E L_o} \frac{1}{\left[1 + \left(\frac{u_p}{L_o} \right)^2 \right]^{1/2}}. \quad (4.11)$$

Physically, s is a mechanical stiffness, and Ψ is a coupling coefficient with units of N/V.

There are two components of s , one given by the extensional stiffness of the four films, and the other being a geometric dilution parameterized by the ratio u_p/L_o . Similarly, Ψ consists of a component that would be expected from extensional strains, and a geometric dilution. Newton's second law for the motion of the mass is

$$F - R_m(\dot{z} - \dot{u}) = m\ddot{z}, \quad (4.12)$$

where R_m is a coefficient of mechanical damping. Using the fact that $z=u+\Delta u$, letting $\ddot{u}=-A(t)$, and using Equation (4.9) for F , Newton's law, Equation (4.12), for m becomes

$$m\Delta\ddot{u} + R_m\Delta\dot{u} + s\Delta u + \Psi\Delta V_u + \Psi\Delta V_1 = mA(t). \quad (4.13)$$

To derive the electrical response of the device, voltage-current laws are derived for the upper and lower films shown in Figure 44. Starting with one of the upper films, elimination of the stress T_1 from Equations (4.3) and (4.4) gives

$$D_3 = \varepsilon_{33}^T \left(1 - \frac{d_{31}^2}{s_{11}^E \varepsilon_{33}^T} \right) E_3 - \frac{d_{31}}{s_{11}^E} S_1. \quad (4.14)$$

Upon integrating $\int_0^h () dz$, using the fact that $\Delta V_u = -\int_0^h E_3 dz$, $\partial D_3 / \partial z = 0$ within the piezoelectric material, and $S_1 = \Delta L / L_o$, Equation (4.14) becomes

$$hD_3 = -\varepsilon_{33}^T \left(1 - \frac{d_{31}^2}{s_{11}^E \varepsilon_{33}^T} \right) \Delta V_u - \frac{d_{31}}{s_{11}^E} h \frac{\Delta L}{L_o}. \quad (4.15)$$

Next, integrate over a volume of infinitesimal thickness enclosing the interface between the electrode and the piezoelectric film. This operation converts Equation (4.15) to

$$wL_o hD_3 = -\varepsilon_{33}^T \left(1 - \frac{d_{31}^2}{s_{11}^E \varepsilon_{33}^T} \right) wL_o \Delta V_u + \frac{d_{31}}{s_{11}^E} wL_o h \frac{\Delta L}{L_o}. \quad (4.16)$$

To obtain a linear model for the upper films, $\Delta L / L_o$ is approximated for small motions Δu , the quantity $wL_o D_3$ is equated to the total free charge Q attracted to the electrode, and Equation (4.16) is multiplied by two to reflect the fact that the two top and bottom electrodes are common. Additionally, it is assumed that charge caused by static deformation has been dissipated. One then obtains

$$-Q_u = -\bar{C} \Delta V_u + \Psi \Delta u, \quad (4.17)$$

where Q_u is the total free charge attracted to the top electrodes on the upper films and

$$\bar{C} = 2 \frac{\epsilon_{33}^T \left(1 - \frac{d_{31}^2}{s_{11}^E \epsilon_{33}^T} \right) w L_o}{h}. \quad (4.18)$$

The derivation for the lower films is similar, only that the polarity orientation of the film is reversed, and positive movements of the mass Δu lead to extensional strains. For the lower films, the voltage-current law then is

$$-Q_1 = -\bar{C} \Delta V_1 + \Psi \Delta u. \quad (4.19)$$

As a final step, the circuit is completed by connecting the bottom electrode on the upper films to the top electrodes of the lower films. Then, $i_u = i_l$ and $V = \Delta V_u + \Delta V_l = -i_u R_L$, and the time derivative of the circuit equations for the upper and lower films are summed to obtain

$$C_o \dot{V} = -\frac{V}{R_L} + \Psi \Delta \dot{u}, \quad (4.20)$$

where

$$C_o = \frac{\bar{C}}{2} = \frac{\epsilon_{33}^T \left(1 - \frac{d_{31}^2}{s_{11}^E \epsilon_{33}^T} \right) w L_o}{h}. \quad (4.21)$$

Equations (4.13) and (4.20) constitute a model for the device, where the acceleration of the frame $A(t)$ is the input, and there are two equations for the unknowns V and Δu .

4.3 Electric Circuit Analysis and Energy Harvesting Capability

The model for the XMR device has a circuit analogy that is useful for analysis of power harvesting capability. Consider the circuit diagram shown in Figure 46. With the definitions of voltage $mA(t)/\Psi$ and current $\Psi \Delta \dot{u}$, and the components $R = R_m/\Psi^2$, $L = m/\Psi^2$, and $C = \Psi^2/s$, the circuit shown in Figure 46 can be verified to have the same governing equations as Equations (4.13) and (4.20).

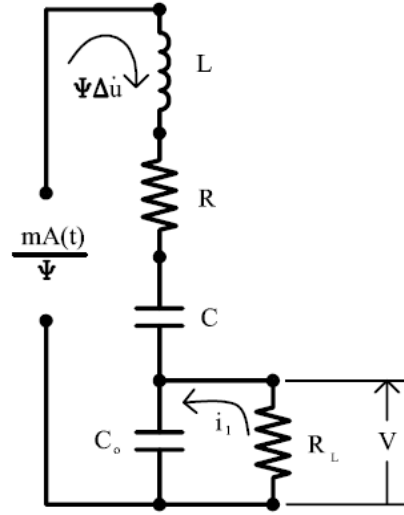


Figure 46 Equivalent circuit diagram for the device (Equations (4.13) and (4.20)).

Furthermore, the natural frequency of the RLC circuit is

$$\omega_n = \frac{1}{\sqrt{LC}} = \sqrt{\frac{s}{m}} = \sqrt{\frac{1}{m} 4 \frac{wh}{s_{11}^E L_o} \left\{ 1 - \frac{1}{\left[1 + \left(\frac{u_p}{L_o} \right)^2 \right]^{3/2}} \right\}}, \quad (4.22)$$

and the quality factor Q is

$$Q = \frac{\sqrt{ms}}{R_m} = \frac{1}{R_m} \sqrt{m 4 \frac{wh}{s_{11}^E L_o} \left\{ 1 - \frac{1}{\left[1 + \left(\frac{u_p}{L_o} \right)^2 \right]^{3/2}} \right\}}. \quad (4.23)$$

Given a harmonic frame acceleration of amplitude A , it is necessary to specify the optimal frequency of operation and load resistance R_L . It has been shown [57, 58] that in the limit of low damping, optimal power production is obtained at two frequencies, the resonance frequency ω_n given by Equation (4.22) and the anti-resonance frequency. When damping becomes larger and exceeds a particular limit, called the bifurcation damping ratio [58] there is a single frequency for optimal power

production. The value of the bifurcation damping ratio is determined by the effective electromechanical coupling factor of the device. The performance of the XMR is not analyzed at this level of detail, instead the scope is restricted to the case that the damping is low, and power production is computed at the natural frequency ω_n .

It is straightforward to compute power, Π_L , dissipated across the load resistor, R_L beginning with the fundamental definition of power written as

$$\Pi_L = \frac{1}{2} \text{Re} \left[\hat{V}_L \hat{I}^* \right] = \frac{1}{2} \text{Re} \left[\hat{V}_L \left(\frac{\hat{V}_L}{R_L} \right)^* \right] = \frac{|\hat{V}_L|^2}{2R_L}, \quad (4.24)$$

where \hat{V}_L and \hat{I} are the complex amplitudes of voltage and current, and * indicates the complex conjugate of the variable. From the equivalent circuit diagram and electromechanical model, the equation for the voltage across the load resistor can be determined as

$$\hat{V}_L = \frac{1}{R \left(\frac{1}{R_L} + j\omega_n C_o \right) + 1} \frac{mA}{\Psi}. \quad (4.25)$$

Performing the magnitude calculation using complex conjugates yields the following expression for the numerator in the power equation

$$|\hat{V}_L|^2 = \frac{1}{\left(\frac{R}{R_L} \right)^2 + 2 \left(\frac{R}{R_L} \right) + (\omega_n RC_o)^2 + 1} \frac{m^2 A^2}{\Psi^2}. \quad (4.26)$$

Finally, substitute Equation (4.26) into the Equation (4.24) to arrive at

$$\Pi = \frac{1}{2} \frac{1}{R_L} \frac{1}{\left(\frac{R}{R_L} \right)^2 + 2 \left(\frac{R}{R_L} \right) + (RC_o \omega_n)^2} \frac{m^2 A^2}{\Psi^2}. \quad (4.27)$$

The optimal load resistance $R_{L,o}$ is found by maximizing the time-average power Π . By differentiation of Π from Equation (4.27), the optimal load resistance $R_{L,o}$ is found to be

$$R_{L,o} = \frac{R}{\sqrt{1 + (RC_o\omega_n)^2}}. \quad (4.28)$$

Given an optimal load resistance $R_{L,o}$ specified by Equation (4.28), the corresponding optimal time-averaged power dissipation Π_o from Equation (4.27) will be

$$\Pi_o = \frac{1}{4R_m} \frac{1}{\sqrt{1 + (RC_o\omega_n)^2}} m^2 A^2. \quad (4.29)$$

4.4 Prototype Device

A prototype XMR was fabricated for experimental verification of the model. The active components of the device occupied a net volume of 21 cm³. The total live mass of the device was 82.3 g. Commercially available PVDF film (Measurement Specialties, Inc.) was used as the piezoelectric element. Properties of the film provided by the manufacturer and other device constants are contained in Table 3.

Table 3 Device geometry constants and PVDF film properties.

m [g]	82.3
L_o [mm]	22
w [mm]	23.95
h [μm]	119
s_{11}^E [m ² /N]	3.65E-10
d_{31} [C/N]	-2.30E-11
ϵ_{33}^T [C/V/m]	1.10E-10
k_{31} [%]	1.15E-01

4.5 Electrical Impedance

Electrical impedance experiments were conducted with an Agilent 4294A precision impedance analyzer to determine the circuit parameters C_o , R , L , C and k^2 . The electromechanical coupling coefficient k^2 is defined as the ratio of energy converted by the system divided by the energy input into the system. The impedance sweep data (Figure 47) was curve fit using a least squares fit in

which variables C_o , R , L , and C were allowed to change. The mechanical damping R_m was calculated using the measured R from the impedance sweep, Equation (4.11), and the relationship $R_m=R\Psi^2$. Results from the impedance sweep were also used to find the optimal load resistance $R_{L,o}$ in order to achieve a matched impedance power experiment. The films were connected in series so that measurements captured the values of the device rather than the individual film elements. An electrical impedance measurement was conducted at each tension screw setting u_p , as the circuit parameters depended upon the device geometry as discussed in Section 4.2 Dynamic Model.

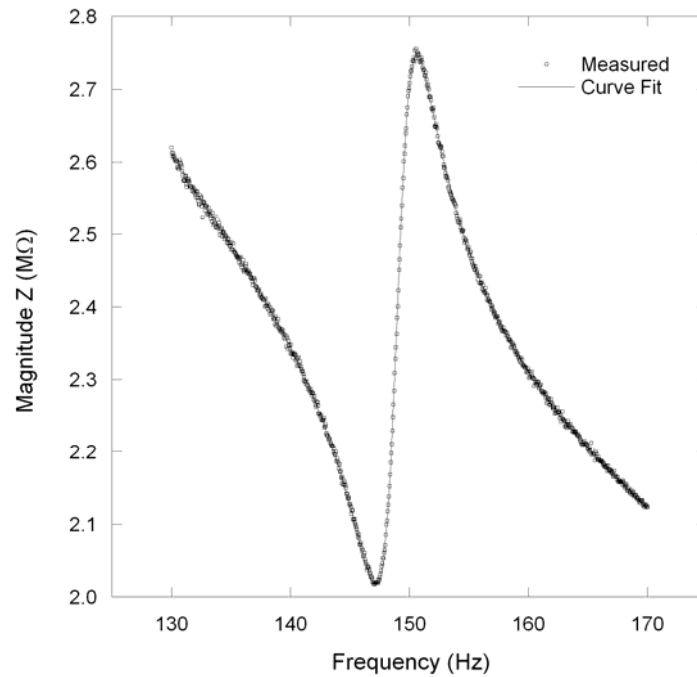


Figure 47 Measurement of electrical impedance and curve fit for circuit parameters R , L , C , C_o and k^2 .

4.6 Mechanical Vibration and Power Output

The schematic for the power measurement experiment is detailed in Figure 48. The XMR device was mounted to a MB Electronics EA1250 vibration head driven with a MB Electronics 2120 amplifier. The input signal to the amplifier (both white noise and fixed sine) was generated by an Agilent 35670A Dynamic Signal Analyzer (DSA). Accelerations were measured with a Bruel & Kjaer Type 4395 accelerometer mounted to the vibration head. The impedance matched resistive load was

provided by an AEMC BR07 decade resistance box. Measurements were conducted at room temperature. Temperature effects were observed during other extended run experiments and caused ~10% reduction in power when the room temperature increased by ~5°C but were not observed in the short time span of the present experiments.

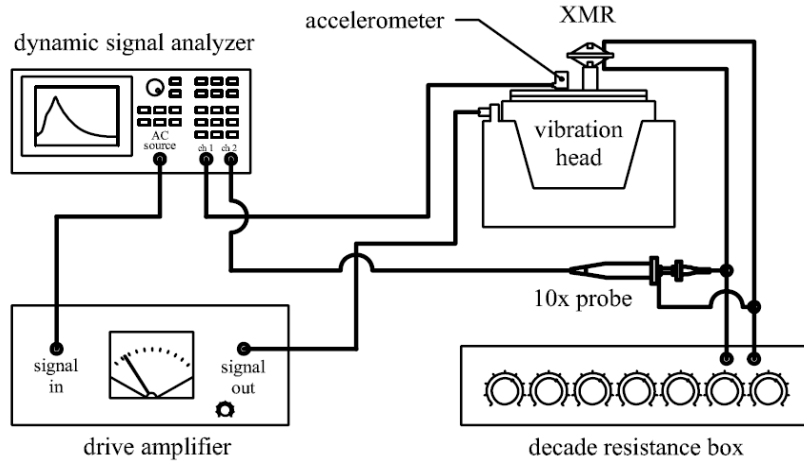


Figure 48 Apparatus used to perform power output experiment from a controlled vibration source.

The typical power measurement series was conducted by first exciting the XMR with white noise in order to determine the resonant frequency. In addition to providing the source signal, the DSA was used to capture the XMR and accelerometer output voltages and to plot the transfer function of mechanical excitation shown in Figure 49. In this experiment the transfer function was defined as the output RMS open circuit voltage of the XMR divided by the acceleration. Open circuit condition refers to the absence of an electrical load across the film elements. The resonant frequency was identified by the maximum in the transfer function. Once the resonant frequency was found, the XMR was excited with a fixed sine signal at that resonant frequency at multiple accelerations. A feature of the DSA enables the use of measurement averaging (in this case, 50 measurements) to improve the resolution in V_{RMS} for each acceleration setting. Power was calculated from $P = V_{RMS}^2 / R_L$ where R_L is the total load resistance of the system (load from the decade box parallel to load from the DSA). When all the desired measurements were collected, the XMR was tuned to a new resonant frequency by adjusting the tension screws. This step changed the u_p position and the initial tension in the films. For

each position u_p , a new impedance measurement was conducted. Once the impedance measure was made, the power experiment was repeated.

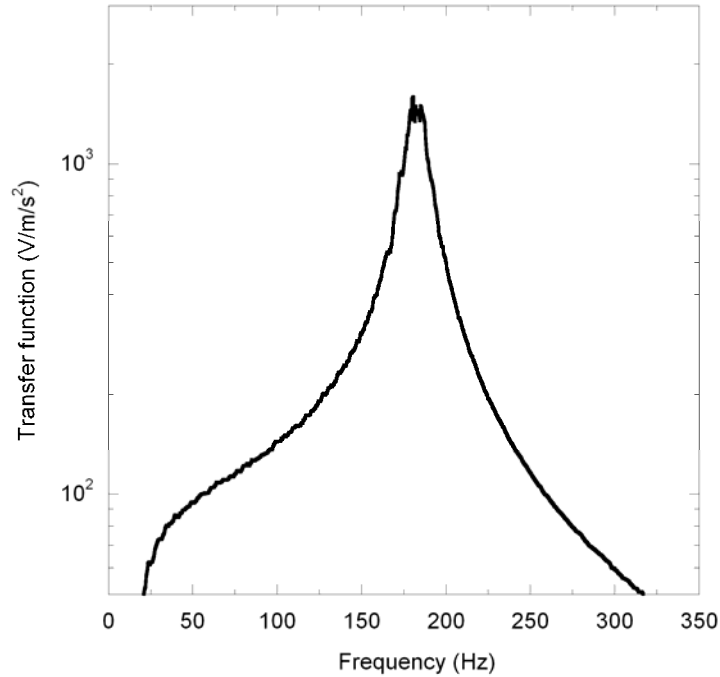


Figure 49 Transfer function vs. frequency of the XMR device. Peak indicates the resonant frequency of the oscillator.

4.7 Results

In this section, results of impedance and mechanical vibration measurements as described in Sections 4.5 and 4.6 are presented. These measurements allow comparison of measured and theoretically predicted device parameters and power output. A discussion of properties of the device as predicted by the theoretical model follows in Section 4.8.

4.7.1 Impedance Tests and Device Parameters

Table 4 provides a comparison of the XMR properties obtained in the impedance experiment with the values determined from the theoretical model. The model provides the fundamental values from geometry and materials properties to calculate the terms in Table 4 using the additional relationships $C=\Psi^2/s$, $L=\Psi^2/m$, $k^2=C/(C+C_o)$, and $f_n=\omega_n/2\pi$. The geometric term u_p was selected to obtain nominal natural frequencies of $f_n=120$ Hz, 150 Hz, and 180 Hz, shown in Table 4.

Table 4 Configuration, impedance measurements, and theoretical predictions for nominal natural frequency of $f_n=120$ Hz, 150 Hz, and 180 Hz. (119 μm film)

Parameter	120 Hz			150 Hz			180 Hz		
	Measured	Theoretical Prediction	% Diff	Measured	Theoretical Prediction	% Diff	Measured	Theoretical Prediction	% Diff
u_p [mm]	3.59			4.62			5.67		
ε_0 [%]	1.32			2.18			3.27		
C_o [pF]	461	479	-4	453	479	-5	458	479	-4
R [M Ω]	7.85			7.06			6.14		
L [kH]	473	349	36	308	214	44	212	145	46
C [pF]	3.81	4.29	-11	3.72	4.31	-14	3.76	4.33	-13
k^2 [%]	0.82	0.89	-8	0.81	0.89	-9	0.81	0.9	-10
f_n [Hz]	119	130	-8	149	166	-10	178	201	-11
R_m [Ns/m]	1.36			1.89			2.39		
Ψ [mN/V]	0.417	0.485	-14	0.517	0.62	-17	0.624	0.753	-17
s [kN/m]	45.7	54.9	-17	71.7	89.1	-20	103	131	-21
$R^*C_o^*\omega_h$	2.48			2.99			3.15		

Consider the measurements and predictions contained in Table 4 in which the XMR was configured to have a natural frequency of 120 Hz. Referring to the second column, a value of $u_p=3.59$ mm was selected. Because the value of L_o is known, and the assumption that the film elements are identical, it is straightforward to calculate a static strain of 1.32% in each film. Electrical impedance measurements gave the values shown in column two for C_o , R , L , C and k^2 . Derived further from the impedance measurements was $\Psi = \sqrt{mL}$, $f_n = 1/2\pi\sqrt{LC}$, and $s=\Psi^2/C$. Presently, the scope of the theoretical model does not include an *a priori* prediction of damping R_m . In the third column of Table 4 are theoretically predicted values of the device parameters using the expressions contained above and in Sections 4.2 and 4.3. The fourth column shows the difference between the measured value and theoretical prediction expressed in percent. Columns 5-7 and 8-11 in Table 4 follow the same format as columns 2-4.

The fundamental properties of the XMR device can be divided into two categories. The first category composed of s , Ψ , C_o , and R_m are fundamental properties of the device. The second category of device parameters are those derived from s , Ψ , C_o , and R_m . These include effective

electromechanical coupling factor k^2 , and the product $RC_o\omega_h$. The product $RC_o\omega_h$ is discussed in Section 4.8 regarding power generation.

Referring to Table 4, it can be seen that the difference between theoretically predicted and measured values for s , Ψ , and C_o ranged from 4-21%. The predicted coupling factor and stiffness consistently exceeded their measured values by approximately 15-20%. The model prediction of natural frequency was within ~10% of the measured value. For several reasons, the agreement was thought to be reasonable for a first order predictive model. PVDF properties, s_{11}^E , d_{31} , and h used in the model prediction were nominal values reported by the manufacturer (Measurement Specialties), and were not confirmed by independent measurement. It was unknown whether the manufacturer's specification for the permittivity is consistent with the tensor assumptions regarding ϵ_{33}^T in Equation (4.4). There was no attempt to compensate these properties for the relatively large amount of static strain encountered during operation. For a first approximation, the model seems to be valuable for predicting s , Ψ , and C_o based only upon material properties and device geometry.

From Table 4, it was observed that the predicted and measured effective mechanical coupling coefficient k^2 was slightly less than 1%. At most, the predicted and measured value of k^2 differed by 10%.

4.8 Mechanical Vibration and Power Output

A comparison of power output at the three nominal natural frequencies of 120 Hz, 150 Hz, and 180 Hz is shown in Figure 50 corresponding to the configurations described in Table 4. To compute a predicted power output using Equation (4.29) it was necessary to use a value for R_m obtained from impedance measurements of R , i.e., $R_m=R\Psi^2$. Multiple measurements of power were made for each device configuration to get an estimate of scatter. Maximum power outputs of 2.9 mW, 4 mW, and 4.4 mW were observed for acceleration amplitudes about ½ g and 9.4 mW and 9.5 mW at just under 1 g. The power output agreed very closely with theoretical predictions for small acceleration amplitudes, 1.3 m/s², 3 m/s², and 7 m/s², for nominal natural frequencies of $f_n=120$ Hz, 150 Hz, and

180 Hz respectively. At higher acceleration amplitudes, the predicted power output exceeded the measured values. This behavior would be expected, as the mathematical model assumed small motions of the proof mass. In a previous analysis, it was shown that the departure from a linearized analysis should occur at larger acceleration amplitudes as the ratio u_p/L_o increased [24]. The measurements shown in Figure 50 are consistent with this analysis.

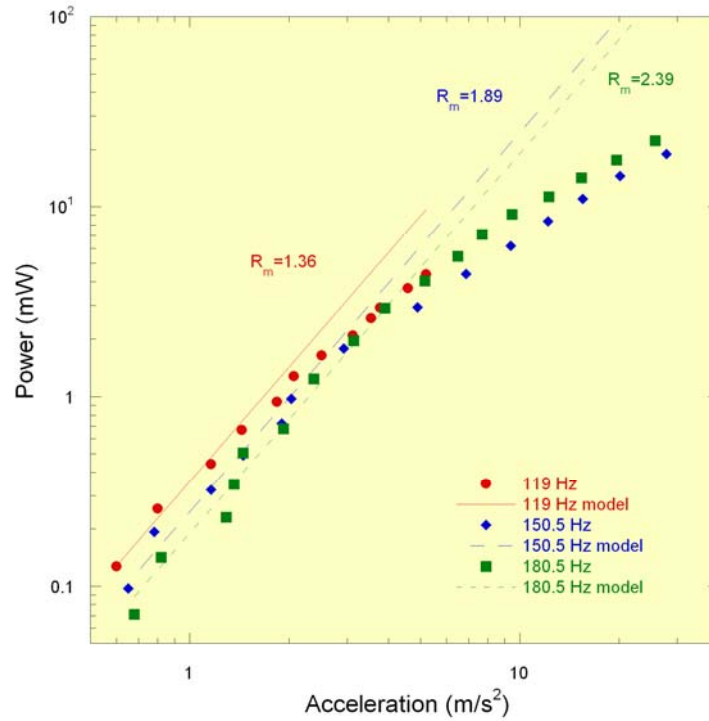


Figure 50 Comparison of predicted power output vs. acceleration for the XMR configured with nominal natural frequencies of 120, 150, and 180 Hz.

Referring to Table 4, the product $RC_o\omega_n$ for each configuration was in the range 2.48-3.19, and according to Equation (4.29) would contribute little to changes in power output. It is apparent that the power output was not identical for the XMR configured for different natural frequencies, but the difference was attributed to a change in mechanical damping. Consequently, these measurements indicate that the power output changes little with the natural frequency of the device, but instead depends predominantly upon the amount of inherent mechanical damping in this device.

Figure 51 shows the results of multiple power measurements of the XMR in incremental steps of approximately 10 Hz. This figure reinforces the notion that power output is less dependent upon frequency as the data merge in the 2-3 m/s² acceleration range. The scatter at lower frequencies is not fully understood. Roll-off of the data at larger acceleration amplitudes is consistent with previously observed behavior.

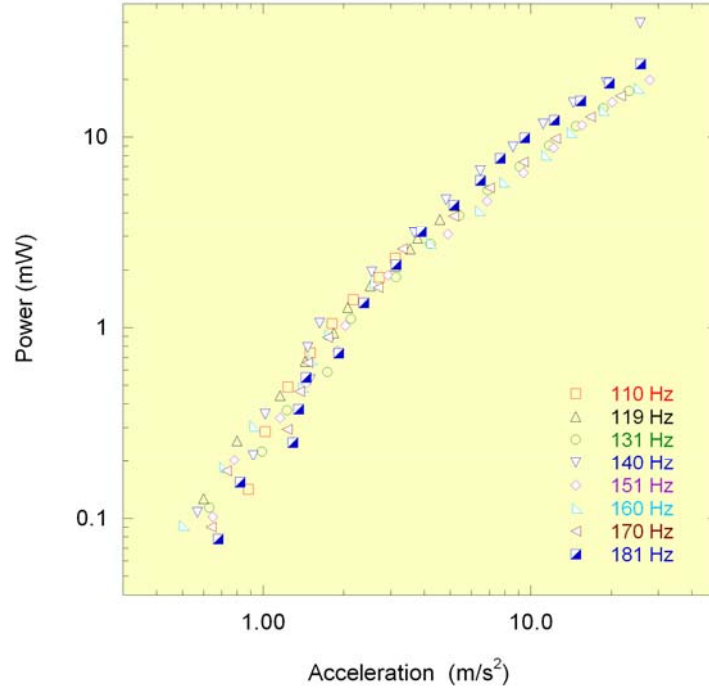


Figure 51 Power output vs. acceleration for the XMR across a broad range of frequencies. Device was constructed with 119 μm films.

Figure 52 shows the results for power vs. acceleration of the XMR using 9 μm films. A comparison is not possible to theoretical values as the range of the impedance analyzer has a minimum frequency of 40 Hz. Consequently, the internal resistance term (R) used to calculate the mechanical damping (R_m) was not available. At this point an *a priori* value for mechanical damping R_m is not available. Rather than calculating an optimal resistance, the experiment was conducted by sweeping a range of resistances on the decade box and measuring the resulting voltage across the load. Power was calculated and plotted to determine the films potential to produce power and to observe any trends.

The results for 40 Hz appear to be much lower than expected. This may be a result of single film operation. The trends of the 48 and 59 Hz curves are in line with previous results where the lower frequency plot lies just above the higher frequency plot, but in general there is not a large digression between power values for a given acceleration. Also observed is the beginning of a power roll-off of the 58 Hz data at about 2 m/s² (this is more evident in other figures such as Figure 41 and Figure 50).

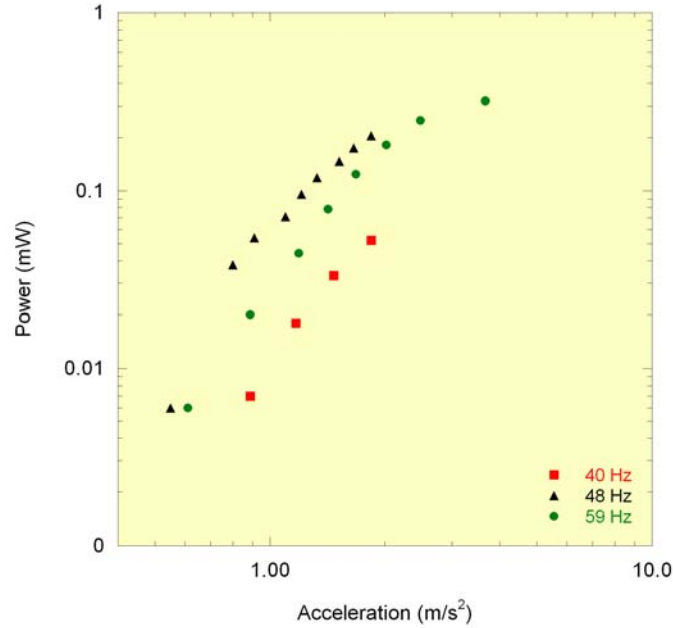


Figure 52 Power output vs. acceleration for the XMR configured with nominal natural frequencies of 40, 48, and 59 Hz. Device was constructed with 9 μm films.

The results for a 28 μm film device are shown in Figure 53 and Table 5. Again, the data matches well with low acceleration amplitudes (<2 m/s²) and diverges beyond. The roll-off is not as well defined (not enough data points) but the divergence would indicate the start of this event. Predicted values for s , Ψ , and C_o ranged from 3-17% compared to the measured values. The predicted coupling factor and stiffness differences were slightly lower than reported for the 119 μm film; consistently exceeding their measured values by approximately 10-17%. The model prediction of natural frequency was improved to within ~5% of the measured value. The mechanical damping, R_m ,

increases with the resonant frequency. The results reinforce confidence in the predicative capabilities of the model.

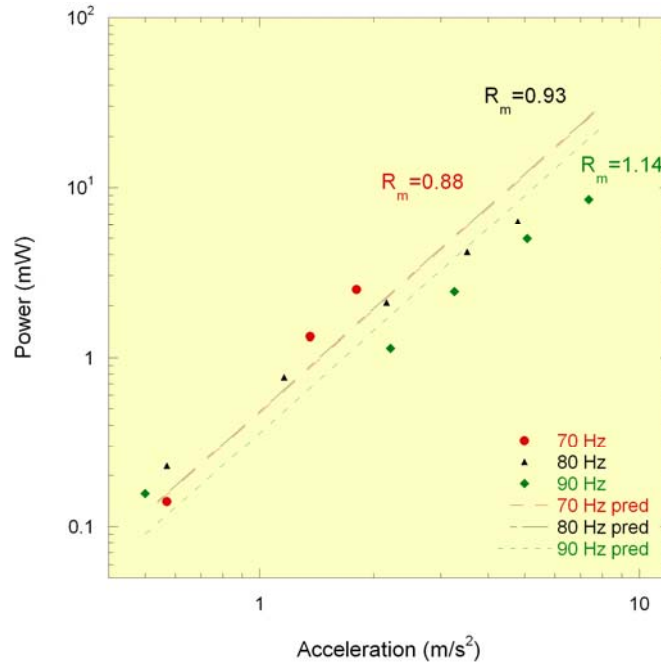


Figure 53 Comparison of predicted power output vs. acceleration for the XMR configured with nominal natural frequencies of 70, 80, and 90 Hz. Device was constructed with 28 μm films.

Table 5 Configuration, impedance measurements, and theoretical predictions for nominal natural frequency of $f_n=70$ Hz, 80 Hz, and 90 Hz. (28 μm film)

Parameter	70 Hz			80 Hz			90 Hz		
	Measured	Theoretical Prediction	% Diff	Measured	Theoretical Prediction	% Diff	Measured	Theoretical Prediction	% Diff
u_p [mm]	3.79			4.41			4.8		
ε_o [%]	1.47			1.98			2.35		
C_o [pF]	1920	2130	11.3	1920	2130	10.9	1980	2130	8
R [M Ω]	2.16	3.09	42.5	1.67	2.41	45.1	1.74	2.53	45.3
L [kH]	200	285	42.5	147	213	45.1	124	181	45.3
C [pF]	24.4	19.1	-21.6	26.9	19.2	-28.7	25.1	19.2	-23.5
k^2 [%]	0.0126	8.89E-03	-29.5	0.0128	8.91E-03	-35.4	0.0125	8.92E-03	-28.6
f_n [Hz]	72	68.1	-5.4	80	78.7	-1.7	90	85.4	-5.2
R_m [Ns/m]	0.884	0.884	0	0.925	9.25	0	1.14	1.14	0
Ψ [mN/V]	0.639	0.535	-16.2	0.746	0.619	-17	0.81	0.672	-17.1
s [kN/m]	16.7	15	-10.6	20.7	20	-3.3	26.2	23.5	-10.1
$R^*C_o^*\omega_n$	1.88	2.82	50	1.61	2.55	58.2	1.95	2.9	48.8

4.9 Uncertainty Discussion

Ordinarily, uncertainty analysis is applied to measured data. In this case, the only value measured in the impedance experiment and the power experiment is voltage which can be determined very precisely. The theoretical model incorporates values that are subject to uncertainty as well. For example, any of the length terms such as L_o , u_p , w , and h have associated measurement uncertainties. The materials parameters used in the calculations are typically the midrange values of the manufacturers reported value so they have uncertainties as well.

Model predictions are compared to measured values to provide confidence in the results expressed by the model. Model predictions rely heavily on the terms for stiffness s , and electromechanical coupling Ψ . Both of these terms are composed of the aforementioned geometric and materials property terms. Following is a derivation of the uncertainty for the theoretical values of s and Ψ for the 120 Hz data in Table 4.

The total uncertainty is determined using the following equation

$$\omega^2 = \sum_n \left(\frac{\partial f}{\partial x_i} \Delta x_i \right)^2, \quad (4.30)$$

where ω is the uncertainty, f is the function, x_i is the parameter, Δx_i is the uncertainty of the x_i parameter and n is the number of independent parameters. When only the geometric terms are included and the measurement uncertainty in each term is $\Delta w=0.5$ mm, $\Delta h=0.02$ mm, $\Delta L_o=0.1$ mm, and $\Delta u_p=0.2$ mm, the uncertainty in s and Ψ are 11,064 N/m and 3.88e-5 N/V respectively. These equate to a 20% uncertainty in s and an 8% uncertainty in Ψ . If the uncertainty for compliance s_{11}^E is included where $\Delta s_{11}^E=1e-10$, the uncertainties increase significantly to 18,692 N/m for s and 1.39e-4 N/V for Ψ , an increase to 34% and 29% respectively. The complete analysis is shown in the appendices. Because s and Ψ appear in many of the other relationships such as C , R , L , and ω_n it is important to recognize the propagation of this uncertainty to those values.

4.10 Conclusions

A tunable vibration harvesting device with an active volume of 21 cm^3 constructed of piezoelectric films supporting a mass of $\sim 82 \text{ g}$ with the ability to vary the resonant frequency was introduced. A model was developed that predicts the device performance from materials properties and device geometry. Results from the predictive model were confirmed with experimental measures with close correlation in the small deflection regime (small accelerations).

Model development included all the geometric and materials properties of the device. Model dynamics were derived from Newton's second law of motion. The results were incorporated with the piezoelectric constitutive equations through an equivalent electrical circuit analysis to derive an equation for power. An optimal power output was predicted and corroborated with experimental data for a variety of frequencies and accelerations. Results at $\frac{1}{2} \text{ g}$ acceleration produced 3 mW to 4 mW at three different frequencies while producing up to 9 mW at just under 1 g acceleration. Model predictions indicated a dependence on both the frequency and mechanical damping. It was shown that the damping has the greatest influence on performance. Experimental data supported this observation.

CHAPTER FIVE

5 EXCESS FILM MODEL DEVELOPMENT

5.1 Introduction

This chapter addresses the development of the excess film model, where the film has additional length beyond $2L_0$. It is imagined that different geometries will allow the XMR to generate more power with the same acceleration input. Additionally, in the event that a composite structure of piezoceramic and metallic foil were to be employed, it is apparent that the structure would not be capable of sustaining the static strains necessary to provide a significant tuning range using the previously described structure. Therefore, a strong motivation for the *xs*-model is to be able to predict the performance and practicality of devices constructed with composite film structures that exceed the initial dimension L_0 such that the device operates in a regime where a tuning range is possible. It is presumed a structure with an angle α approximately 45° would provide a suitable tuning range for films with low strain capabilities. The intention is to develop the equations to predict power and frequency performance when the film angle, α , is closer to 45° . The development follows closely to that presented in the previous chapter, and in fact, the dynamic and electrical portions are identical. Therefore the bulk of this chapter deals with the effects of geometric changes to the device and compares the model results with test results from a prototype device.

5.2 Geometric Effects

In general, the dimensional descriptions from Figure 43 apply. The differences are highlighted in Figure 54 below.

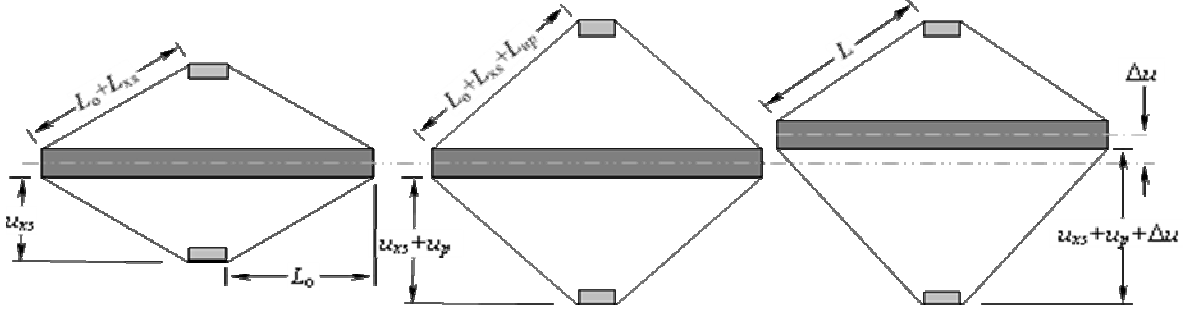


Figure 54 XS model geometric configuration (left) unstrained configuration, (middle) static strained film due to u_p tension, (right) dynamic strained films due to base motion Δu .

In the left image, the unstrained film length is equal to $L_0 + L_{xs}$. In the middle image, the films have been subjected to a static strain through the tensioning or tuning step u_p to a length \bar{L} defined as $L_0 + L_{xs} + L_{up}$. In the image on the right, base motion causes the films to undergo dynamic strain. The film length uses the previously defined term $L = \bar{L} + \Delta L$. Through geometric manipulation, the following terms are derived

$$L_0 + L_{xs} = \sqrt{L_0^2 + u_{xs}^2}, \quad (5.1)$$

$$\bar{L} = \sqrt{L_0^2 + (u_{xs} + u_p)^2}, \quad (5.2)$$

$$L = \bar{L} + \Delta L = \sqrt{L_0^2 + (u_{xs} + u_p - \Delta u)^2}. \quad (5.3)$$

In this section, the total strain calculation and dynamic angle terms will be used to develop the stiffness term, s , and coupling term, Ψ . Recall from the previous chapter Equations (4.5) and (4.6) rewritten here for convenience

$$F_v^+ = \frac{wh}{s_{11}^E} \frac{\Delta L}{L_0} \cos \alpha_u + \frac{d_{31}w}{s_{11}^E} \cos \alpha_u \Delta V_u, \quad (5.4)$$

$$F_v^- = \frac{wh}{s_{11}^E} \frac{\Delta L}{L_0} \cos \alpha_1 - \frac{d_{31}w}{s_{11}^E} \cos \alpha_1 \Delta V_1. \quad (5.5)$$

The Taylor approximations for $\frac{\Delta L}{L_0} \cos \alpha$ and $\cos \alpha$ utilizing the *total strain* will be used. The

same force equations are used but the result is different. See *Mathematica* derivation “RXMR xs model w dynamic alpha.nb” in the appendices for details. The total force F_T is written as

$$F_{TOT} = 2F_v^+ + 2F_v^- . \quad (5.6)$$

Substitution of the linear Taylor approximation terms and simplification result in an equation for F_{TOT}

$$F_{TOT} = -\frac{4wh}{s_{11}^E} \frac{L_0 (u_p + u_{xs})^2 \sqrt{1 + \left(\frac{u_p + u_{xs}}{L_0}\right)^2} + L_0^3 \left(\sqrt{1 + \left(\frac{u_{xs}}{L_0}\right)^2} - \sqrt{1 + \left(\frac{u_p + u_{xs}}{L_0}\right)^2} \right)}{L_0 \sqrt{1 + \left(\frac{u_{xs}}{L_0}\right)^2} L_0^3 \left(1 + \left(\frac{u_p + u_{xs}}{L_0}\right)^2 \right)^{\frac{3}{2}}} \Delta u$$

$$+ \frac{2wd_{31}}{s_{11}^E} \frac{L_0 \sqrt{1 + \left(\frac{u_{xs}}{L_0}\right)^2} (V_L + V_U) \left((u_p + u_{xs})^3 + L_0^2 (u_p + u_{xs}) \right) + L_0 \sqrt{1 + \left(\frac{u_{xs}}{L_0}\right)^2} L_0^2 (V_L - V_U) \Delta u}{L_0 \sqrt{1 + \left(\frac{u_{xs}}{L_0}\right)^2} L_0^3 \left(1 + \left(\frac{u_p + u_{xs}}{L_0}\right)^2 \right)^{\frac{3}{2}}} . \quad (5.7)$$

Collecting terms and comparing the result to

$$F_T = 2F_v^+ + 2F_v^- = -s\Delta u + \Psi\Delta V_U + \Psi\Delta V_L \quad (5.8)$$

provides an expression for the stiffness s , written as

$$s = \frac{4wh}{s_{11}^E} \frac{L_0 (u_p + u_{xs})^2 \sqrt{1 + \left(\frac{u_p + u_{xs}}{L_0}\right)^2} + L_0^3 \left(\sqrt{1 + \left(\frac{u_{xs}}{L_0}\right)^2} - \sqrt{1 + \left(\frac{u_p + u_{xs}}{L_0}\right)^2} \right)}{L_0 \sqrt{1 + \left(\frac{u_{xs}}{L_0}\right)^2} L_0^3 \left(1 + \left(\frac{u_p + u_{xs}}{L_0}\right)^2 \right)^{\frac{3}{2}}} , \quad (5.9)$$

which can be reduced slightly to

$$s = \frac{4wh}{s_{11}^E} \frac{\left(u_p + u_{xs}\right)^2 \sqrt{1 + \left(\frac{u_p + u_{xs}}{L_0}\right)^2} + L_0^2 \left(\sqrt{1 + \left(\frac{u_{xs}}{L_0}\right)^2} - \sqrt{1 + \left(\frac{u_p + u_{xs}}{L_0}\right)^2} \right)}{\sqrt{1 + \left(\frac{u_{xs}}{L_0}\right)^2} L_0^3 \left(1 + \left(\frac{u_p + u_{xs}}{L_0}\right)^2\right)^{\frac{3}{2}}}. \quad (5.10)$$

Likewise, the expression for the coupling term Ψ is written as

$$\Psi = \frac{2wd_{31}}{s_{11}^E} \frac{\left(\left(u_p + u_{xs}\right)^3 + L_0^2 \left(u_p + u_{xs}\right)\right)}{L_0^3 \left(1 + \left(\frac{u_p + u_{xs}}{L_0}\right)^2\right)^{\frac{3}{2}}}, \quad (5.11)$$

which simplifies to

$$\Psi = \frac{2wd_{31}}{s_{11}^E} \frac{\left(u_p + u_{xs}\right)}{L_0 \sqrt{1 + \left(\frac{u_p + u_{xs}}{L_0}\right)^2}}. \quad (5.12)$$

It is seen that there is an additional term beyond the s and Ψ equivalences used in the previous derivations that contains values of both Δu and ΔV_x

$$XScoupling = \frac{2wd_{31}}{s_{11}^E} \frac{L_0 \sqrt{1 + \left(\frac{u_{xs}}{L_0}\right)^2} L_0^2 (V_L - V_U) \Delta u}{L_0 \sqrt{1 + \left(\frac{u_{xs}}{L_0}\right)^2} L_0^3 \left(1 + \left(\frac{u_p + u_{xs}}{L_0}\right)^2\right)^{\frac{3}{2}}}, \quad (5.13)$$

which can be reduced to

$$XScoupling = \frac{2wd_{31}}{s_{11}^E} \frac{(V_L - V_U) \Delta u}{L_0 \left(1 + \left(\frac{u_p + u_{xs}}{L_0}\right)^2\right)^{\frac{3}{2}}}. \quad (5.14)$$

Because of the nonlinear nature of this term (a function of both Δu and V_x), it is assumed to not significantly contribute to the model and will be neglected at this point consistent with the approximation.

5.3 Development of Power Equations

The development of the power equations follows directly from the previous model development as well as the optimal resistance term because the electrical mechanical equivalent model has not changed. What has changed are the values for C_o , R , and ω in the resulting equations. For convenience, the developed equations are shown

$$\Pi = \frac{1}{2} \frac{1}{R_L} \frac{1}{\left(\frac{R}{R_L}\right)^2 + 2\left(\frac{R}{R_L}\right) + (RC_o\omega_n)^2} \frac{m^2 A^2}{\Psi^2}, \quad (5.15)$$

$$R = \frac{R_m}{\Psi^2}, \quad (5.16)$$

and

$$R_{L,o} = \frac{R}{\sqrt{1 + (RC_o\omega_n)^2}}. \quad (5.17)$$

Substituting the optimal resistance equation (5.17) into the power equation (5.15) results in

$$\Pi_o = \frac{1}{4R_m} \frac{1}{\sqrt{1 + (RC_o\omega_n)^2} + 1} m^2 A^2. \quad (5.18)$$

The geometric changes associated with the *xs*-model impact the equations for R and C_o minimally, however ω_n is changed significantly. Changes to C_o are limited to the increased area of the electrodes due to the addition of film over the relatively planar geometry of the RXMR in Chapter 4. Resistance changes are seen due to the coupling term Ψ . Frequency has a significant change because the excess film affects the *no strain* position. If one were to substitute an ideally linear elastic material in place of the current material that undergoes changes in modulus due to strain, it may be expected that the

previous model derivation for frequency would still apply. The revised equations for these variables which use the dynamic form of $\cos\alpha$ are shown here

$$\omega = \sqrt{\frac{s}{m}} = \sqrt{\frac{4wh}{ms_{11}^E} \frac{\left(u_p + u_{xs}\right)^2 \sqrt{1 + \left(\frac{u_p + u_{xs}}{L_0}\right)^2} + L_0^2 \left(\sqrt{1 + \left(\frac{u_{xs}}{L_0}\right)^2} - \sqrt{1 + \left(\frac{u_p + u_{xs}}{L_0}\right)^2} \right)}{\sqrt{1 + \left(\frac{u_{xs}}{L_0}\right)^2} L_0^3 \left(1 + \left(\frac{u_p + u_{xs}}{L_0}\right)^2\right)^{\frac{3}{2}}}}, \quad (5.19)$$

$$C_0 = \frac{\epsilon_{33}^T \left(1 - \frac{d_{31}^2}{s_{11}^E \epsilon_{33}^T}\right) w \sqrt{L_0^2 + u_{xs}^2}}{h}, \quad (5.20)$$

and

$$R = \frac{R_m}{\Psi^2} = \frac{R_m}{\left(\frac{2wd_{31}}{s_{11}^E} \frac{(u_p + u_{xs})}{L_0 \sqrt{1 + \left(\frac{u_p + u_{xs}}{L_0}\right)^2}} \right)^2}. \quad (5.21)$$

Substitution and simplification of the terms above into the power equation provides an equation for power written as a function of materials properties and geometry as follows

$$\Pi_o = \frac{m^2 A^2}{2R_m} * \left[\frac{1}{2 + 2 \sqrt{1 + \frac{R_m^2 s_{11}^E \sqrt{L_0^2 + u_{xs}^2} \sqrt{L_0^2 + (u_p + u_{xs})^2} \left(-(u_p + u_{xs})^2 \sqrt{L_0^2 + (u_p + u_{xs})^2} + L_0^2 \left(\sqrt{L_0^2 + u_{xs}^2} - \sqrt{L_0^2 + (u_p + u_{xs})^2} \right) \right) \left(d_{31}^2 - s_{11}^E \epsilon_{33}^T \right)^2}}{4d_{31}^4 h m (u_p + u_{xs})^4} \omega} \right]. \quad (5.22)$$

A plot of the acceleration normalized power equation for varying values of u_{xs} is shown in Figure 55. The geometric and materials terms are held constant and are taken from the 120 Hz data set in Table 4 from the previous chapter. The material is 119 μm PVDF film with an 82.3 g mass.

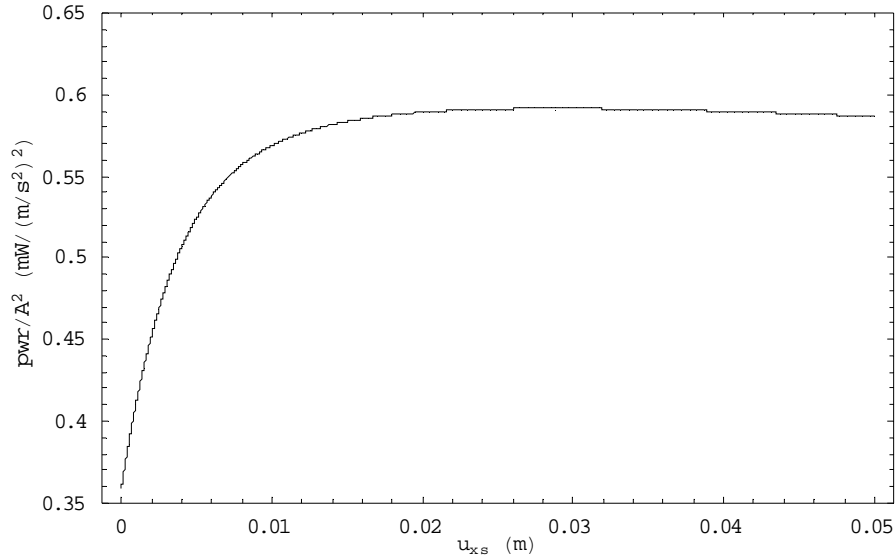


Figure 55 Plot of power function vs. u_{xs} . Acceleration normalized power variation with changes in excess film length for a device configured with 119 μm film, 82.3 g mass, and dimensions of $L_0= 22$ mm, $w= 24$ mm, and $u_p= 3.59$ mm.

The plot in Figure 55 indicates that the power achieves a maximum at a value of $u_{xs}=L_0=22$ mm that corresponds with an $\alpha=45^\circ$. Once beyond this point, the power stays essentially constant. The general shape of the curve can be explained based on the changes in geometry that occur with incremental additions to the film length. When $u_{xs}=0$, the smallest increase allows the films to be affected by the vertical force from mass oscillations. Further increases to u_{xs} allow a larger portion of the vertical motion to come to bear on the films, increasing strain and producing more power. The steep initial slope continuously decreases as more film is added. This would be expected as the change to the geometry requires an increasing amount of film to generate another degree of angle change.

The plot shown below in Figure 56 compares the $RC_0\omega_n$ term to changes in excess film length, u_{xs} . The term $RC_0\omega_n$, defined by others as the dimensionless time constant, [57, 58] is seen to decrease dramatically with the smallest increase in film length beyond $u_{xs}=0$. This response to geometry change is clearly the explanation to the change in power as the term is prominent in the power equation, Equation (5.18), and the mechanical damping term R_m is held constant. This provides insight into the effect geometry plays on the power output. In practice, measured power is likely to diminish because

of the strong influence that R_m has on power output and as the results in Figure 32 demonstrate, significant geometry changes cause significant changes in R_m .

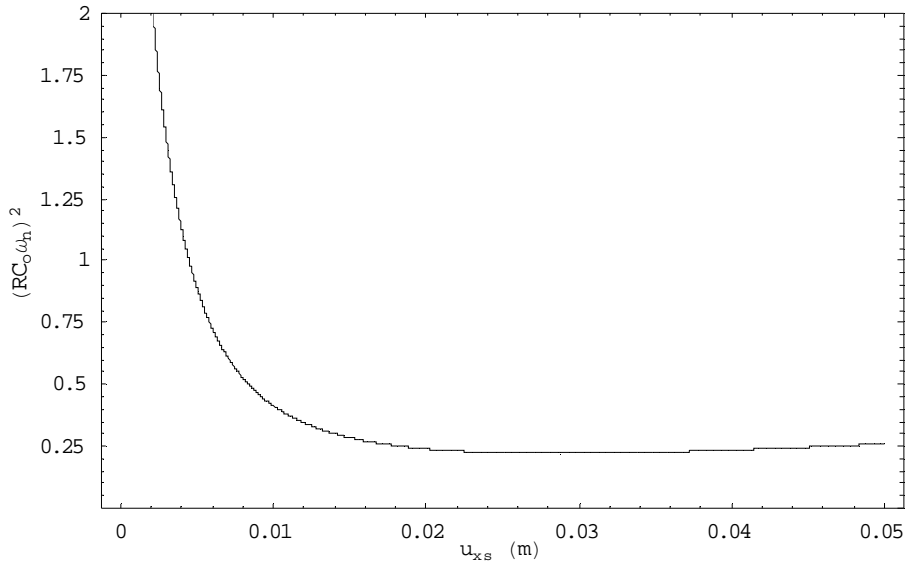


Figure 56 Dimensionless term $RC_0\omega_n$ vs. u_{xs} . Variation of the $RC_0\omega_n$ term with additions to the film length.

The response of frequency to changes in film length from Equation (5.19) is shown in Figure 57. Frequency appears to reach a maximum at the $\alpha=45^\circ$ condition. It is assumed that the change in geometry allows a greater portion of the force vector due to mass oscillations to come to bear on the films and that continues to increase, although at a diminishing rate, until the $\alpha=45^\circ$ point.

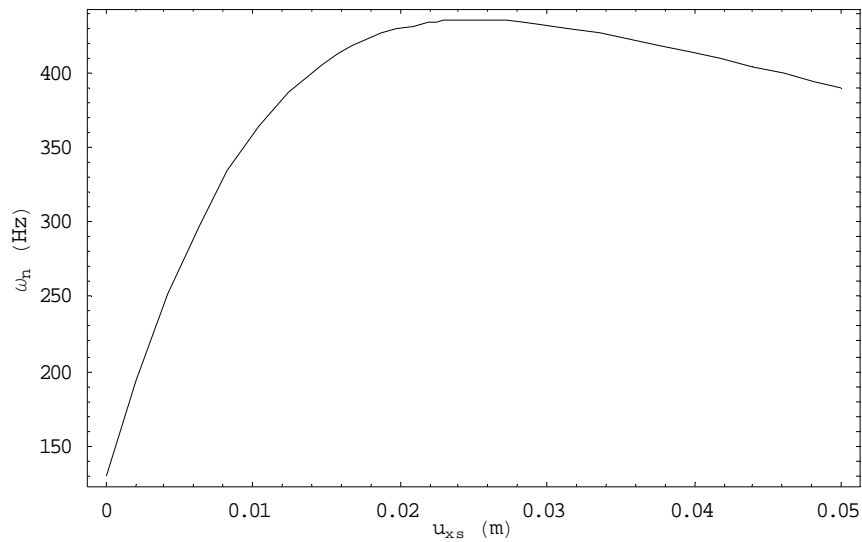


Figure 57 Resonant frequency response to changes in excess film length.

The explanation for frequency decrease beyond this point is explained by the change in device stiffness, s , shown in Figure 58. This is a plot of stiffness s , defined by Equation (5.10) and because mass is constant, is the principle contributor to the change in resonant frequency as shown in Equation (5.19). Physically this shows that with a constant pretension u_p , additional length to the films reduces the strain induced by the motion of the mass which manifests itself as a reduction in the device stiffness.

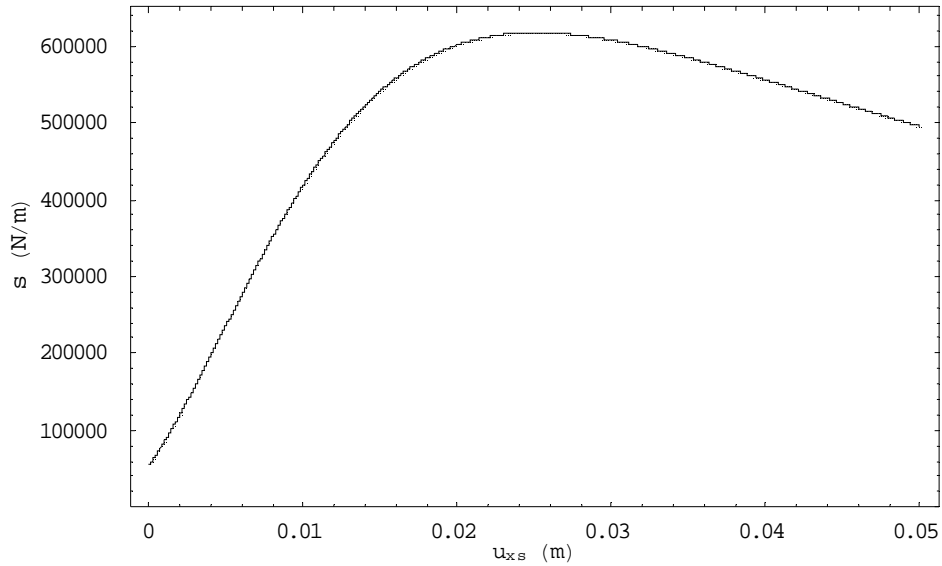


Figure 58 Device stiffness vs. changes in excess film length.

An example of the change due to variation in u_p is shown in Figure 59. Here u_{xs} is allowed to sweep a range that captures the $\alpha=45^\circ$ condition with values of $u_p=3, 4,$ and 5 mm corresponding to the red, green and black curves in the figure. The values for u_p are larger than real world dimensions but are used to provide some clarity in the plot. The general trend is maintained but at very high values of u_{xs} the curves join indicating the reduced role of u_p on the total stiffness value of the structure. Inspection of Equation (5.10) will confirm this. The curve also indicates that each resonant frequency can be achieved by two values of u_{xs} and that there is a maximum frequency that the device can achieve.

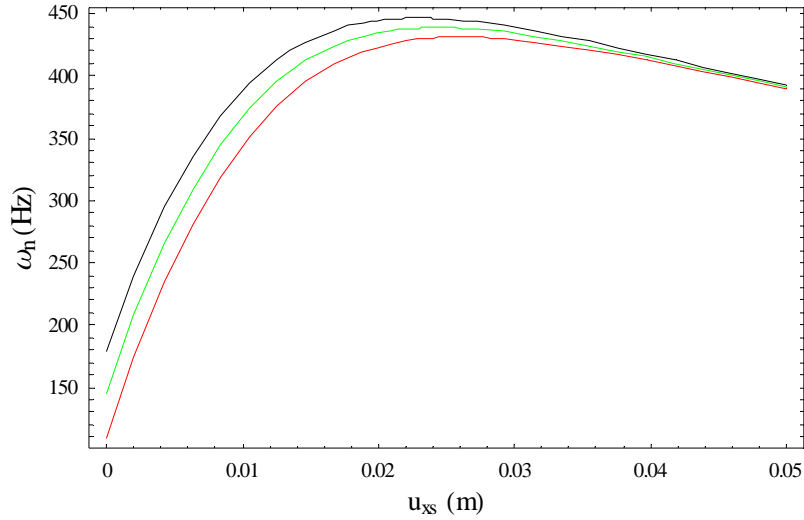


Figure 59 Predicted frequency response of x_s -model versus changes in u_{xs} at several values of u_p . (red (long dash): $u_p=3$ mm, green (short dash): $u_p=4$ mm, black (solid): $u_p=5$ mm)

Chapter 4 developed a model that demonstrated a linear response of frequency to changes in u_p . The model used an approximation for the included angle in the device geometry. The model presented in this chapter allows the angle to change with the dynamics of the structure. Figure 60 shows the change in resonant frequency when u_p sweeps a range of values with fixed lengths of u_{xs} . In this case, $u_{xs}=0, 10,$ and 20 mm corresponding to the red, green and black curves in the figure. What is most curious is the variation of frequency with respect to u_p . When $u_{xs}=0$, the condition presented in Chapter 4, there is a large linear region as the experimental data show, but beyond a point ($u_p \sim 10$ mm) the plot deviates and ultimately appears to reach a maximum. Increases in film length due to u_{xs} cause the transition from the linear to the curved portion to occur much sooner. In the case of $u_{xs}=20$ mm, the linear region is very small, from about 380 Hz to 440 Hz. In addition, the maximum operating frequency diminishes with the increases to u_p .

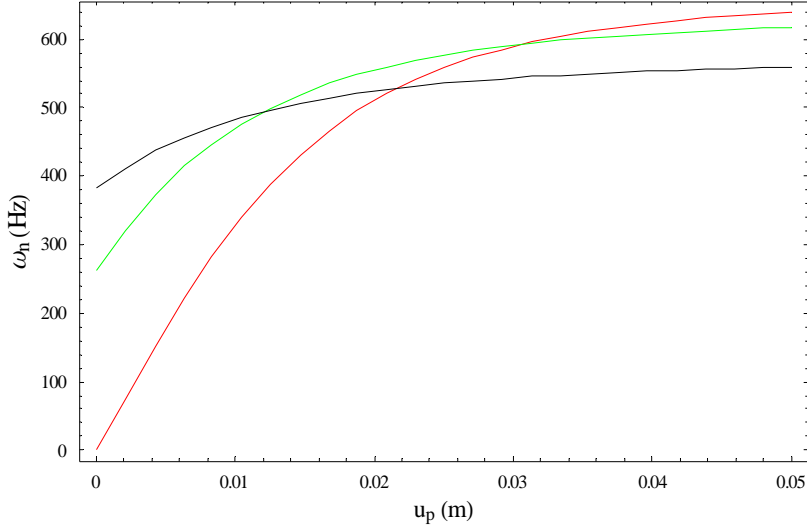


Figure 60 Predicted frequency response of xs -model versus changes in u_p at several values of u_{xs} . (red (long dash): $u_{xs}=0$, green (short dash): $u_{xs}=10$ mm, black (solid): $u_{xs}=20$ mm)

5.4 Experimental Results of Excess Model

In order to verify the accuracy of the theoretical model developed, a device was constructed using the same mass and film material as the device presented in the last chapter. The overall dynamic mass increased slightly from 82.3 g to 82.9 g. This change was attributed to the increase in film material. Similar to the previous device, 119 μm thick Measurement Specialties PVDF film was used. The difference in film length, L_{xs} , is 8.9 mm. A more practical term for use in the model is the change in dimension in the u direction, u_{xs} , and it is convenient to calculate it with the following

$$u_{xs} = L_o \sqrt{\left(1 + \frac{L_{xs}}{L_o}\right)^2} - 1. \quad (5.23)$$

Substituting $L_o=22$ mm with $L_{xs}=9$ mm returns a value of $u_{xs}=21.89$ mm or 22 mm. The static strain, ϵ_{stat} , developed by pretensioning the films a distance u_p is approximated by

$$\epsilon_{stat} \approx \frac{u_{xs} u_p}{L_o^2 \left(1 + \left(\frac{u_{xs}}{L_o}\right)^2\right)}. \quad (5.24)$$

The device was connected to an impedance analyzer to measure the general properties discussed previously ($R, L, C_o, C, k^2, \omega_n$). These values are used to calculate some of the “measured” values using the relationships; $L = m/\Psi^2$, $C = \Psi^2/s$, $R = R_m/\Psi^2$, and $k^2 = C/(C + C_o)$. The results are shown in the Table 6.

Small errors in measuring the geometric terms and assumptions of materials properties as described in Chapter 4, lead to larger errors that propagate through some of the values. This is particularly evident in the large difference between measure Ψ (from $L = m/\Psi^2$) and calculated Ψ which uses Equation (5.12) and s , derived from measured C and the relationship above. The theoretical column uses the developed equations to calculate the terms s , Ψ , and C_o . The relationships listed above were used to calculate the remaining predicted values (they are the measured quantities from the impedance analyzer).

The theoretical resistance R is not shown as it depends on the damping term which is difficult to quantify. The only relationship is shown above and would yield a circular calculation as the measured R from the impedance data was used to calculate R_m . Certainly, R could be calculated by using the theoretical Ψ term with the measured R_m , however this results in the already demonstrated difference between Ψ with no new insight.

It should be noted that the impedance data for 354 Hz appears outside the expected. It may be that there was a poor connection between the lead wire and the film. This is particularly obvious when a comparison is made between the measured values of C_o at the three settings. Ideally, C_o should remain almost constant, any change in its value is due to the small change in film thickness, h , and an increase in film area due to the strain imposed by u_p . It is noted that the value remains the same for the 332 Hz and 370 Hz measurements but is double the value for the remaining experiment. This indicates the measurement captured just a single film element pair.

Table 6 Configuration, impedance measurements, and theoretical predictions for nominal natural frequency of $f_n=332$ Hz, 354 Hz, and 370 Hz. (119 μm film).

Parameter	332 Hz			354 Hz			370 Hz		
	Measured	Theoretical Prediction	% Diff	Measured	Theoretical Prediction	% Diff	Measured	Theoretical Prediction	% Diff
u_p [mm]	0			0.1			0.2		
ϵ_o [%]	0			0.23			0.45		
C_o [pF]	643	684	6.3	1260	684	-45.8	642	684	6.7
R [M Ω]	5.12			6.10			6.83		
L [kH]	77.1	18.0	-76.7	91.8	17.9	-80.5	85.3	17.8	-79.1
C [pF]	3.3	9.1	177	2.6	9.1	246	2.9	9.1	216
k^2 [%]	0.0051	0.0132	158	0.0021	0.0131	526	0.0045	0.0131	192
f_n [Hz]	316	393	25	323	394	22	321	396	23
R_m [Ns/m]	5.51	23.6	329	5.51	28.3	414	6.64	18.2	174
Ψ [mN/V]	1.04	2.15	107	0.95	2.15	127	0.99	2.16	119
s [kN/m]	326	505	55	342	509	49	337	512	52
$R^*C_o^*\omega_n$	6.53	8.65	32	15.6	10.3	-34	8.84	6.63	-25

The measured power output shown in Figure 61 does not reflect the change in capacitance that was detailed in the previous paragraph, although the theoretical value appears low and would certainly be affected by a change in this term. The motion of the device during the dynamic measurement (rather than the small motions imposed by the impedance analyzer) appears to have completed the circuit.

Theoretical calculations for power use Equations (5.18), (5.19), and (5.20). R_m was calculated from $R_m=R\Psi^2$, using the measured value for R at a number of accelerations to generate the damping term. The results match the measured data very well. Unlike the predicted values, it is the lowest frequency data set of the measured data that appears out of place. This may be attributed to an experimental condition with no pretension, i.e. $u_p=0$.

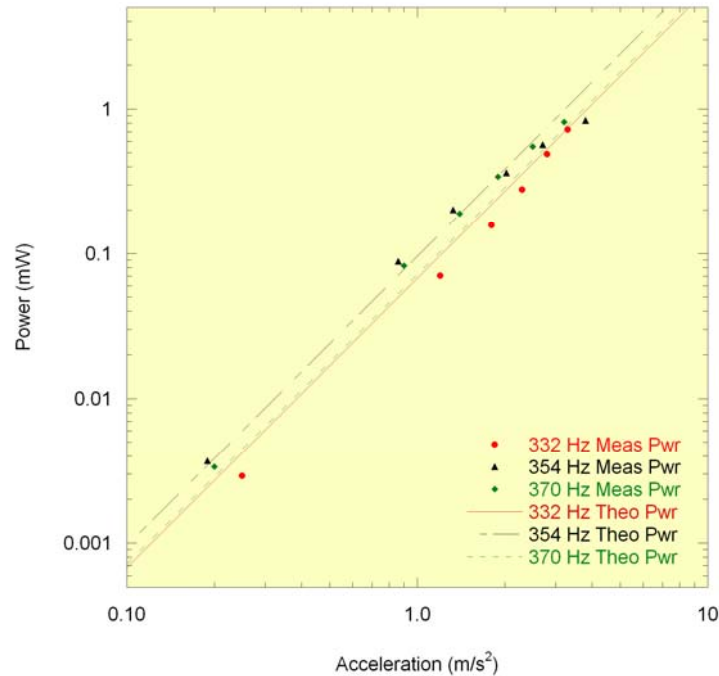


Figure 61 Measured power vs. acceleration data with theoretical predictions for an xs-model device.

Another series of data was taken using the same configuration and setup. The results are shown in Figure 62 with impedance and geometry data shown in Table 7. Similar differences are seen in the reported data as shown in the previous set. Note that the problem with C_o does not appear. Again, the theoretical power appears to closely match the measure result. This demonstrates the significance of the damping term R_m . While the predicted values of the terms R , C_o , and ω_n vary significantly with the measured values, their role in predicting power is limited to the contribution in the radical of the denominator. Another observation is the duplication of resonant frequency at 378 Hz with two different settings of u_p . This appears to be the upper tuning limit. This point was about as tight as the films would go although the geometry of the device was capable of further adjustment. It may be that this exceeded the elastic limit of the material and induced some plastic deformation.

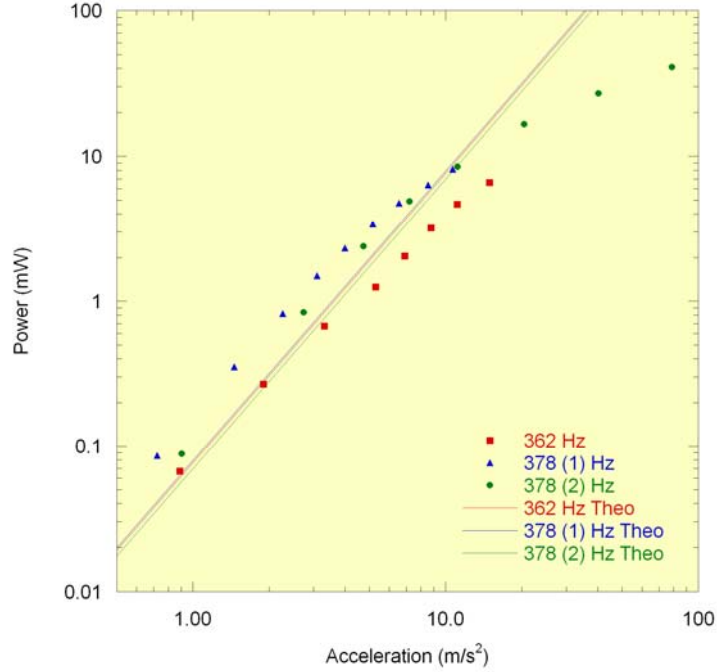


Figure 62 Measured power vs. acceleration data with theoretical predictions for an xs-model device.

Table 7 Configuration, impedance measurements, and theoretical predictions for nominal natural frequency of $f_n=362$ Hz, and two at 370 Hz. (119 μm film).

Parameter	362 Hz			378 (1) Hz			378 (2) Hz		
	Measured	Theoretical Prediction	% Diff	Measured	Theoretical Prediction	% Diff	Measured	Theoretical Prediction	% Diff
u_p [mm]	0.1			0.365			.430		
ε_o [%]	0.45			0.83			0.98		
C_o [pF]	644	684	6.3	650	684	5.3	658	684	4
R [M Ω]	6.39			4.44			6.76		
L [kH]	82.6	18	-78	58.8	17.7	-70	82.5	17.6	-79
C [pF]	3.0	9.1	210	3.6	9.1	153	2.9	9.1	213
k^2 [%]	.0045	.0131	192	.0055	.0131	138	.0044	.0131	197
f_n [Hz]	323	396	22	347	398	15	326	398	22
R_m [Ns/m]	6.42	29.76	364	6.27	20.84	233	6.79	31.78	368
Ψ [mN/V]	1	2.15	115	1.19	2.14	81	1	2.16	116
s [kN/m]	342	512	50	393	517	32	348	520	50
$R^*C_o^*\omega_n$	8.36	10.9	30	6.29	7.6	21	9.1	11.6	27

Figure 63 shows the results from several data collections of the *xs*-device. The device shows consistency over the runs although evidence of creep can be seen. The data set shown as 370 Hz in the blue curve has the same u_p setting as the 362 Hz red data curve. In fact the runs were consecutive with a span of 3 weeks between them. Power roll-off is evident at the higher accelerations (about 7 m/s^2). Data was collected at accelerations of almost 80 m/s^2 and generated almost 45 mW . The RXMR seemed to run well at this setting.

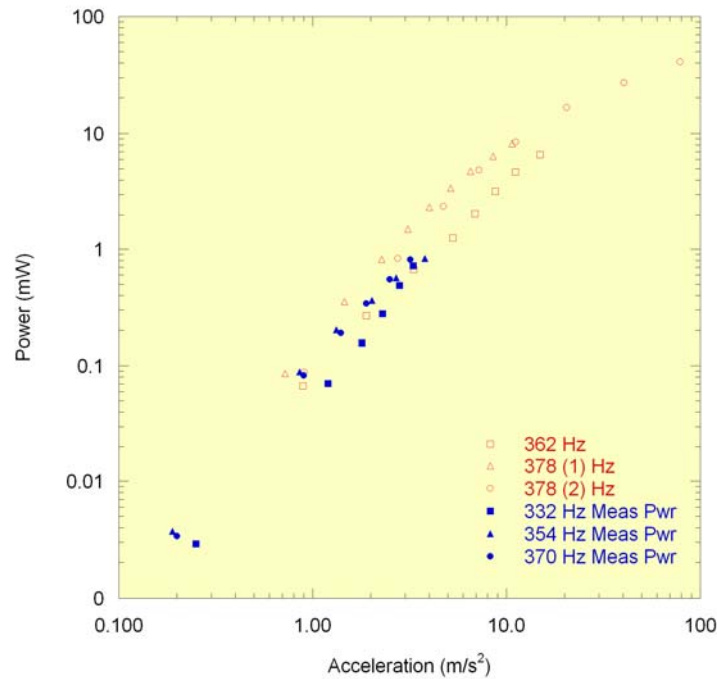


Figure 63 Power vs. acceleration plot of *xs*-model device from two separate data runs. The dimension u_p is the same between the 354 Hz measurement and the 362 Hz measurement indicating potential creep. Blue data set was taken approximately two weeks before the red set. Two different u_p settings generated 378 Hz data in the latter set.

A final comparison is shown in Figure 64 between the *xs*-model and the regular model. Both devices used the same mass and films, and were statically strained about the same range. The power produced by the higher frequency *xs*-model device is slightly below the regular model XMR, but certainly not as significant a reduction as literature would suggest with the inverse relationship between power and frequency. The plot also demonstrates that the initial perception of higher power output at a perhaps more favorable geometry is not necessarily true. However, the model development

does address the other issue of interest, that of excess material length that may be required for a low strain capable piezoceramic materials system.

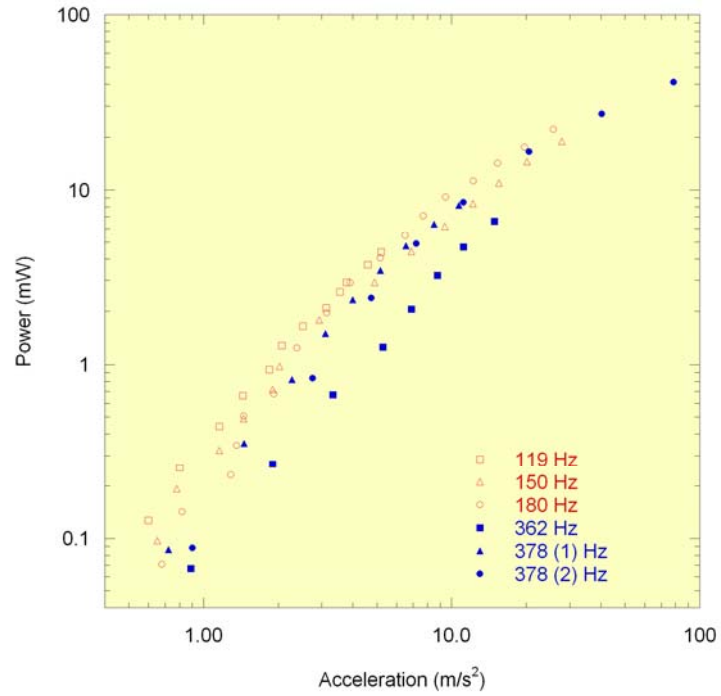


Figure 64 Power vs. acceleration plot of xs-model device (blue) contrasted with the regular model (red). Mass and film thickness are the same. Film length is the significant variation between the two results.

CHAPTER SIX

6 APPLICATIONS OF THE DEVELOPED MODELS TO DESIGN

6.1 Introduction

This chapter is devoted to the application of the derived models to design devices for a variety of installations. The device designs will still have the adjustable resonant frequency feature and the idea is to center the device frequency on the expected resonant frequency of an installation so that there is still tuning above and below the center frequency. This work has focused on generating energy using a vibrating mass driving piezoelectric elements and, in the scheme of energy harvesting for remote sensing, is a battery replacement or storage charger. No effort has been placed on design or improvement of energy conversion and optimization, or storage techniques. Typical installations of sensors will have a load requirement of their own and that value can be used in the future to direct device design.

As stated earlier, many opportunities are available for the remote monitoring of equipment and structures. Of particular interest are sensors that can monitor a variety of conditions in infrastructure. Other applications that can contribute significant cost savings are corrosion monitors in military and civilian airframes. Still other installations, such as bearing condition monitors, can help minimize downtime on critical pieces of production equipment or printing lines. Therefore, the development throughout this chapter will focus on a very low frequency (0.5-3.3 Hz) [14] harvester for a building, a low frequency harvester for a helicopter installation (~20-25 Hz) [59], a device that captures 60 Hz frequencies as might be seen on the electric motors on many production equipment installations and a clothes dryer with requirements reported by Hu *et. al* (121 Hz, 3.5 m/s²) [54].

Any number of criteria may be used as the design constraints of a device; from power output, frequency range, weight, or volume, or any combination of these. For simplicity, device volume will be used for the following designs which will run from a small device, about the size of a matchbox, a

low profile device the size of a CD jewel case, and a large volume device about the size of a ½ pint milk carton. Given the device volume constraint, the design process will determine the expected frequency range and power output for a variety of input accelerations.

6.2 Matchbox Device

Given the dimensions as 15 mm x 30 mm x 50 mm, the device in Figure 65 uses tungsten for the mass and PVDF films as the active piezoelectric elements. The regular model (Chapter 4) is used to determine the predicted outputs as the low profile of the device does not lend itself to the *xs*-model (Chapter 5).

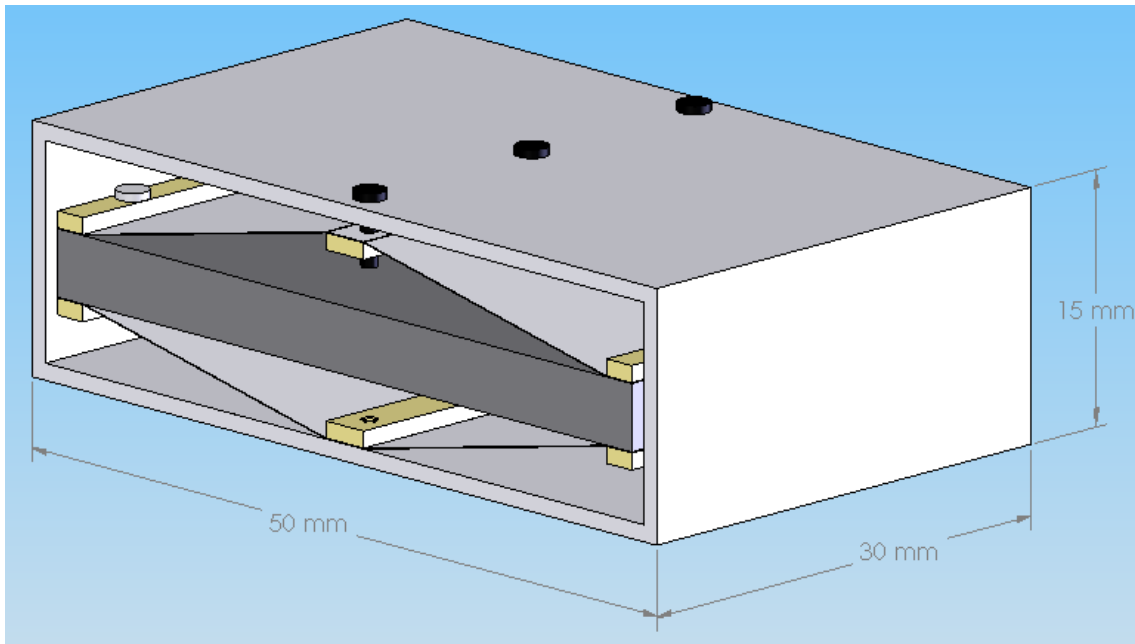


Figure 65 Model of the matchbox size device.

The four clamp bars that secure the film to the tungsten mass and the two rails that exert the tension into the films are metallic elements and act as conductors in the extraction of power from the device. The clamp bars are arranged so they contact the outer electrode surfaces of the device and conduct charge through the screws into the mass. This makes the outer electrode surfaces electrically

common. The rails also are arranged so they contact the inner electrode surfaces. They can be isolated from one another through several schemes:

- the screws that secure the lower rail and move the upper rail are composed of an insulating material such as nylon and an insulation strip is applied between the lower film and the case.
- the case is constructed of an insulating material.
- the case is constructed of metal but one set of (upper or lower rail) screw holes are lined with insulating features such as nylon bushings and washers.

In the first two cases, wires attached to the rails extract the power generated from motion of the device. In the third example, the case itself is common to one electrode and forms one conductor, then power can be extracted from a wire attached to either the upper rail or the isolated upper rail screws.

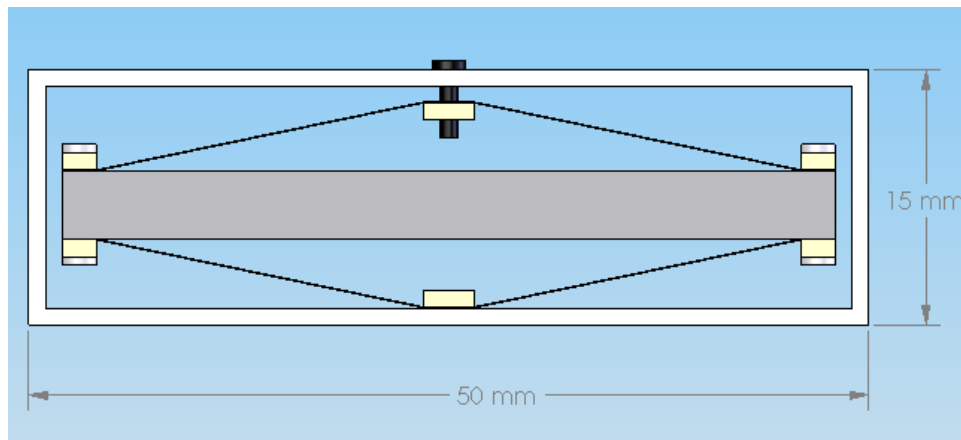


Figure 66 Front view of the matchbox device showing device configuration and clearance.

Figure 66 shows the front view of the device in order to clarify the relationship between the different components. The case places an upper limit on the tuning range (through changes in u_p) of the device but it should be noted that a strain of 2.63% is calculated for the maximum u_p value possible for this device (see Table 8). Generous clearance is shown between the device and the sidewalls of the enclosure to minimize drag potential (as may occur if the mass were to shift sideways) and air damping. The partial section view in Figure 67 shows additional relationships between the components such as the rail screws and film clamps.

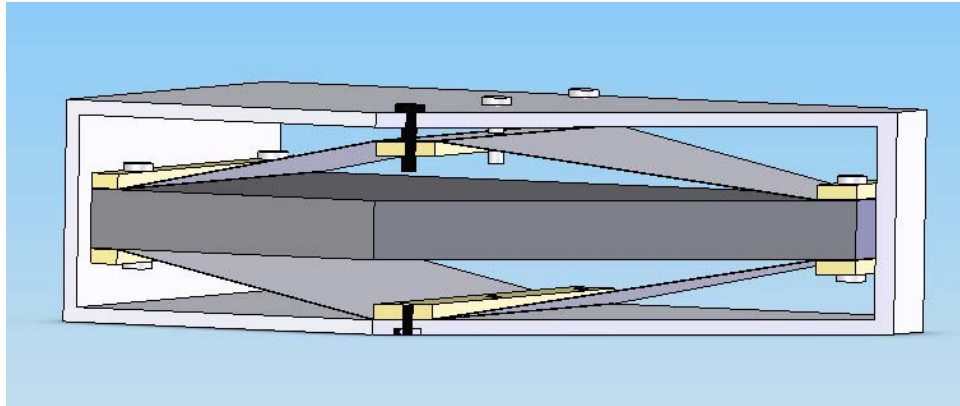


Figure 67 Partial section view of the matchbox device.

The device constraints were used to iterate the final design. The final dimensions were used to predict the power output shown in Figure 68. The plot shows predictions for two different configurations, one using 28 μm PVDF film (31, 62, and 92 Hz) and the other with 119 μm PVDF film (65, 128, and 190 Hz). The power predictions are similar to experimental results from Chapter 4 which is to be expected. This design is similar in size to the original XMR but utilizes a larger mass, in this case 107 g. The active area of a film element in the XMR is 22 mm x 24 mm while this device is 19.5 mm x 30 mm. Power is calculated using a constant value for $R_m=1.7$ Ns/m.

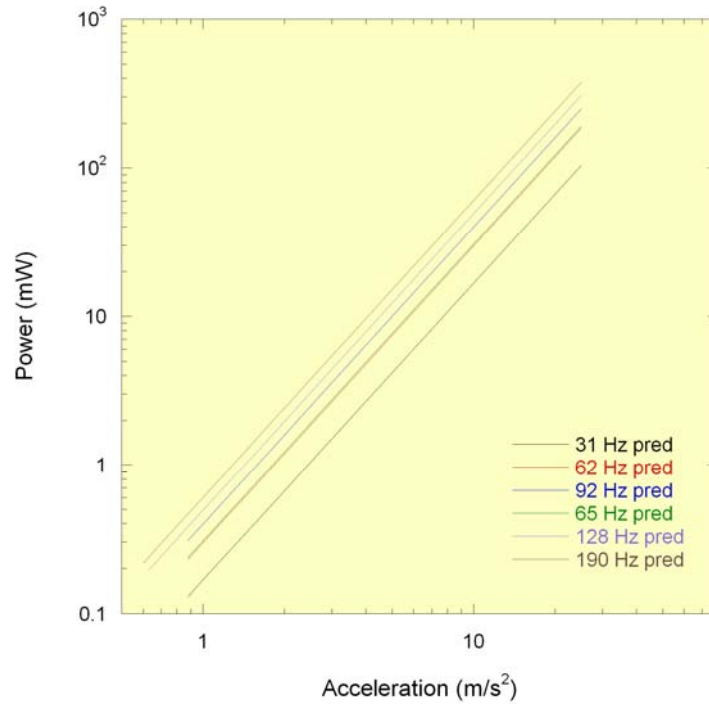


Figure 68 Predicted power vs. acceleration for the matchbox device showing performance from a device constructed with two sizes of PVDF film. Results of 31, 62 and 92 Hz are from 28 μm film, the remaining are from 119 μm film.

Table 8 shows some trends that can be compared to previous experimental and theoretical results. The change in resonant frequency increases with increases in device geometry, u_p , which is consistent with previous data and results from the increasing value of device stiffness, s . Device stiffness also shows a strong dependence upon the material thickness. The electromechanical coupling term, Ψ , is shown to be independent of material thickness but trends up with increases in geometry.

Table 8 Predicted results for the matchbox device at various u_p dimensions and film thicknesses. Calculations assume a constant R_m value of 1.7 Ns/m.

Parameter	u_p [mm] 1.5		u_p [mm] 2.25		u_p [mm] 3	
	28 μ m Theoretical Prediction	119 μ m Theoretical Prediction	28 μ m Theoretical Prediction	119 μ m Theoretical Prediction	28 μ m Theoretical Prediction	119 μ m Theoretical Prediction
ε_o [%]	0.3	0.3	1.18	1.18	2.63	2.63
C_o [nF]	2.27	0.53	2.27	0.53	2.27	0.53
R [M Ω]	20.22	20.22	5.14	5.14	2.35	2.35
L [kH]	1272.51	1272.51	323.74	323.74	148.04	148.04
C [pF]	0.20	4.74	0.20	4.76	0.20	4.80
k^2 [%]	8.84E-03	8.84E-03	8.87E-03	8.87E-03	8.94E-03	8.94E-03
f_n [Hz]	31.4	64.8	62.1	128.2	91.5	188.9
Ψ [mN/V]	0.3	0.3	0.6	0.6	0.9	0.9
s [kN/m]	4.2	17.7	16.3	69.4	35.3	150.7
Q [unitless]	12.4	25.6	24.5	50.7	36.2	74.7
$R^*C_o^*\omega_h$	9.0	4.4	4.6	2.2	3.1	1.5
R_m [Ns/m]	1.7					

6.3 CD Jewel Case Device

A CD jewel case is approximately 12 mm x 125 mm x 150 mm. This is a very low profile device and will have a very limited tuning range due to the restriction in u_p . Figure 69 and Figure 70 show views of the iterated design. This device is similar to the matchbox device in function and electrical connections. However, the moving mass is tungsten and weighs 706 g and it has a much larger film area (69.5 mm x 125 mm). From the theory presented earlier, frequency was shown to be strongly dependant on mass. As such, the resulting frequency for this device, shown in Table 9, ranges from 3.7 to 15.3 Hz. The height restriction limits u_p to a range from 1.5 mm to 3 mm. This range produces static strains from 0.02% to 0.09% respectively.

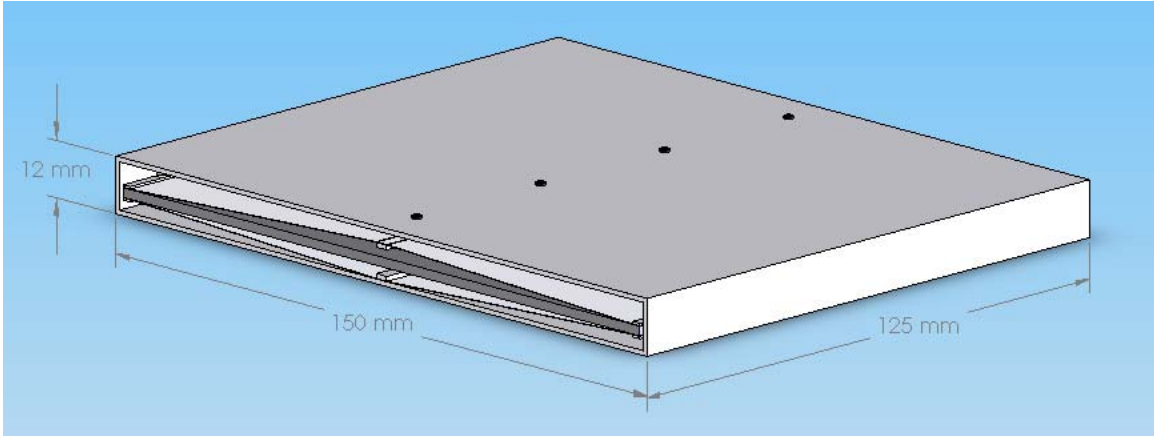


Figure 69 Model of the CD jewel case device.

The front view of the device (Figure 70) again shows the relationship of the components and the clearance along the wall of the enclosure. This space becomes more important in a large area device such as this as air needs to move between the upper and lower portions of the enclosure during the device vibrations.

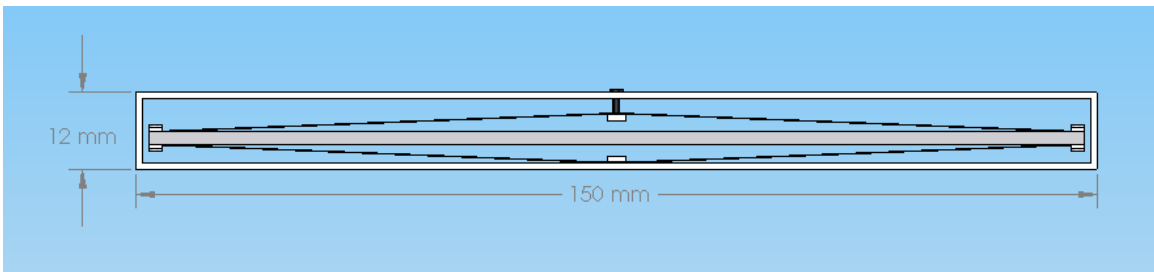


Figure 70 Front view of the CD jewel case device showing device configuration and clearance.

Predicted power outputs are shown in Figure 71 for configurations of the CD case device using both 28 μm and 119 μm PVDF films at various frequencies. The trends are as expected with the constant damping assumption; power output goes up from increases in both resonant frequency and acceleration. In practice, the damping term was seen to change with changes in device configuration.

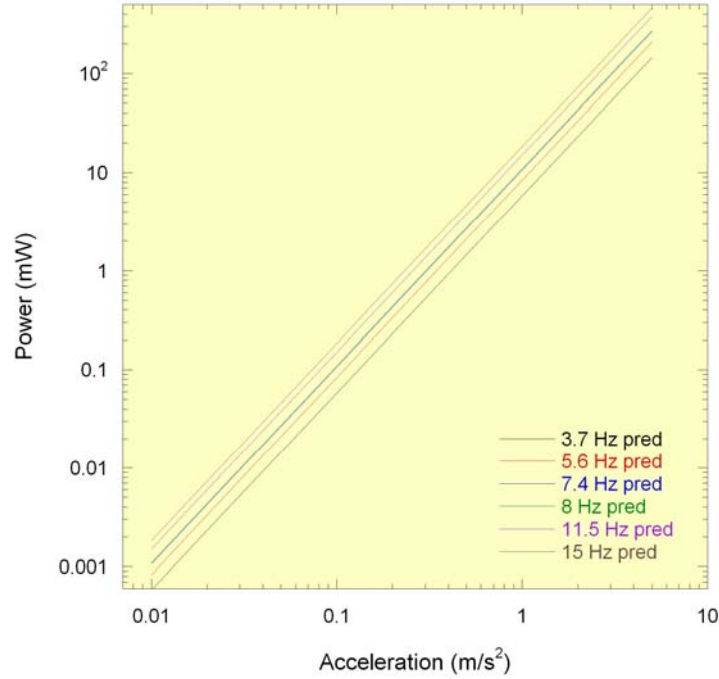


Figure 71 Predicted power vs. acceleration for the CD jewel case device showing performance from a device constructed with two sizes of PVDF film. Results of 3.7, 5.6 and 7.4 Hz are from 28 μm film, the remaining are from 119 μm film.

Table 9 Predicted results for the CD jewel case device at various u_p dimensions and film thicknesses. Calculations assume a constant R_m value of 1.7 Ns/m.

u_p [mm]	1.5		2.25		3	
	28 μm Theoretical Prediction	119 μm Theoretical Prediction	28 μm Theoretical Prediction	119 μm Theoretical Prediction	28 μm Theoretical Prediction	119 μm Theoretical Prediction
Parameter						
ε_o [%]	0.02	0.02	0.05	0.05	0.09	0.09
C_o [nF]	33.7	7.90	33.7	7.90	33.7	7.90
R [M Ω]	14.7	14.7	6.54	6.54	3.68	3.68
L [MH]	6.11	6.11	2.72	2.72	1.53	1.53
C [pF]	300	70.3	300	70.3	300	70.3
k^2 [%]	0.008823	0.008820	0.008825	0.008825	0.008827	0.008827
f_n [Hz]	3.7	7.7	5.6	11.5	7.4	15.3
Ψ [mN/V]	0.34	0.34	0.51	0.51	0.68	0.68
s [kN/m]	0.39	1.64	0.87	3.69	1.54	6.56
Q [unitless]	9.7	20.0	14.5	30.0	19.4	40.0
$R^*C_o*\omega_n$	11.6	5.6	7.7	3.7	5.8	2.8
R_m [Ns/m]	1.7					

The question of how well the PVDF material performs compared to PZT or other piezoceramic composites is addressed next. Minor modifications are required to the theoretical equations derived in Chapter 4 to accommodate a composite structure and are presented in detail in the appendix. The principle changes occur to the value for compliance and thickness of the film. The capacitance term is calculated using the thickness of the active layer while the mechanical terms for s and Ψ use the composite thickness. The CD jewel case device was chosen for comparison because of the very low strains necessary to operate the device.

The materials properties are from the materials specification sheet from Megacera, a division of Nihon Ceratec, Inc. a Japanese manufacturer. The “M” type product has 70 μm of PZT on a 70 μm brass substrate. Details of the type of PZT are not given however the following properties are listed:

- $d_{31} = -185 \text{E-}12 \text{ m/V}$
- $s_{11}^E = 15.2 \text{E-}12 \text{ m}^2/\text{N}$
- $\epsilon_{33} = 1.593 \text{E-}8 \text{ F/m}$

The results of the power prediction are shown in Figure 72 where the lowest frequency predictions from the two cases of PVDF are shown as a comparison. The PZT on brass foil produces almost twice the power of a 28 μm PVDF film device and about 50% more than the 119 μm PVDF film device. The difference can be attributed to the lack of strain that can be supported by the PZT material. The three conditions used very low strains and are listed in the table below with the other predicted values from this configuration. The limit on strain also affects the tuning range as tuning is a function of the change to the geometry. This configuration shows tuning of 4 Hz.

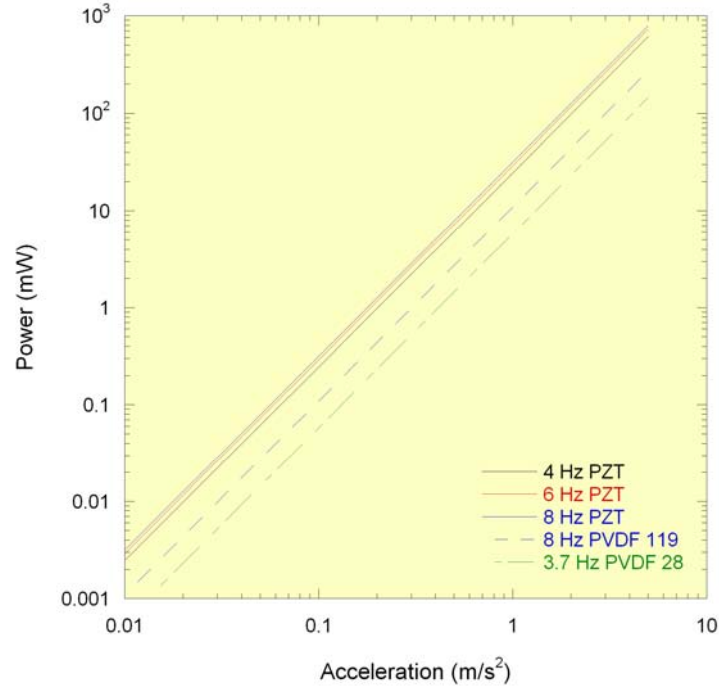


Figure 72 Predicted power vs. acceleration for the CD jewel case device showing performance from a device constructed with PZT on brass foils. Results of 3.7 Hz (PVDF 28 μm film) and 8 Hz (PVDF 119 μm film) are shown for comparison.

Table 10 Predicted results for the CD jewel case device at various u_p dimensions from films of PZT on brass. Calculations assume a constant R_m value of 1.7 Ns/m.

u_p [mm]	0.15	0.225	0.3
Parameter	140 μm Theoretical Prediction	140 μm Theoretical Prediction	140 μm Theoretical Prediction
ε_o [%]	0.00020	0.000500	0.000900
C_o [μF]	1.70	1.70	1.70
R [$\text{M}\Omega$]	0.039	0.018	0.010
L [kH]	16.370	7.276	4.093
C [nF]	0.931	0.931	0.931
k^2 [%]	0.052	0.052	0.052
f_n [Hz]	4.1	6.1	8.2
Ψ [mN/V]	6.567	9.851	13.134
s [N/m]	462.99	1041.72	1851.93
Q [unitless]	10.64	15.95	21.27
$R^*C_o^*\omega_n$	1.714	1.142	0.857
R_m [Ns/m]	1.7		

6.4 1/2 Pint Carton Device

A half pint milk carton is approximately 80 mm x 80 mm x 80 mm. The device designed around these dimensions utilizes the *xs*-model developed in Chapter 5 to predict performance. The predictions are based on using 28 μm and 119 μm PVDF films. The advantage that this package provides is the ability to really increase the mass in order to operate at a low frequency.

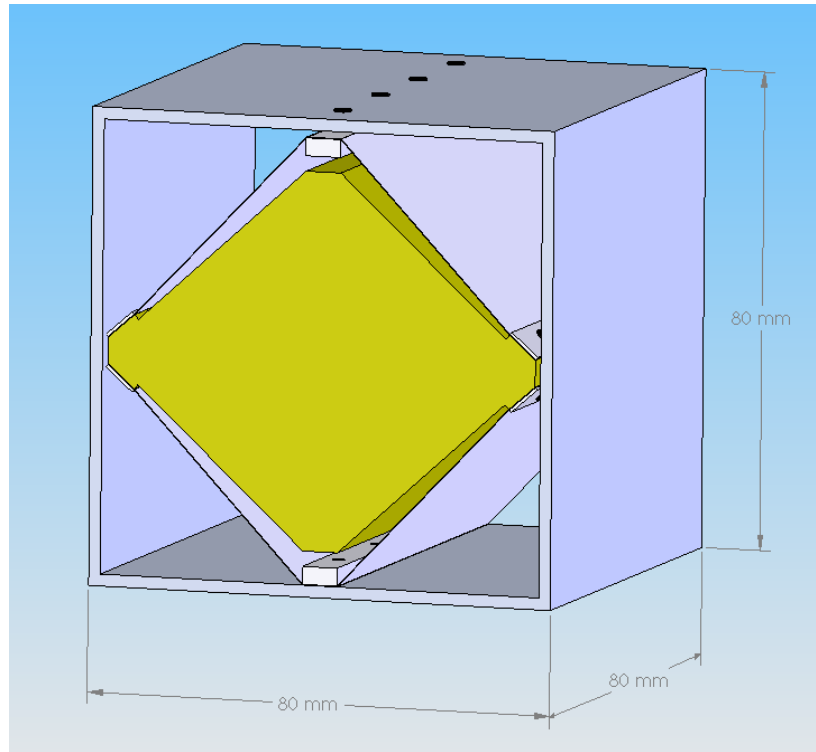


Figure 73 Model of the 1/2 pint carton device designed with a copper mass and PVDF films.

The device uses a copper mass of 1.87 kg shown in Figure 73. Figure 74 is the front view of the device and shows the relationship between the components as well as the limited adjustment range. The geometry of the *xs*-model really limits the tuning range of a device, as small changes in u_p effect large increases in the static strain of the active elements. Consequently, there is not a great need for a large tuning range.

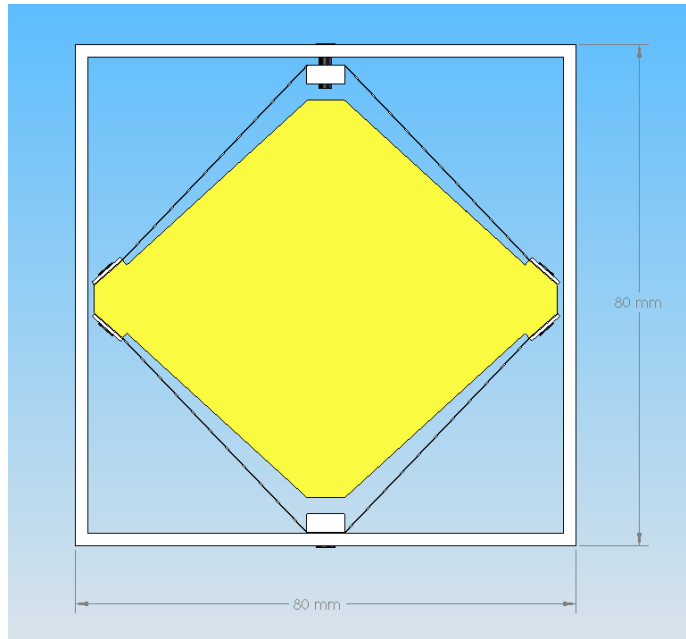


Figure 74 Front view of the 1/2 pint carton device showing relationship between components.

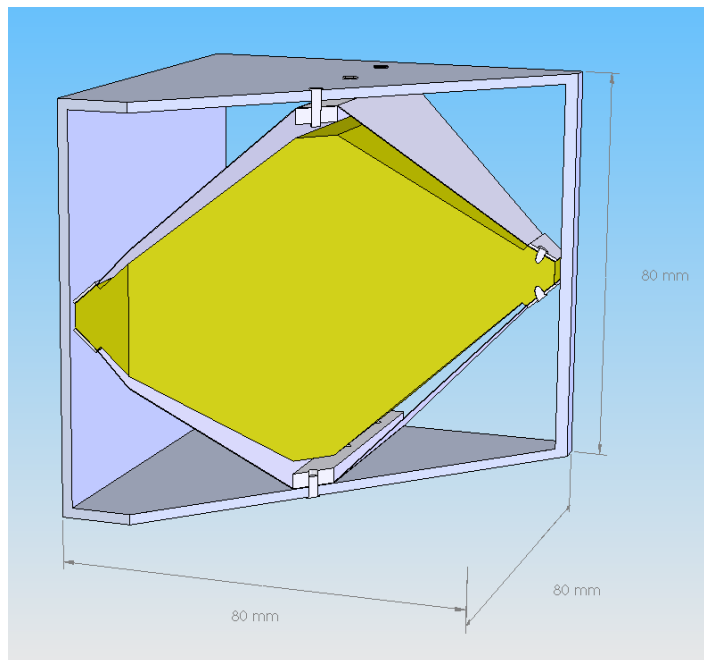


Figure 75 Section view of the 1/2 pint carton device showing additional relations between components.

Figure 75 provides an additional view to understand the relationship between the components of the device. The profile of the mass in the above figures shows an area where material is removed to provide clearance during the dynamic phase of operation and to minimize air damping.

Table 11 shows the predicted values of the device using the xs -model equations developed in Chapter 5. The frequency values indicate a very small tuning range, particularly with the 28 μm film. The large u_p value generates an excessive amount of strain, more than 5%. Of particular note is how high the resonant frequency is for any of the settings. However, inspection of the device stiffness term, s , quickly explains this result. The resonant frequency is shown to be a function of both the mass and the stiffness, and in the case of this configuration which allows a tremendous mass, the geometry also increases the stiffness significantly. Stiffness comparison to the CD jewel case device shows an increase of more than 700X. The mass increase on the other hand was only 2.5X.

Table 11 Predicted results for the 1/2 pint carton device at various u_p dimensions and film thicknesses. Calculations assume a constant R_m value of 6.5 Ns/m.

u_p [mm]	0.03		2.28		3.28	
	Theoretical Prediction					
ϵ_o [%]	0.05	0.05	3.94	3.94	5.71	5.71
C_o [nF]	0.13	2.98	0.13	2.98	0.13	2.98
R [M Ω]	0.13	0.13	0.12	0.12	0.12	0.12
L [kH]	38.36	38.36	35.54	34.47	34.47	34.47
C [pF]	0.017	0.399	0.018	0.418	0.018	0.418
k^2 [%]	0.013	0.013	0.014	0.014	0.014	0.014
f_n [Hz]	62.42	128.68	63.72	132.55	64.30	132.55
Ψ [mN/V]	6.987	6.987	7.260	7.371	7.371	7.371
s [kN/m]	288.11	1224.48	300.22	1299.19	305.69	1299.19
Q [unitless]	113.02	232.99	115.37	239.99	116.41	239.99
$R^*C_o^*\omega_n$	0.66	0.32	0.63	0.30	0.61	0.30
R_m [Ns/m]	6.5					

In this configuration, the heavy mass is supported by a large amount of film. The question of whether the films can support this mass is addressed as follows. In the d_{31} test conducted in Chapter 2, a small sample of film (13 mm x 28 μm) was subjected to a mass of ~100 g. The cross sectional area of the sample is 3.64E-7 m² and results in a stress of 275 kPa, safely below the reported yield strength

of 45 MPa for linearly stretched PVDF films such as these (Measurement Specialties, Inc.). The samples were not noticeably affected by this stress level. Consider the configuration above and assume that only the upper films support the mass. The film is 80 mm wide and in the worst case, 28 μm thick. The cross sectional area of a single film is $2.24\text{E-}6 \text{ m}^2$. With two films supporting the 1.87 kg mass, the stress is found to be 417 kPa. This result is still substantially below the reported yield strength of the material. However, the dynamic motion of the mass will limit the operational range of the device.

Power calculations shown in Figure 76 assume a constant mechanical damping term of $R_m=6.5 \text{ Ns/m}$ which is a midrange value derived from the *xs*-model experimental data. It is observed that a large amount of power can be generated with very small acceleration amplitudes, for example the 119 μm film produces almost 10 mW at 1 m/s^2 . The geometry appears to create a much larger gap between power generation as a function of film thickness. In this case, the power gap is about 2 orders of magnitude while the CD case and matchbox designs vary by less than half an order of magnitude. Additionally, the higher frequency curves (129, 131, and 133 Hz), generated by the 119 μm film are so close to one another as to be almost indistinguishable in the plot. The lower frequency bands also have a minimal separation.

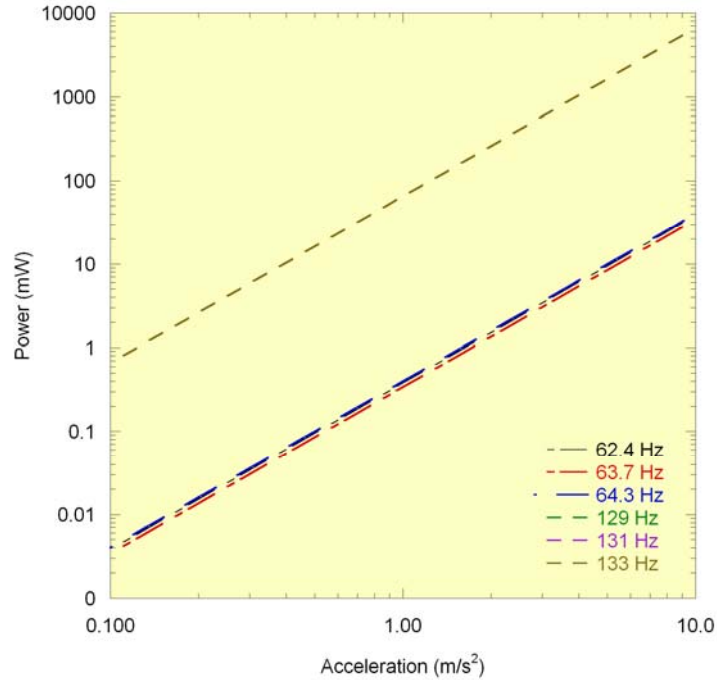


Figure 76 Predicted power vs. acceleration for the 1/2 pint carton device showing performance from a device constructed with two sizes of PVDF film. Results of 62.4, 63.7 and 64.3 Hz are from 28 μm film, the remaining are from 119 μm film.

6.5 Conclusions

This chapter presented a few configurations designed using a fixed volume constraint. The performance of the designs was estimated using the models created in the previous chapters. As stated at the beginning, any of the constraints may be used to guide the design including frequency range, acceleration magnitude, target power, and mass. Additionally, other piezoelectric materials can be used in place of PVDF by substituting the appropriate materials parameters as shown with the CD case device where the PVDF films are replaced with PZT on brass. Details to the equation variations are shown in the appendices for the composite materials model.

Predicted power and performance of the different devices showed additional relationships that must be considered when targeting particular design goals. For example, resonant frequency is often assumed to be largely a function of mass, however it was shown in the half pint device that the successful design must also control the stiffness term. Stiffness is shown to be very dependent on the

geometry. A comparison of the predicted performance of the devices in this chapter showed the increase in s with the changes in geometry of the different configurations. This relationship is also confirmed in Chapter 5, Figure 58 which shows the change in device stiffness with the addition of film length u_{xs} .

CHAPTER SEVEN

7 CONCLUSIONS

This document has presented the need, and one of a number of possible solutions, to the problem of powering remote devices directly or charging the power storage component of a remote sensing system. While vibrations may not be the most abundant of harvestable environmental energy, they certainly have their niche. Extensive research has been conducted on fixed frequency vibration devices, principally of the cantilever design, that convert the environmental mechanical energy into electrical energy through electromagnetic and piezoelectric effects. Because of the nature of resonant frequency oscillators such as cantilevers, which operate most effectively when the vibration of the device matches the input vibration, considerable design effort must be expended at the front end of an installation to insure the final design will operate effectively in the intended installation. Researchers have recognized the limitation of fixed frequency devices and efforts have been expended to move towards tunable devices.

The XMR device generates energy by stretching a piezoelectric film, and provides a means to vary the resonant tuning over a wide range through changes in device geometry. Results have shown a very broad and linear tuning range. A number of prototype devices were constructed with tuning ranges and details outlined in the Table 12. The initial XMR device shows a tuning range of 86 Hz-225 Hz. In contrast, tuning ranges in the literature report much lower values. Leland and Wright demonstrated tuning from 250 Hz to 200 Hz [19], while Challa *et al.* showed a device with a resonant frequency of 26 Hz that can tune between 24 Hz and 32 Hz [20]. This requires switching the polarity of the magnets. The RXMR device has a similar broad adjustment range of 54 Hz-182 Hz. Thicker films reduces the range from 110 Hz-180 Hz due to the increase in stiffness. Initial modeling demonstrated a linear power versus acceleration range that was a function of the geometric value u_p . As the ratio u_p/L_o increased, the linear power region with respect to acceleration increased.

Table 12 Device performance for various prototype configurations.

Device	Mass (g)	Film (μm)	Max Power Measured (mW)	Frequency Range Tested (Hz)	Working Volume (cm^3)	Acceleration Range Tested (m/s^2)	Power/Volume (mW/cm^3)
XMR	28.6	28	na	100-225	10	na	
XMR	28.6	28	$\sim 0.17^1$	86-154	10	2-10	0.017 ¹
RXMR	65	28	3.2	54-182	21	3-30	0.15
RXMR	82	9	0.3	39-60	21	0.5-4	0.01
RXMR	82	28	12	62-100	21	1-12	0.57
RXMR	82	119	22	110-180	21	0.9-25	1.05
RXMR-xs	82	119	40	332-378	78	0.2-79	0.51

¹ Single film operation

Power output for the different configurations is also shown in Table 12. The lowest power output is from the initial prototype device XMR at ~ 0.17 mW. The device performance is limited because of the small area of film and the strain gradients due to the geometry. The RXMR device with 119 μm films made 22 mW and exceeds the 1 mW/cm^3 mark initially requested by the Navy. The power/volume metric allows comparison to other devices in the literature. For example, Perpetuum sells an fixed frequency commercial harvester using an electromagnetic cantilever design that produces 4 mW at 100 Hz and 0.04 g acceleration in a 30 cm^3 package [60]. This equates to 0.13 mW/cm^3 . Calculation of an acceleration normalized value results in $3.3 \text{ mW/cm}^3\text{g}$. The RXMR is $0.42 \text{ mW/cm}^3\text{g}$. The power output generated by the device was shown to be more strongly affected by the damping of the device rather than the resonant frequency of operation, which was shown to be contrary to cantilever devices.

The RXMR (rectangular model) provides additional power output over the original circular model XMR. This is primarily due to the elimination of strain gradients in the film elements of the RXMR design. The reduction in the strain gradient allows all the active area of the films to produce power effectively. Improvements in power are seen by comparing the power/volume metric. Assuming the single film output would double to 0.034 mW for the XMR device operating with both films, the

RXMR produces more than 4 times the power per volume. The reduction in the strain gradient also prevents premature failure of the films due to plastic deformation.

Modeling developed the relationships for power output based on materials properties and device geometry. Prototype devices were constructed and evaluated. Results compared favorably to the model predictions at low acceleration magnitudes. The predictive capabilities for other parameters such as device stiffness, resonant frequency, coupling, capacitance, optimal load resistance and device quality factor compare favorably as well. The model can be used as a design tool to optimize a harvester that can operate through a variety of conditions. Any of the parameters may be used as design constraints to generate an iterative solution.

Equations were also developed to allow the use of composite material films such as PZT on brass. The assumption is based on constant strain, i.e. the interface between the composite is ideal. The ability to use composite films affects a limited number of equations in the model, principally the capacitance, C_0 , stiffness, s , and electromechanical coupling term, Ψ .

The modeling was expanded to include additional film lengths, L_{xs} , to accommodate geometries that may include piezoceramic structures that are not capable of significant strains but need to operate in a particular vibration spectrum. At present, the equations of the xs -model tend to over predict the device stiffness and coupling. Many of the other parameters are determined from these two, so the error propagates through. However, the power predictions from the model match closely to the values measured from a prototype device. This may be attributed to the strong dependence in the power equation on the damping term (which must be measured) and the weak dependence on the parameters determined from device geometry. The RXMR with excess film shows a reduced tuning range at a much higher resonant frequency for similar strain ranges, i.e. 332 Hz to 378 Hz. The power is somewhat lower than the RXMR regular model for similar strains and accelerations as seen in Figure 64 however the design provides harvesting at accelerations in excess of 75 m/s^2 .

As a design exercise and to show the performance range of the RXMR device a number of volume limited designs were modeled and evaluated. Frequencies ranged between 3 Hz to 190 Hz and predicted powers up to 650 mW at 3 m/s^2 acceleration. Comparisons are shown for variables such as film thickness (28 μm and 119 μm) and strains (0.02% to 5.71%) through variation of the pretension dimension u_p . In one case, PVDF films are compared with a PZT on brass composite with the composite PZT structure producing about 120 mW at 3 m/s^2 versus 2.5 mW for the PVDF at the same acceleration. This was accomplished at very low static strain rates of less than 0.0009%. Device geometry is shown to influence the stiffness of the mechanism which dramatically affects the resonant frequency. This is particularly evident in the half pint carton device where the mass is very large, 1.8 kgs, however the device geometry drives the stiffness so high that the resonant frequency range was much higher than anticipated.

There are still many unanswered questions. The performance of PVDF films are known to be affected by temperature, both high and low. This fact was observed in some experiments conducted in this research, however the issue has not been addressed in the modeling. PVDF has a very low piezoelectric coefficient which is why some of the work conducted was on composite PVDF/HFP-PZT films. There are still many issues to resolve in this system; casting a consistent film, phase conversion, poling, applying electrodes. The significant difference between some terms in the *xs*-model still must be addressed. There is the issue of saturation that is observed in the power output at higher accelerations and while work has been progressing on this, the solution is not yet at hand.

Other issues would be interesting to pursue, for example, the composite film model could be expanded to incorporate a bimorph configuration. The single element PVDF films could be doubled or tripled up, with electrodes in common. Both of these methods would certainly increase the device stiffness but may also improve power output. Prototype devices could be constructed of PZT on brass and compared to the predicted results. Additional testing of the *xs*-model prototype device should be conducted and used to help clarify the model.

This research has provided a design tool that can predict device performance based on geometry and materials properties. It allows direction in optimizing the power output for a vibration harvesting device. It has also shown relationships between device parameters and performance.

REFERENCES

- [1] Beeby, S.P., Torah, R.N., Tudor, M.J., Glynne-Jones, P., Donnell, T.O., Saha, C.R., and Roy, S., *A micro electromagnetic generator for vibration energy harvesting*. Journal of Micromechanics and Microengineering, 2007(7): p. 1257.
- [2] El-hami, M., Glynne-Jones, P., White, N.M., Hill, M., Beeby, S., James, E., Brown, A.D., and Ross, J.N., *Design and fabrication of a new vibration-based electromechanical power generator*. Sensors and Actuators A: Physical, 2001. **92**(1-3): p. 335.
- [3] Amirtharajah, R. and Chandrakasan, A.P., *Self-powered signal processing using vibration-based power generation*. IEEE Journal of Solid-State Circuits, 1998. **33**(5): p. 687.
- [4] Williams, C.B., Shearwood, C., Harradine, M.A., Mellor, P.H., Birch, T.S., and Yates, R.B., *Development of an electromagnetic micro-generator*. Circuits, Devices and Systems, IEE Proceedings -, 2001. **148**(6): p. 337.
- [5] Ching, N.N.H., Li, W.J., Leong, P.H.W., Wen, Z., and Wong, H.Y. *A laser-micromachined multi-modal resonating power transducer for wireless sensing systems*. 2002. Munich: Elsevier Science B.V.
- [6] Roundy, S., Leland, E.S., Baker, J., Carleton, E., Reilly, E., Lai, E., Otis, B., Rabaey, J.M., Wright, P.K., and Sundararajan, V., *Improving power output for vibration-based energy scavengers*. IEEE Pervasive Computing, 2005. **4**(1): p. 28.
- [7] Renaud, M., Fiorini, P., and van Hoof, C., *Optimization of a piezoelectric unimorph for shock and impact energy harvesting*. Smart Materials and Structures, 2007(4): p. 1125.
- [8] Stephen, N.G., *On energy harvesting from ambient vibration*. Journal of Sound and Vibration, 2006. **293**(1-2): p. 409.
- [9] Beeby, S.P., Tudor, M.J., and White, N.M., *Energy harvesting vibration sources for microsystems applications*. Measurement Science and Technology, 2006. **17**(12): p. 175-195.
- [10] Nakano, K., Elliott, S.J., and Rustighi, E., *A unified approach to optimal conditions of power harvesting using electromagnetic and piezoelectric transducers*. Smart Materials and Structures, 2007. **16**(4): p. 948.
- [11] Roundy, S., *On the effectiveness of vibration-based energy harvesting*. Journal of Intelligent Material Systems and Structures, 2005. **16**(10): p. 809.
- [12] Rossi, G., Marsili, R., Gusella, V., and Gioffre, M., *Comparison between accelerometer and laser vibrometer to measure traffic excited vibrations on bridges*. Shock and Vibration, 2002. **9**(1-2): p. 11.
- [13] Lin, C.W. and Yang, Y.B., *Use of a passing vehicle to scan the fundamental bridge frequencies: An experimental verification*. Engineering Structures, 2005. **27**(13): p. 1865.

- [14] Glanville, M.J., Kwok, K.C.S., and Denoon, R.O., *Full-scale damping measurements of structures in Australia*. Journal of Wind Engineering and Industrial Aerodynamics, 1996. **59**(2-3): p. 349.
- [15] Yoshimura, M., Wu, Q., Takahashi, K., Nakamura, S., and Furukawa, K., *Vibration analysis of the Second Saikai Bridge--a concrete filled tubular (CFT) arch bridge*. Journal of Sound and Vibration, 2006. **290**(1-2): p. 388.
- [16] Ottman, G.K., Hofmann, H.F., Bhatt, A.C., and Lesieutre, G.A., *Adaptive piezoelectric energy harvesting circuit for wireless remote power supply*. IEEE Transactions on Power Electronics, 2002. **17**(5): p. 669.
- [17] Wu, W.J., Chen, Y.F., Chen, Y.Y., Wang, C.S., and Chen, Y.H. *Smart wireless sensor network powered by random ambient vibrations*. 2007. Taipei, Taiwan: Institute of Electrical and Electronics Engineers Inc., New York, NY 10016-5997, United States.
- [18] Roundy, S. and Zhang, Y. *Toward self-tuning adaptive vibration based micro-generators*. 2005. Sydney, Australia: International Society for Optical Engineering, Bellingham, WA 98227-0010, United States.
- [19] Leland, E.S. and Wright, P.K., *Resonance tuning of piezoelectric vibration energy scavenging generators using compressive axial preload*. Smart Materials and Structures, 2006(5): p. 1413.
- [20] Challa, V.R., Prasad, M.G., Shi, Y., and Fisher, F.T., *A vibration energy harvesting device with bidirectional resonance frequency tunability*. Smart Materials and Structures, 2008(1).
- [21] Rastegar, J., Pereira, C., and Nguyen, H.L. *Piezoelectric-based power sources for harvesting energy from platforms with low frequency vibration*. 2006. San Diego, CA, United States: International Society for Optical Engineering, Bellingham WA, WA 98227-0010, United States.
- [22] Shahruz, S.M., *Design of mechanical band-pass filters with large frequency bands for energy scavenging*. Mechatronics, 2006. **16**(9): p. 523.
- [23] Tieck, R.M., Carman, G.P., and Enoch Lee, D.G. *Electrical energy harvesting using a mechanical rectification approach*. 2006. Chicago, IL, United States: American Society of Mechanical Engineers, New York, NY 10016-5990, United States.
- [24] Morris, D.J., Youngsman, J.M., Anderson, M.J., and Bahr, D.F., *A resonant-frequency tunable, extensional mode piezoelectric vibration harvesting mechanism*. Smart Materials and Structures, 2008. **17**.
- [25] Stachura, S., *NTSB investigators surprised by what they found*. 2008, Minnesota Public Radio: Minnesota Public Radio Website.
- [26] Clegg, W.W., Jenkins, D.F.L., and Cunningham, M.J., *The preparation of piezoceramic-polymer thick films and their application as micromechanical actuators*. Sensors and Actuators A: Physical, 1997. **58**(3): p. 173.
- [27] Seema, A., Dayas, K.R., and Varghese, J.M., *PVDF-PZT-5H composites prepared by hot press and tape casting techniques*. Journal of Applied Polymer Science, 2007. **106**(1): p. 146.

- [28] Naval Research Laboratories Materials Science and Technology Division, *Crystal Lattice Structures* <http://cst-www.nrl.navy.mil/lattice/index.html>.
- [29] Roundy, S., Wright, P.K., and Rabaey, J., *A study of low level vibrations as a power source for wireless sensor nodes*. Computer Communications, 2003. **26**(11): p. 1131.
- [30] Sodano, H.A., Lloyd, J., and Inman, D.J., *An experimental comparison between several active composite actuators for power generation*. Smart Materials and Structures, 2006. **15**(5): p. 1211.
- [31] Jeon, Y.B., Sood, R., Jeong, J.H., and Kim, S.G., *MEMS power generator with transverse mode thin film PZT*. Sensors and Actuators, A: Physical, 2005. **122**(1 SPEC ISS): p. 16.
- [32] Harrison, J.S. and Ounaies, Z., *Piezoelectric Polymers*. 2001: Hampton, VA. p. 32.
- [33] Linares, A. and Acosta, J.L., *Tensile and dynamic mechanical behaviour of polymer blends based on PVDF*. European Polymer Journal, 1997. **33**(4): p. 467.
- [34] Lovinger, A.J., *Ferroelectric Polymers*. Science, 1983. **220**(4602): p. 1115-1121.
- [35] El-Hami, K., Ribbe, A., Isoda, S., and Matsushige, K., *Structural analysis of the P(VDF/TrFE) copolymer film*. Chemical Engineering Science, 2003. **58**(2): p. 397.
- [36] Chilton, J.A. and Goosey, M.T., eds. *Special Polymers for Electronics & Optoelectronics*. 1st ed. 1995, Chapman & Hall: London.
- [37] Gregorio, R.J., Cestari, M., and Bernardino, F.E., *Dielectric behaviour of thin films of β -PVDF/PZT and β -PVDF/BaTiO₃ composites*. Journal of Materials Science, 1996. **31**(11): p. 2925.
- [38] Gregorio, R.J. and Cestari, M., *Effect of crystallization temperature on the crystalline phase content and morphology of poly(vinylidene fluoride)*. Journal of Polymer Science, Part B: Polymer Physics, 1994. **32**(5): p. 859.
- [39] Kepler, R.G., *Piezoelectricity, Pyroelectricity, and Ferroelectricity in Organic Materials*. Annual Review of Physical Chemistry, 1978. **29**(1): p. 497-518.
- [40] Thomson, W.T., *Theory of vibrations with applications*. 2nd ed. 1981, Englewood Cliffs, N.J.: Prentice-Hall, Inc. 493.
- [41] Liu, C., *Foundations of MEMS*. 2006, Upper Saddle River, NJ: Pearson Education, Inc. 530.
- [42] Williams, C.B. and Yates, R.B., *Analysis of a micro-electric generator for microsystems*. Sensors and Actuators, A: Physical, 1996. **52**(1-3 pt 1): p. 8.
- [43] Zeng, R., Kwok, K.W., Chan, H.L.W., and Choy, C.L., *Longitudinal and transverse piezoelectric coefficients of lead zirconate titanate/vinylidene fluoride-trifluoroethylene composites with different polarization states*. Journal of Applied Physics, 2002. **92**(5): p. 2674.
- [44] Socrates, G., *Infrared characteristic group frequencies*. 1980, Chichester: John Wiley & Sons, Ltd. 153.

- [45] Lanceros-Mendez, S., Mano, J.F., Costa, A.M., and Schmidt, V.H., *FTIR and DSC studies of mechanically deformed β -PVDF films*. Journal of Macromolecular Science - Physics, 2001. **40** B(3-4): p. 517.
- [46] Goodfellow Corporation, *Polyvinylidene fluoride (PVDF) Material Information*. 2008.
- [47] Sullivan, M.S., *Development of a novel method for measuring the transverse piezoelectric coefficients of thin piezoelectric films*, in *Materials Science and Engineering*. 2004, Washington State University: Pullman. p. 90.
- [48] Robinson, M.C., *Microstructural and geometric effects on the piezoelectric performance of PZT MEMS*, in *Materials Science*. 2007, Washington State University: Pullman. p. 196.
- [49] Anton, S.R. and Sodano, H.A., *A review of power harvesting using piezoelectric materials (2003-2006)*. Smart Materials and Structures, 2007(3): p. R1.
- [50] Casciati, F. and Rossi, R., *A power harvester for wireless sensing applications*. Structural Control & Health Monitoring, 2007. **14**(4): p. 649-659.
- [51] Mossi, K., Green, C., Ounaies, Z., and Hughes, E., *Harvesting energy using a thin unimorph prestressed bender: Geometrical effects*. Journal of Intelligent Material Systems and Structures, 2005. **16**(3): p. 249.
- [52] Kim, H.W., Priya, S., Uchino, K., and Newnham, R.E., *Piezoelectric energy harvesting under high pre-stressed cyclic vibrations*. Journal of Electroceramics, 2005. **15**(1): p. 27.
- [53] Cho, J.H., Richards, R.F., Bahr, D.F., Richards, C.D., and Anderson, M.J., *Efficiency of energy conversion by piezoelectrics*. Applied Physics Letters, 2006. **89**(10): p. 104107.
- [54] Hu, Y., Xue, H., and Hu, H., *A piezoelectric power harvester with adjustable frequency through axial preloads*. Smart Materials and Structures, 2007. **16**(5): p. 1961.
- [55] Mitcheson, P.D., Reilly, E.K., Toh, T., Wright, P.K., and Yeatman, E.M., *Performance limits of the three MEMS inertial energy generator transduction types*. Journal of Micromechanics and Microengineering, 2007(9): p. S211.
- [56] Kino, G., *Acoustic waves: devices, imaging, and analog signal processing*. 1987, Englewood Cliffs, NJ: Prentice-Hall, Inc. 601.
- [57] DuToit, N.E. and Wardle, B.L., *Experimental verification of models for microfabricated piezoelectric vibration energy harvesters*. AIAA Journal, 2007. **45**(5): p. 1126.
- [58] Renno, J.M., Daqaq, M.F., and Inman, D.J., *On the optimal energy harvesting from a vibration source*. Journal of Sound and Vibration, 2009. **320**(1-2): p. 386.
- [59] Heffernan, R., Precetti, D., and Johnson, W., *Vibration Analysis of SA349/2 Helicopter*, NASA, Editor. 1991, Publ by NASA: New York, NY, USA. p. 104.
- [60] PMG Perpetuum Ltd. <http://www.perpetuum.co.uk/>.

APPENDIX

A1 Materials Properties Information

A1.1 Materials properties of Measurement Specialties, Inc. PVDF

Table 1. Typical properties of piezo film

Symbol	Parameter		PVDF	Copolymer	Units
t	Thickness		9, 28, 52, 110	<1 to 1200	μm (micron, 10^{-6})
d_{31}	Piezo Strain Constant		23	11	$10^{-12} \frac{\text{m/m}}{\text{V/m}}$ or $\frac{\text{C/m}^2}{\text{N/m}^2}$
d_{33}			-33	-38	
g_{31}	Piezo Stress constant		216	162	$10^{-3} \frac{\text{V/m}}{\text{N/m}^2}$ or $\frac{\text{m/m}}{\text{C/m}^2}$
g_{33}			-330	-542	
k_{31}	Electromechanical Coupling Factor		12%	20%	
k_t			14%	25-29%	
C	Capacitance		380 for 28 μm	68 for 100 μm	pF/cm ² @ 1KHz
Y	Young's Modulus		2-4	3-5	10^9 N/m^2
V_0	Speed of Sound	stretch: thickness:	1.5	2.3	10^3 m/s
			2.2	2.4	
p	Pyroelectric Coefficient		30	40	$10^{-6} \text{ C/m}^2 \text{ }^\circ\text{K}$
ϵ	Permittivity		106-113	65-75	10^{-12} F/m
ϵ/ϵ_0	Relative Permittivity		12-13	7-8	
ρ_m	Mass Density		1.78	1.82	10^3 kg/m
ρ_e	Volume Resistivity		$>10^{13}$	$>10^{14}$	Ohm meters
R_{\square}	Surface Metallization Resistivity		<3.0	<3.0	Ohms/square for NiAl
R_{\square}			0.1	0.1	Ohms/square for Ag Ink
$\tan \delta_e$	Loss Tangent		0.02	0.015	@ 1KHz
	Yield Strength		45-55	20-30	10^6 N/m^2 (stretch axis)
	Temperature Range		-40 to 80...100	-40 to 115...145	$^\circ\text{C}$
	Water Absorption		<0.02	<0.02	% H ₂ O
	Maximum Operating Voltage		750 (30)	750 (30)	V/mil(V/ μm), DC, @ 25 $^\circ\text{C}$
	Breakdown Voltage		2000 (80)	2000 (80)	V/mil(V/ μm), DC, @ 25 $^\circ\text{C}$

Table 2. Comparison of piezoelectric materials

Property	Units	PVDF Film	PZT	BaTiO ₃
Density	10 ³ kg/m ³	1.78	7.5	5.7
Relative Permittivity	ϵ/ϵ_0	12	1,200	1,700
d_{31} Constant	(10 ⁻¹²)C/N	23	110	78
g_{31} Constant	(10 ⁻³)Vm/N	216	10	5
k_{31} Constant	% at 1 KHz	12	30	21
Acoustic Impedance	(10 ⁶)kg/m ² -sec.	2.7	30	30

OPERATING PROPERTIES FOR A TYPICAL PIEZO FILM ELEMENT

The DT1 element is a standard piezo film configuration consisting of a 12x30 mm active area printed with silver ink electrodes on both surfaces of a 15x40 mm die-cut piezo polymer substrate.

1. Electro-Mechanical Conversion

(1 direction) 23 x 10⁻¹²m/V, 700 x 10⁻⁶N/V
 (3 direction) -33 x 10⁻¹²m/V

2. Mechano-Electrical Conversion

(1 direction) 12 x 10⁻³V per microstrain, 400 x 10⁻³V/ μ m, 14.4V/N
 (3 direction) 13 x 10⁻³V/N

3. Pyro-Electrical Conversion

8V/ $^{\circ}$ K (@ 25 $^{\circ}$ C)

4. Capacitance

1.36 x 10⁻⁹F; Dissipation Factor of 0.018 @ 10 KHz; Impedance of 12 K Ω @ 10 KHz

5. Maximum Operating Voltage

DC: 280 V (yields 7 μ m displacement in 1 direction)
 AC: 840 V (yields 21 μ m displacement in 1 direction)

6. Maximum Applied Force (at break, 1 direction)

6-9 kgF (yields voltage output of 830 to 1275 V)

A1.2 Materials properties for PZT on brass

標準材料特性

STANDARD MATERIAL CHARACTERISTICS

原 材 名 Material code		M	D	C	NA
比 誘 電 率 Dielectric constant	ϵ_{33}/ϵ_0	1800	4500	1550	1460
	ϵ_{11}/ϵ_0	1700	4700	1550	1750
誘電損失係数 Dielectric loss tangent	$\tan \delta$ (%)	2.0	2.0	0.4	0.4
電気機械結合係数 Coupling factor	K_r	0.61	0.70	0.61	0.58
	K_{31}	0.36	0.41	0.35	0.33
	K_{33}	0.74	0.76	0.65	0.69
	K_t	0.48	0.45	0.52	0.55
	K_{15}	0.72	0.72	0.65	0.73
圧電定数 Piezo-electric strain constant	d_{31} ($\times 10^{-12}\text{m/V}$)	-185	-360	-160	-120
	d_{33} ($\times 10^{-12}\text{m/V}$)	420	660	280	315
	d_{15} ($\times 10^{-12}\text{m/V}$)	630	1010	450	580
圧電出力定数 Voltage output constant	g_{31} ($\times 10^{-3}\text{V}\cdot\text{m/N}$)	-10.3	-8.75	-11.5	-10.8
	g_{33} ($\times 10^{-3}\text{V}\cdot\text{m/N}$)	23.3	16.3	16.5	25.0
	g_{15} ($\times 10^{-3}\text{V}\cdot\text{m/N}$)	36.9	24.3	30.5	37.5
弾性定数 Elastic constant	S_{11} ($\times 10^{-12}\text{m}^2/\text{N}$)	15.2	14.9	15.2	12.1
	S_{33} ($\times 10^{-12}\text{m}^2/\text{N}$)	17.7	18.5	15.5	16.6
ヤング率 Young's modulus	Y_{11} ($\times 10^{10}\text{N/m}^2$)	6.5	6.7	6.6	8.2
	Y_{33} ($\times 10^{10}\text{N/m}^2$)	5.6	5.4	6.5	6.5
機械的品質係数 Mechanical quality factor	Q_m	60	60	1350	2000
キュリー温度 Curie temperature	T_c ($^{\circ}\text{C}$)	320	180	310	310
密度 Density	ρ ($\times 10^3\text{kg/m}^3$)	7.7	7.8	7.5	7.6
周波数定数 Frequency constant	N_r ($\text{Hz}\cdot\text{m}$)	2030	1910	2080	2250
	N_{31} ($\text{Hz}\cdot\text{m}$)	1460	1460	1515	1650
	N_{33} ($\text{Hz}\cdot\text{m}$)	1350	1310	2024	1540
	N_t ($\text{Hz}\cdot\text{m}$)	2050	2100	2070	1850
	N_{15} ($\text{Hz}\cdot\text{m}$)	900	860	940	960

仕様は改良などのために、予告なしに変更することがあります。

The specifications contained in this brochure may be changed without previous notice owing to our further improvement.

Megacera 株式会社 日本セラテックメガセラ事業本部
Nihon Ceratec Co., Ltd. Megacera Div

埼玉工場 埼玉県日高市大字原宿7番地5
〒350-1205 TEL (042) 985-1111 (代)
FAX (042) 989-7378
e-mail: sales@megacera.com

Saitama Office・Factory: 7-5 Harajuku, Hidaka-City,
Saitama 350-1205, Japan
(PHONE) +81-42-985-1111
(FAX) +81-42-989-7378
e-mail: sales@megacera.com

圧電サウンダー・スピーカ用エレメント (他励型)

PIEZOCERAMIC SOUNDER · SPEAKER ELEMENTS
(External drive)

製品コード Model code	共振周波数 Resonant frequency [KHz]	共振抵抗 Resonant resistance [Ω] max	静電容量 Electrostatic capacity [PF] ±30%	寸 法 Dimensions [mm]				振動板材質 Material of metal plate
				振動板 Diameter of metal plate (D)	圧電板 Diameter of ceramic element (d)	総厚み Total thickness of vibration plate (T)	金属板厚 Thickness of metal plate (t)	
M12SA1	5.6±1.0	600	14000	12.0±0.1	9.0±0.3	0.13±0.03	0.07±0.02	Brass
M122A2	9.5±1.0	400	7000	12.0±0.1	9.0±0.3	0.21±0.05	0.10±0.02	Brass
D131A1	4.2±0.5	300	36000	13.0±0.1	9.0±0.3	0.11±0.03	0.05±0.01	Brass
D201B1A	2.0±0.5	300	90000	20.0±0.1	15.0±0.3	0.11±0.03	0.05±0.01	42 alloy
M202B2	3.7±0.5	300	24000	20.0±0.1	15.0±0.3	0.21±0.05	0.10±0.02	Brass
M204B4	6.5±1.0	300	12000	20.0±0.1	15.0±0.3	0.41±0.07	0.20±0.02	Brass
M204B4A	7.0±1.0	300	12000	20.0±0.1	15.0±0.3	0.41±0.05	0.20±0.02	42 alloy
M253B4A	4.0±1.0	300	12000	25.0±0.1	15.0±0.3	0.36±0.06	0.15±0.02	42 alloy
M272C2	2.3±0.5	300	44000	27.0±0.1	20.0±0.3	0.21±0.05	0.10±0.02	Brass
M274C4	3.5±0.5	250	22000	27.0±0.1	20.0±0.3	0.41±0.07	0.20±0.02	Brass
M312C2A	1.4±0.5	600	44000	31.2±0.1	20.0±0.3	0.21±0.05	0.10±0.02	42 alloy
M352D2A	1.2±0.5	600	70000	35.0±0.1	25.0±0.4	0.21±0.05	0.10±0.02	42 alloy
M354D4	2.2±0.5	300	35000	35.0±0.1	25.0±0.4	0.41±0.07	0.20±0.02	Brass
M412D2	1.0±0.3	1000	70000	41.0±0.1	25.0±0.4	0.21±0.05	0.10±0.02	Brass
M412D2A	0.8±0.3	1000	70000	41.0±0.1	25.0±0.4	0.21±0.05	0.10±0.02	42 alloy
M442D2	0.6±0.3	1000	70000	44.0±0.1	25.0±0.4	0.21±0.05	0.10±0.02	Brass
M504E4	1.0±0.3	800	50000	50.0±0.1	30.0±0.4	0.41±0.07	0.20±0.02	Brass

Model code M12SA1 was selected as the representative PZT on brass sample for calculations.

A2 RXMR Excess Model Development Equations from *Mathematica*

A2.1 RXMR Tlr App cos a total strain xs.nb

RXMR Tlr App cos a total strain xs.nb

1

Calculations for xs total strain cos α

Start with top film such that up+uxs is the position from the centered mass. When the mass is displaced upward (in this case) Δu is subtracted from the height.

In[74]:= Clear[up, uxs, L0, Δu]

$$\frac{\text{up} + \text{uxs} - \Delta u}{\sqrt{L0^2 + (\text{up} + \text{uxs} - \Delta u)^2}} * \frac{\sqrt{L0^2 + (\text{up} + \text{uxs} - \Delta u)^2} - \sqrt{L0^2 + \text{uxs}^2}}{\sqrt{L0^2 + \text{uxs}^2}};$$

Series[%, {Δu, 0, 2}]

$$\begin{aligned} \text{Out[76]} = & \frac{(\text{up} + \text{uxs}) \left(-\sqrt{L0^2 + \text{uxs}^2} + \sqrt{L0^2 + \text{up}^2 + 2 \text{up} \text{uxs} + \text{uxs}^2} \right)}{\sqrt{L0^2 + \text{uxs}^2} \sqrt{L0^2 + \text{up}^2 + 2 \text{up} \text{uxs} + \text{uxs}^2}} + \\ & \frac{1}{\sqrt{L0^2 + \text{uxs}^2}} \left(\left(-\frac{\sqrt{L0^2 + \text{uxs}^2} + \sqrt{L0^2 + \text{up}^2 + 2 \text{up} \text{uxs} + \text{uxs}^2}}{\sqrt{L0^2 + \text{up}^2 + 2 \text{up} \text{uxs} + \text{uxs}^2}} + \right. \right. \\ & (\text{up} + \text{uxs}) \left(\frac{\text{up}}{\sqrt{L0^2 + \text{up}^2 + 2 \text{up} \text{uxs} + \text{uxs}^2}} - \frac{\text{uxs}}{\sqrt{L0^2 + \text{up}^2 + 2 \text{up} \text{uxs} + \text{uxs}^2}} + \left(\frac{\text{up}}{(L0^2 + \text{up}^2 + 2 \text{up} \text{uxs} + \text{uxs}^2)^{3/2}} + \right. \right. \\ & \left. \left. \frac{\text{uxs}}{(L0^2 + \text{up}^2 + 2 \text{up} \text{uxs} + \text{uxs}^2)^{3/2}} \right) \left(-\sqrt{L0^2 + \text{uxs}^2} + \sqrt{L0^2 + \text{up}^2 + 2 \text{up} \text{uxs} + \text{uxs}^2} \right) \right) \Delta u \Big) + \\ & \frac{1}{\sqrt{L0^2 + \text{uxs}^2}} \left(\left(-\frac{\text{up}}{\sqrt{L0^2 + \text{up}^2 + 2 \text{up} \text{uxs} + \text{uxs}^2}} - \frac{\text{uxs}}{\sqrt{L0^2 + \text{up}^2 + 2 \text{up} \text{uxs} + \text{uxs}^2}} - \right. \right. \\ & \left. \left(\frac{\text{up}}{(L0^2 + \text{up}^2 + 2 \text{up} \text{uxs} + \text{uxs}^2)^{3/2}} + \frac{\text{uxs}}{(L0^2 + \text{up}^2 + 2 \text{up} \text{uxs} + \text{uxs}^2)^{3/2}} \right) \right. \\ & \left. \left(-\sqrt{L0^2 + \text{uxs}^2} + \sqrt{L0^2 + \text{up}^2 + 2 \text{up} \text{uxs} + \text{uxs}^2} \right) + \right. \\ & (\text{up} + \text{uxs}) \left(\left(-\frac{\text{up}^2}{2 (L0^2 + \text{up}^2 + 2 \text{up} \text{uxs} + \text{uxs}^2)^{3/2}} - \right. \right. \\ & \left. \frac{\text{up} \text{uxs}}{(L0^2 + \text{up}^2 + 2 \text{up} \text{uxs} + \text{uxs}^2)^{3/2}} - \frac{\text{uxs}^2}{2 (L0^2 + \text{up}^2 + 2 \text{up} \text{uxs} + \text{uxs}^2)^{3/2}} + \right. \\ & \left. \left. \frac{1}{2 \sqrt{L0^2 + \text{up}^2 + 2 \text{up} \text{uxs} + \text{uxs}^2}} \right) / \left(\sqrt{L0^2 + \text{up}^2 + 2 \text{up} \text{uxs} + \text{uxs}^2} \right) + \right. \\ & \left(\frac{\text{up}}{(L0^2 + \text{up}^2 + 2 \text{up} \text{uxs} + \text{uxs}^2)^{3/2}} + \frac{\text{uxs}}{(L0^2 + \text{up}^2 + 2 \text{up} \text{uxs} + \text{uxs}^2)^{3/2}} \right) \\ & \left(-\frac{\text{up}}{\sqrt{L0^2 + \text{up}^2 + 2 \text{up} \text{uxs} + \text{uxs}^2}} - \frac{\text{uxs}}{\sqrt{L0^2 + \text{up}^2 + 2 \text{up} \text{uxs} + \text{uxs}^2}} \right) + \\ & \left(\frac{3 \text{up}^2}{2 (L0^2 + \text{up}^2 + 2 \text{up} \text{uxs} + \text{uxs}^2)^{5/2}} + \frac{3 \text{up} \text{uxs}}{(L0^2 + \text{up}^2 + 2 \text{up} \text{uxs} + \text{uxs}^2)^{5/2}} + \right. \\ & \left. \frac{3 \text{uxs}^2}{2 (L0^2 + \text{up}^2 + 2 \text{up} \text{uxs} + \text{uxs}^2)^{5/2}} - \frac{1}{2 (L0^2 + \text{up}^2 + 2 \text{up} \text{uxs} + \text{uxs}^2)^{3/2}} \right) \\ & \left. \left(-\sqrt{L0^2 + \text{uxs}^2} + \sqrt{L0^2 + \text{up}^2 + 2 \text{up} \text{uxs} + \text{uxs}^2} \right) \right) \Delta u^2 \Big) + \mathcal{O}[\Delta u]^3 \end{aligned}$$

■ Take the linear term and simplify

In[77] :=

$$\text{Simplify}\left[\frac{1}{\sqrt{L0^2 + uxs^2}} \left(-\frac{\sqrt{L0^2 + uxs^2} + \sqrt{L0^2 + up^2 + 2 up uxs + uxs^2}}{\sqrt{L0^2 + up^2 + 2 up uxs + uxs^2}} + \right. \right. \\ \left. \left. (up + uxs) \left(\frac{\frac{up}{\sqrt{L0^2 + up^2 + 2 up uxs + uxs^2}} - \frac{uxs}{\sqrt{L0^2 + up^2 + 2 up uxs + uxs^2}}}{\sqrt{L0^2 + up^2 + 2 up uxs + uxs^2}} + \left(\frac{up}{(L0^2 + up^2 + 2 up uxs + uxs^2)^{3/2}} + \right. \right. \right. \right. \\ \left. \left. \left. \frac{uxs}{(L0^2 + up^2 + 2 up uxs + uxs^2)^{3/2}} \right) \left(-\sqrt{L0^2 + uxs^2} + \sqrt{L0^2 + up^2 + 2 up uxs + uxs^2} \right) \right) \right] \Delta u]$$

$$\text{out}[77] = \frac{(- (up + uxs)^2 \sqrt{L0^2 + (up + uxs)^2} + L0^2 (\sqrt{L0^2 + uxs^2} - \sqrt{L0^2 + (up + uxs)^2})) \Delta u}{\sqrt{L0^2 + uxs^2} (L0^2 + (up + uxs)^2)^{3/2}}$$

■ Repeat for the bottom film. In this case the height is $up+uxs+\Delta u$

$$\begin{aligned}
 In[78] := & \text{Series}\left[\frac{up + uxs + \Delta u}{\sqrt{L0^2 + (up + uxs + \Delta u)^2}} * \frac{\sqrt{L0^2 + (up + uxs + \Delta u)^2} - \sqrt{L0^2 + uxs^2}}{\sqrt{L0^2 + uxs^2}}, \{\Delta u, 0, 2\}\right] \\
 Out[78] = & \frac{(up + uxs) \left(-\sqrt{L0^2 + uxs^2} + \sqrt{L0^2 + up^2 + 2 up uxs + uxs^2} \right)}{\sqrt{L0^2 + uxs^2} \sqrt{L0^2 + up^2 + 2 up uxs + uxs^2}} + \\
 & \frac{1}{\sqrt{L0^2 + uxs^2}} \left(\left(\frac{(up + uxs) \left(\frac{up}{\sqrt{L0^2 + up^2 + 2 up uxs + uxs^2}} + \frac{uxs}{\sqrt{L0^2 + up^2 + 2 up uxs + uxs^2}} \right)}{\sqrt{L0^2 + up^2 + 2 up uxs + uxs^2}} + \right. \right. \\
 & \left. \left(-\frac{(up + uxs) (2 up + 2 uxs)}{2 (L0^2 + up^2 + 2 up uxs + uxs^2)^{3/2}} + \frac{1}{\sqrt{L0^2 + up^2 + 2 up uxs + uxs^2}} \right) \right. \\
 & \left. \left. \left(-\sqrt{L0^2 + uxs^2} + \sqrt{L0^2 + up^2 + 2 up uxs + uxs^2} \right) \right) \Delta u \right) + \frac{1}{\sqrt{L0^2 + uxs^2}} \\
 & \left(\left((up + uxs) \left(-\frac{up^2}{2 (L0^2 + up^2 + 2 up uxs + uxs^2)^{3/2}} - \frac{up uxs}{(L0^2 + up^2 + 2 up uxs + uxs^2)^{3/2}} - \right. \right. \right. \\
 & \left. \left. \left. \frac{uxs^2}{2 (L0^2 + up^2 + 2 up uxs + uxs^2)^{3/2}} + \frac{1}{2 \sqrt{L0^2 + up^2 + 2 up uxs + uxs^2}} \right) \right) / \right. \\
 & \left. \left(\sqrt{L0^2 + up^2 + 2 up uxs + uxs^2} \right) + \left(-\frac{(up + uxs) (2 up + 2 uxs)}{2 (L0^2 + up^2 + 2 up uxs + uxs^2)^{3/2}} + \right. \right. \\
 & \left. \left. \frac{1}{\sqrt{L0^2 + up^2 + 2 up uxs + uxs^2}} \right) \right. \\
 & \left. \left(\frac{up}{\sqrt{L0^2 + up^2 + 2 up uxs + uxs^2}} + \frac{uxs}{\sqrt{L0^2 + up^2 + 2 up uxs + uxs^2}} \right) + \right. \\
 & \left. \left(-\sqrt{L0^2 + uxs^2} + \sqrt{L0^2 + up^2 + 2 up uxs + uxs^2} \right) \left(-\frac{2 up + 2 uxs}{2 (L0^2 + up^2 + 2 up uxs + uxs^2)^{3/2}} + \right. \right. \\
 & \left. \left. \frac{(up + uxs) \left(\frac{3 (2 up - 2 uxs)^2}{4 (L0^2 + up^2 + 2 up uxs + uxs^2)^2} - \frac{1}{L0^2 + up^2 + 2 up uxs + uxs^2} \right)}{2 \sqrt{L0^2 + up^2 + 2 up uxs + uxs^2}} \right) \right) \Delta u^2 \right) + O[\Delta u]^3
 \end{aligned}$$

■
Take linear term and simplify

$$\begin{aligned}
 \text{In}[79] := & \text{Simplify}\left[\frac{1}{\sqrt{L0^2 + uxs^2}} \left(\frac{(up + uxs) \left(\frac{up}{\sqrt{L0^2 + up^2 + 2 up uxs - uxs^2}} + \frac{uxs}{\sqrt{L0^2 + up^2 + 2 up uxs - uxs^2}} \right)}{\sqrt{L0^2 + up^2 + 2 up uxs + uxs^2}} + \left(-\frac{(up + uxs) (2 up + 2 uxs)}{2 (L0^2 + up^2 + 2 up uxs + uxs^2)^{3/2}} + \right. \right. \\
 & \left. \left. \frac{1}{\sqrt{L0^2 + up^2 + 2 up uxs + uxs^2}} \right) \left(-\sqrt{L0^2 + uxs^2} + \sqrt{L0^2 + up^2 + 2 up uxs + uxs^2} \right) \right] \Delta u \\
 \text{Out}[79] = & \frac{\left((up + uxs)^2 \sqrt{L0^2 + (up + uxs)^2} + L0^2 \left(-\sqrt{L0^2 + uxs^2} + \sqrt{L0^2 + (up + uxs)^2} \right) \right) \Delta u}{\sqrt{L0^2 + uxs^2} (L0^2 + (up + uxs)^2)^{3/2}}
 \end{aligned}$$

■
Consider just the dynamic strain term times $\cos\alpha$ for the top film

$$\begin{aligned}
 \text{In}[80] := & \text{Series}\left[\frac{up + uxs - \Delta u}{\sqrt{L0^2 + (up + uxs - \Delta u)^2}} * \frac{\sqrt{L0^2 + (up + uxs - \Delta u)^2} - \sqrt{L0^2 + (uxs + up)^2}}{\sqrt{L0^2 + (uxs + up)^2}}, \{\Delta u, 0, 2\}\right] \\
 \text{Out}[80] = & \frac{(-2 up - 2 uxs) (up + uxs) \Delta u}{2 (L0^2 + up^2 + 2 up uxs + uxs^2) \sqrt{L0^2 + (up + uxs)^2}} + \\
 & \frac{1}{\sqrt{L0^2 + (up + uxs)^2}} \left(-\frac{-2 up - 2 uxs}{2 (L0^2 + up^2 + 2 up uxs + uxs^2)} + \right. \\
 & (up + uxs) \left(\frac{(-2 up - 2 uxs) \left(\frac{up}{(L0^2 - up^2 + 2 up uxs - uxs^2)^{3/2}} + \frac{uxs}{(L0^2 - up^2 + 2 up uxs - uxs^2)^{3/2}} \right)}{2 \sqrt{L0^2 + up^2 + 2 up uxs + uxs^2}} + \right. \\
 & \left. \left. \frac{1}{2} \left(-\frac{(-2 up - 2 uxs)^2}{4 (L0^2 + up^2 + 2 up uxs + uxs^2)^2} + \frac{1}{L0^2 + up^2 + 2 up uxs + uxs^2} \right) \right) \right) \Delta u^2 + O[\Delta u]^3 \\
 \text{In}[81] := & \\
 & \text{Simplify}\left[\frac{(-2 up - 2 uxs) (up + uxs) \Delta u}{2 (L0^2 + up^2 + 2 up uxs + uxs^2) \sqrt{L0^2 + (up + uxs)^2}}\right] \\
 \text{Out}[81] = & -\frac{(up + uxs)^2 \Delta u}{(L0^2 + (up + uxs)^2)^{3/2}}
 \end{aligned}$$

■

And for the bottom film

$$\text{In}[83] := \text{Series}\left[\frac{\text{up} + \text{uxs} + \Delta\text{u}}{\sqrt{\text{L0}^2 + (\text{up} + \text{uxs} + \Delta\text{u})^2}} * \frac{\sqrt{\text{L0}^2 + (\text{up} + \text{uxs} + \Delta\text{u})^2} - \sqrt{\text{L0}^2 + (\text{uxs} + \text{up})^2}}{\sqrt{\text{L0}^2 + (\text{uxs} + \text{up})^2}}, \{\Delta\text{u}, 0, 2\}\right]$$

$$\begin{aligned} \text{Out}[83] = & \frac{(\text{up} + \text{uxs}) (2 \text{up} + 2 \text{uxs}) \Delta\text{u}}{2 (\text{L0}^2 + \text{up}^2 + 2 \text{up} \text{uxs} + \text{uxs}^2) \sqrt{\text{L0}^2 + (\text{up} + \text{uxs})^2}} + \frac{1}{\sqrt{\text{L0}^2 + (\text{up} + \text{uxs})^2}} \\ & \left(\left(\frac{1}{2} (\text{up} + \text{uxs}) \left(-\frac{(2 \text{up} + 2 \text{uxs})^2}{4 (\text{L0}^2 + \text{up}^2 + 2 \text{up} \text{uxs} + \text{uxs}^2)^2} + \frac{1}{\text{L0}^2 + \text{up}^2 + 2 \text{up} \text{uxs} + \text{uxs}^2} \right) + \right. \\ & \left. \frac{(2 \text{up} + 2 \text{uxs}) \left(-\frac{(\text{up} - \text{uxs}) (2 \text{up} + 2 \text{uxs})}{2 (\text{L0}^2 + \text{up}^2 + 2 \text{up} \text{uxs} + \text{uxs}^2)^{3/2}} + \frac{1}{\sqrt{\text{L0}^2 + \text{up}^2 + 2 \text{up} \text{uxs} + \text{uxs}^2}} \right)}{2 \sqrt{\text{L0}^2 + \text{up}^2 + 2 \text{up} \text{uxs} + \text{uxs}^2}} \right) \Delta\text{u}^2 \right) + \text{O}[\Delta\text{u}]^3 \end{aligned}$$

$$\text{In}[84] := \text{Simplify}\left[\frac{(\text{up} + \text{uxs}) (2 \text{up} + 2 \text{uxs}) \Delta\text{u}}{2 (\text{L0}^2 + \text{up}^2 + 2 \text{up} \text{uxs} + \text{uxs}^2) \sqrt{\text{L0}^2 + (\text{up} + \text{uxs})^2}}\right]$$

$$\text{Out}[84] = \frac{(\text{up} + \text{uxs})^2 \Delta\text{u}}{(\text{L0}^2 + (\text{up} + \text{uxs})^2)^{3/2}}$$

In[85] :=

■

Calculate the approx for $\cos\alpha$ for top film

$$\text{In}[86] := \text{Series}\left[\frac{\text{up} + \text{uxs} - \Delta\text{u}}{\sqrt{\text{L0}^2 + (\text{up} + \text{uxs} - \Delta\text{u})^2}}, \{\Delta\text{u}, 0, 2\}\right]$$

$$\begin{aligned} \text{Out}[86] = & \left(\frac{\text{up}}{\sqrt{\text{L0}^2 + \text{up}^2 + 2 \text{up} \text{uxs} + \text{uxs}^2}} + \frac{\text{uxs}}{\sqrt{\text{L0}^2 + \text{up}^2 + 2 \text{up} \text{uxs} + \text{uxs}^2}} \right) + \\ & \left(\frac{\text{up}^2}{(\text{L0}^2 + \text{up}^2 + 2 \text{up} \text{uxs} + \text{uxs}^2)^{3/2}} + \frac{2 \text{up} \text{uxs}}{(\text{L0}^2 + \text{up}^2 + 2 \text{up} \text{uxs} + \text{uxs}^2)^{3/2}} + \right. \\ & \left. \frac{\text{uxs}^2}{(\text{L0}^2 + \text{up}^2 + 2 \text{up} \text{uxs} + \text{uxs}^2)^{3/2}} - \frac{1}{\sqrt{\text{L0}^2 + \text{up}^2 + 2 \text{up} \text{uxs} + \text{uxs}^2}} \right) \Delta\text{u} + \\ & \left(\frac{3 \text{up}^3}{2 (\text{L0}^2 + \text{up}^2 + 2 \text{up} \text{uxs} + \text{uxs}^2)^{5/2}} + \frac{9 \text{up}^2 \text{uxs}}{2 (\text{L0}^2 + \text{up}^2 + 2 \text{up} \text{uxs} + \text{uxs}^2)^{5/2}} + \right. \\ & \left. \frac{9 \text{up} \text{uxs}^2}{2 (\text{L0}^2 + \text{up}^2 + 2 \text{up} \text{uxs} + \text{uxs}^2)^{5/2}} + \frac{3 \text{uxs}^3}{2 (\text{L0}^2 + \text{up}^2 + 2 \text{up} \text{uxs} + \text{uxs}^2)^{5/2}} - \right. \\ & \left. \frac{3 \text{up}}{2 (\text{L0}^2 + \text{up}^2 + 2 \text{up} \text{uxs} + \text{uxs}^2)^{3/2}} - \frac{3 \text{uxs}}{2 (\text{L0}^2 + \text{up}^2 + 2 \text{up} \text{uxs} + \text{uxs}^2)^{3/2}} \right) \Delta\text{u}^2 + \text{O}[\Delta\text{u}]^3 \end{aligned}$$

$$\text{In}[87] := \text{Simplify}\left[\left(\frac{\text{up}}{\sqrt{\text{L0}^2 + \text{up}^2 + 2 \text{up} \text{uxs} + \text{uxs}^2}} + \frac{\text{uxs}}{\sqrt{\text{L0}^2 + \text{up}^2 + 2 \text{up} \text{uxs} + \text{uxs}^2}}\right) + \left(\frac{\text{up}^2}{(\text{L0}^2 + \text{up}^2 + 2 \text{up} \text{uxs} + \text{uxs}^2)^{3/2}} + \frac{2 \text{up} \text{uxs}}{(\text{L0}^2 + \text{up}^2 + 2 \text{up} \text{uxs} + \text{uxs}^2)^{3/2}} + \frac{\text{uxs}^2}{(\text{L0}^2 + \text{up}^2 + 2 \text{up} \text{uxs} + \text{uxs}^2)^{3/2}} - \frac{1}{\sqrt{\text{L0}^2 + \text{up}^2 + 2 \text{up} \text{uxs} + \text{uxs}^2}}\right) \Delta u\right]$$

$$\text{Out}[87] = \frac{(\text{up} + \text{uxs})^3 + \text{L0}^2 (\text{up} + \text{uxs} - \Delta u)}{(\text{L0}^2 + (\text{up} + \text{uxs})^2)^{3/2}}$$

$$\text{In}[88] := \frac{(\text{up} + \text{uxs})^3 + \text{L0}^2 (\text{up} + \text{uxs} - \Delta u)}{(\text{L0}^2 + (\text{up} + \text{uxs})^2)^{3/2}}$$

$$\text{Out}[88] = \frac{(\text{up} + \text{uxs})^3 + \text{L0}^2 (\text{up} + \text{uxs} - \Delta u)}{(\text{L0}^2 + (\text{up} + \text{uxs})^2)^{3/2}}$$

$\text{In}[89] :=$

■ And for the bottom film

$$\text{In}[90] := \text{Series}\left[\frac{\text{up} + \text{uxs} + \Delta u}{\sqrt{\text{L0}^2 + (\text{up} + \text{uxs} + \Delta u)^2}}, \{\Delta u, 0, 2\}\right]$$

$$\text{Out}[90] = \frac{\text{up} + \text{uxs}}{\sqrt{\text{L0}^2 + \text{up}^2 + 2 \text{up} \text{uxs} + \text{uxs}^2}} + \left(-\frac{(\text{up} + \text{uxs}) (2 \text{up} + 2 \text{uxs})}{2 (\text{L0}^2 + \text{up}^2 + 2 \text{up} \text{uxs} + \text{uxs}^2)^{3/2}} + \frac{1}{\sqrt{\text{L0}^2 + \text{up}^2 + 2 \text{up} \text{uxs} + \text{uxs}^2}}\right) \Delta u + \left(-\frac{2 \text{up} + 2 \text{uxs}}{2 (\text{L0}^2 + \text{up}^2 + 2 \text{up} \text{uxs} + \text{uxs}^2)^{3/2}} + \frac{(\text{up} + \text{uxs}) \left(\frac{3 (2 \text{up} + 2 \text{uxs})^2}{4 (\text{L0}^2 + \text{up}^2 + 2 \text{up} \text{uxs} + \text{uxs}^2)^2} - \frac{1}{\text{L0}^2 + \text{up}^2 + 2 \text{up} \text{uxs} + \text{uxs}^2}\right)}{2 \sqrt{\text{L0}^2 + \text{up}^2 + 2 \text{up} \text{uxs} + \text{uxs}^2}}\right) \Delta u^2 + \mathcal{O}[\Delta u]^3$$

$$\text{In}[91] := \text{Simplify}\left[\frac{\text{up} + \text{uxs}}{\sqrt{\text{L0}^2 + \text{up}^2 + 2 \text{up} \text{uxs} + \text{uxs}^2}} + \left(-\frac{(\text{up} + \text{uxs}) (2 \text{up} + 2 \text{uxs})}{2 (\text{L0}^2 + \text{up}^2 + 2 \text{up} \text{uxs} + \text{uxs}^2)^{3/2}} + \frac{1}{\sqrt{\text{L0}^2 + \text{up}^2 + 2 \text{up} \text{uxs} + \text{uxs}^2}}\right) \Delta u\right]$$

$$\text{Out}[91] = \frac{(\text{up} + \text{uxs})^3 + \text{L0}^2 (\text{up} + \text{uxs} + \Delta u)}{(\text{L0}^2 + (\text{up} + \text{uxs})^2)^{3/2}}$$

- **Cos α for the small u approximation, ie top and bottom use the same value**

$$\text{In}[92] := \text{Series}\left[\frac{\text{up} + \text{uxs}}{\sqrt{\text{L0}^2 + (\text{up} + \text{uxs})^2}}, \{\Delta u, 0, 2\}\right]$$

$$\text{Out}[92] = \frac{\text{up} + \text{uxs}}{\sqrt{\text{L0}^2 + (\text{up} + \text{uxs})^2}}$$

- **Test solution for accuracy why doesn't it match the regular solution model when uxs=0?**

$$\text{In}[93] := \text{uxs} = 0$$

$$\text{Out}[93] = 0$$

$$\text{In}[94] := \frac{(-(\text{up} + \text{uxs})^2 \sqrt{\text{L0}^2 + (\text{up} + \text{uxs})^2} + \text{L0}^2 (\sqrt{\text{L0}^2 + \text{uxs}^2} - \sqrt{\text{L0}^2 + (\text{up} + \text{uxs})^2})) \Delta u}{\sqrt{\text{L0}^2 + \text{uxs}^2} (\text{L0}^2 + (\text{up} + \text{uxs})^2)^{3/2}}$$

$$\text{Out}[94] = \frac{(-\text{up}^2 \sqrt{\text{L0}^2 + \text{up}^2} + \text{L0}^2 (\sqrt{\text{L0}^2} - \sqrt{\text{L0}^2 + \text{up}^2})) \Delta u}{\sqrt{\text{L0}^2} (\text{L0}^2 + \text{up}^2)^{3/2}}$$

$$\text{In}[95] := \text{Simplify}\left[\frac{\text{up} (-\sqrt{\text{L0}^2} + \sqrt{\text{L0}^2 + \text{up}^2})}{\sqrt{\text{L0}^2} \sqrt{\text{L0}^2 + \text{up}^2}} + \frac{\left(-\frac{\sqrt{\text{L0}^2 + \sqrt{\text{L0}^2 + \text{up}^2}}}{\sqrt{\text{L0}^2 + \text{up}^2}} + \text{up} \left(-\frac{\text{up}}{\text{L0}^2 + \text{up}^2} + \frac{\text{up} (-\sqrt{\text{L0}^2} + \sqrt{\text{L0}^2 + \text{up}^2})}{(\text{L0}^2 + \text{up}^2)^{3/2}}\right)\right) \Delta u}{\sqrt{\text{L0}^2}}\right]$$

$$\text{Out}[95] = \frac{1}{\sqrt{\text{L0}^2} (\text{L0}^2 + \text{up}^2)^{3/2}} \left(\text{up}^3 (-\sqrt{\text{L0}^2} + \sqrt{\text{L0}^2 + \text{up}^2}) + \text{up} \left(-(\text{L0}^2)^{3/2} + \text{L0}^2 \sqrt{\text{L0}^2 + \text{up}^2}\right) - \text{up}^2 \sqrt{\text{L0}^2 + \text{up}^2} \Delta u + \left((\text{L0}^2)^{3/2} - \text{L0}^2 \sqrt{\text{L0}^2 + \text{up}^2}\right) \Delta u\right)$$

$$\text{In}[96] :=$$

$$\text{In}[97] := \frac{\text{up} + \text{uxs} - \Delta u}{\sqrt{\text{L0}^2 + (\text{up} + \text{uxs} - \Delta u)^2}} * \frac{\sqrt{\text{L0}^2 + (\text{up} + \text{uxs} - \Delta u)^2} - \sqrt{\text{L0}^2 + \text{uxs}^2}}{\sqrt{\text{L0}^2 + \text{uxs}^2}}$$

$$\text{Out}[97] = \frac{(-\sqrt{\text{L0}^2} + \sqrt{\text{L0}^2 + (\text{up} - \Delta u)^2}) (\text{up} - \Delta u)}{\sqrt{\text{L0}^2} \sqrt{\text{L0}^2 + (\text{up} - \Delta u)^2}}$$

In[98]:=

Series[% , {Δu, 0, 2}]

$$\text{Out}[98]= \frac{\text{up} \left(-\sqrt{L0^2} + \sqrt{L0^2 + \text{up}^2} \right)}{\sqrt{L0^2} \sqrt{L0^2 + \text{up}^2}} + \frac{\left(-\frac{-\sqrt{L0^2} + \sqrt{L0^2 + \text{up}^2}}{\sqrt{L0^2 + \text{up}^2}} + \text{up} \left(-\frac{\text{up}}{L0^2 + \text{up}^2} + \frac{\text{up} \left(-\sqrt{L0^2} + \sqrt{L0^2 + \text{up}^2} \right)}{(L0^2 + \text{up}^2)^{3/2}} \right) \right) \Delta u}{\sqrt{L0^2}} + \frac{1}{\sqrt{L0^2}}$$

$$\left(\left(\frac{\text{up}}{L0^2 + \text{up}^2} - \frac{\text{up} \left(-\sqrt{L0^2} + \sqrt{L0^2 + \text{up}^2} \right)}{(L0^2 + \text{up}^2)^{3/2}} + \text{up} \left(-\frac{\text{up}^2}{(L0^2 + \text{up}^2)^2} + \frac{-\frac{\text{up}^2}{2 (L0^2 + \text{up}^2)^{5/2}} + \frac{1}{2 \sqrt{L0^2 + \text{up}^2}}}{\sqrt{L0^2} + \text{up}^2} \right. \right. \right.$$

$$\left. \left. \left(\frac{3 \text{up}^2}{2 (L0^2 + \text{up}^2)^{5/2}} - \frac{1}{2 (L0^2 + \text{up}^2)^{3/2}} \right) \left(-\sqrt{L0^2} + \sqrt{L0^2 + \text{up}^2} \right) \right) \right) \Delta u^2 \right) + \text{O}[\Delta u]^3$$

In[99]:= **Simplify** $\left[\frac{\left(-\frac{-\sqrt{L0^2} + \sqrt{L0^2 + \text{up}^2}}{\sqrt{L0^2 + \text{up}^2}} + \text{up} \left(-\frac{\text{up}}{L0^2 + \text{up}^2} + \frac{\text{up} \left(-\sqrt{L0^2} + \sqrt{L0^2 + \text{up}^2} \right)}{(L0^2 + \text{up}^2)^{3/2}} \right) \right)}{\sqrt{L0^2}} \right]$

$$\text{Out}[99]= \frac{(L0^2)^{3/2} - L0^2 \sqrt{L0^2 + \text{up}^2} - \text{up}^2 \sqrt{L0^2 + \text{up}^2}}{\sqrt{L0^2} (L0^2 + \text{up}^2)^{3/2}}$$

In[100]:=

$$\frac{\text{up} - \Delta u}{\sqrt{L0^2 + (\text{up} - \Delta u)^2}} * \frac{\sqrt{L0^2 + (\text{up} - \Delta u)^2} - L0}{L0};$$

Series[% , {Δu, 0, 3}]

Out[101]=

$$\frac{\text{up} \left(-L0 + \sqrt{L0^2 + \text{up}^2} \right)}{L0 \sqrt{L0^2 + \text{up}^2}} + \frac{\left(-\frac{-L0 + \sqrt{L0^2 + \text{up}^2}}{\sqrt{L0^2 + \text{up}^2}} + \text{up} \left(-\frac{\text{up}}{L0^2 + \text{up}^2} + \frac{\text{up} \left(-L0 + \sqrt{L0^2 + \text{up}^2} \right)}{(L0^2 + \text{up}^2)^{3/2}} \right) \right) \Delta u}{L0} + \frac{1}{L0}$$

$$\left(\left(\frac{\text{up}}{L0^2 + \text{up}^2} - \frac{\text{up} \left(-L0 + \sqrt{L0^2 + \text{up}^2} \right)}{(L0^2 + \text{up}^2)^{3/2}} + \text{up} \left(-\frac{\text{up}^2}{(L0^2 + \text{up}^2)^2} + \frac{-\frac{\text{up}^2}{2 (L0^2 + \text{up}^2)^{5/2}} + \frac{1}{2 \sqrt{L0^2 + \text{up}^2}}}{\sqrt{L0^2} + \text{up}^2} \right. \right. \right.$$

$$\left. \left. \left(\frac{3 \text{up}^2}{2 (L0^2 + \text{up}^2)^{5/2}} - \frac{1}{2 (L0^2 + \text{up}^2)^{3/2}} \right) \left(-L0 + \sqrt{L0^2 + \text{up}^2} \right) \right) \right) \Delta u^2 \right) + \frac{1}{L0}$$

$$\left(\left(\frac{\text{up}^2}{(L0^2 + \text{up}^2)^2} - \frac{-\frac{\text{up}^2}{2 (L0^2 + \text{up}^2)^{5/2}} + \frac{1}{2 \sqrt{L0^2 + \text{up}^2}}}{\sqrt{L0^2} + \text{up}^2} - \left(\frac{3 \text{up}^2}{2 (L0^2 + \text{up}^2)^{5/2}} - \frac{1}{2 (L0^2 + \text{up}^2)^{3/2}} \right) \right. \right.$$

$$\left. \left(-L0 + \sqrt{L0^2 + \text{up}^2} \right) + \text{up} \left(-\frac{\text{up} \left(\frac{3 \text{up}^2}{2 (L0^2 + \text{up}^2)^{5/2}} - \frac{1}{2 (L0^2 + \text{up}^2)^{3/2}} \right)}{\sqrt{L0^2} + \text{up}^2} + \right.$$

$$\left. \frac{-\frac{\text{up}^2}{2 (L0^2 + \text{up}^2)^{5/2}} + \frac{\text{up}}{2 (L0^2 + \text{up}^2)^{3/2}}}{\sqrt{L0^2} + \text{up}^2} + \frac{\text{up} \left(-\frac{\text{up}^2}{2 (L0^2 + \text{up}^2)^{3/2}} + \frac{1}{2 \sqrt{L0^2 + \text{up}^2}} \right)}{(L0^2 + \text{up}^2)^{3/2}} \right) +$$

$$\left(\frac{5 \text{up}^3}{2 (L0^2 + \text{up}^2)^{7/2}} - \frac{3 \text{up}}{2 (L0^2 + \text{up}^2)^{5/2}} \right) \left(-L0 + \sqrt{L0^2 + \text{up}^2} \right) \right) \Delta u^3 \right) + \text{O}[\Delta u]^4$$

In[102]:=

$$\text{Simplify}\left[\frac{\left(-\frac{-L0+\sqrt{L0^2+up^2}}{\sqrt{L0^2+up^2}} + up\left(-\frac{up}{L0^2+up^2} + \frac{up(-L0+\sqrt{L0^2+up^2})}{(L0^2+up^2)^{3/2}}\right)\right)}{L0}\right]$$

Out[102]=

$$-\frac{1}{L0} + \frac{L0^2}{(L0^2 + up^2)^{3/2}}$$

In[103]:=

$$x := -\frac{1}{L0} + \frac{L0^2}{(L0^2 + up^2)^{3/2}}$$

$$y := \frac{(L0^2)^{3/2} - L0^2 \sqrt{L0^2 + up^2} - up^2 \sqrt{L0^2 + up^2}}{\sqrt{L0^2} (L0^2 + up^2)^{3/2}}$$

$$z := \frac{(- (up + uxs)^2 \sqrt{L0^2 + (up + uxs)^2} + L0^2 (\sqrt{L0^2 + uxs^2} - \sqrt{L0^2 + (up + uxs)^2}))}{\sqrt{L0^2 + uxs^2} (L0^2 + (up + uxs)^2)^{3/2}}$$

L0 = 50;

up = 4;

uxs = 0;

N[x]

N[y]

N[z]

Out[109]=

-0.000190475

Out[110]=

-0.000190475

Out[111]=

-0.000190475

- This sheet develops the power equations using the xs model including the dynamic $\cos \alpha$ term rather than the approximate term. Equations are imported from other sheets that develop coupling term Ψ and stiffness s .

$$\frac{d1t1}{L0} \text{ csa1} = x1$$

and

$$\frac{d1t1}{L0} \text{ csa2} = x2$$

```
In[44]:= Clear[Fu, F1, Ft, up, uxs, L0, csa1, csa2, Vu, V1, d31, w, s11,
           d1t1, x1, x2, Ξ, s, ωn, R, Rm, C0, ε3, h, pwr, A, fcn1, fcn2, m]
```

$$\begin{aligned} \Xi &:= \frac{2 w d31}{s11} \left(\frac{up + uxs}{L0} \frac{1}{\left(1 + \left(\frac{up+uxs}{L0}\right)^2\right)^{\frac{1}{2}}} \right) \\ s &:= -\frac{4 w h}{s11} \left(\left(- (up + uxs)^2 \sqrt{L0^2 + (up + uxs)^2} + L0^2 \left(\sqrt{L0^2 + uxs^2} - \sqrt{L0^2 + (up + uxs)^2} \right) \right) / \right. \\ &\quad \left. \left(\sqrt{L0^2 + uxs^2} (L0^2 + (up + uxs)^2)^{3/2} \right) \right) \end{aligned}$$

```
In[47]:= Ξ
          s
```

$$\text{Out[47]} = \frac{2 d31 (up + uxs) w}{L0 s11 \sqrt{1 + \frac{(up+uxs)^2}{L0^2}}}$$

$$\text{Out[48]} = -\frac{4 h \left(- (up + uxs)^2 \sqrt{L0^2 + (up + uxs)^2} + L0^2 \left(\sqrt{L0^2 + uxs^2} - \sqrt{L0^2 + (up + uxs)^2} \right) \right) w}{s11 \sqrt{L0^2 + uxs^2} (L0^2 + (up + uxs)^2)^{3/2}}$$

```
In[49]:=
```

$$R := \frac{Rm}{\Xi^2}$$

$$C0 := \frac{\epsilon3 \left(1 - \frac{d31^2}{s11 \epsilon3}\right) w \sqrt{L0^2 + uxs^2}}{h}$$

$$\omega n := \sqrt{\frac{s}{m}}$$

```
In[52]:= R
          C0
          ωn
```

$$\text{Out[52]} = \frac{L0^2 Rm s11^2 \left(1 + \frac{(up+uxs)^2}{L0^2}\right)}{4 d31^2 (up+uxs)^2 w^2}$$

$$\text{Out[53]} = \frac{\sqrt{L0^2 + uxs^2} w \left(1 - \frac{d31^2}{s11 \epsilon 3}\right) \epsilon 3}{h}$$

$$\text{Out[54]} = 2 \sqrt{-\frac{h \left(- (up+uxs)^2 \sqrt{L0^2 + (up+uxs)^2} + L0^2 \left(\sqrt{L0^2 + uxs^2} - \sqrt{L0^2 + (up+uxs)^2}\right)\right) w}{m s11 \sqrt{L0^2 + uxs^2} (L0^2 + (up+uxs)^2)^{3/2}}}$$

- Use the developed equation for optimal power (symbolized here as pwr) from the original model development. Allow the substitutions from the xs model development terms to populate the equation.

```
In[55]:= pwr := \frac{1}{4 Rm} \frac{1}{\sqrt{1 + (R C0 \omega n)^2 + 1}} m^2 A^2
```

```
In[56]:=
          pwr
```

$$\text{Out[56]} = (A^2 m^2) / \left(4 Rm \left(1 + \sqrt{1 - \left(L0^4 Rm^2 s11^3 \sqrt{L0^2 + uxs^2} \left(1 + \frac{(up+uxs)^2}{L0^2} \right)^2 \left(- (up+uxs)^2 \sqrt{L0^2 + (up+uxs)^2} + L0^2 \left(\sqrt{L0^2 + uxs^2} - \sqrt{L0^2 + (up+uxs)^2} \right) \right) \left(1 - \frac{d31^2}{s11 \epsilon 3} \right)^2 \epsilon 3^2 \right)} \right) / \left(4 d31^4 h m (up+uxs)^4 (L0^2 + (up+uxs)^2)^{3/2} w \right) \right)$$

```
In[57]:=
          Simplify[pwr]
```

$$\text{Out[57]} = (A^2 m^2) / \left(2 Rm \left(2 + 2 \sqrt{1 - \left(Rm^2 s11 \sqrt{L0^2 + uxs^2} \sqrt{L0^2 + (up+uxs)^2} \left(- (up+uxs)^2 \sqrt{L0^2 + (up+uxs)^2} + L0^2 \left(\sqrt{L0^2 + uxs^2} - \sqrt{L0^2 + (up+uxs)^2} \right) \right) \right) \right) / \left((d31^2 - s11 \epsilon 3)^2 \right) / \left(4 d31^4 h m (up+uxs)^4 w \right) \right)$$

- Now evaluate a function f_{cn1} pwr / A^2 substituting values for all other terms then plot the function versus changes in uxs to see if there is a max or min to the function.

```
In[58] :=
```

$$f_{cn1}[uxs_] := \frac{pwr}{A^2}$$

- Define a new function $f_{cn2} = (RC\omega)^2$

```
In[59] :=
```

$$f_{cn2}[uxs_] := (RC\omega)^2$$

- assign values to variables: use values from 1st 119 μm Film" spreadsheet at 119 Hz

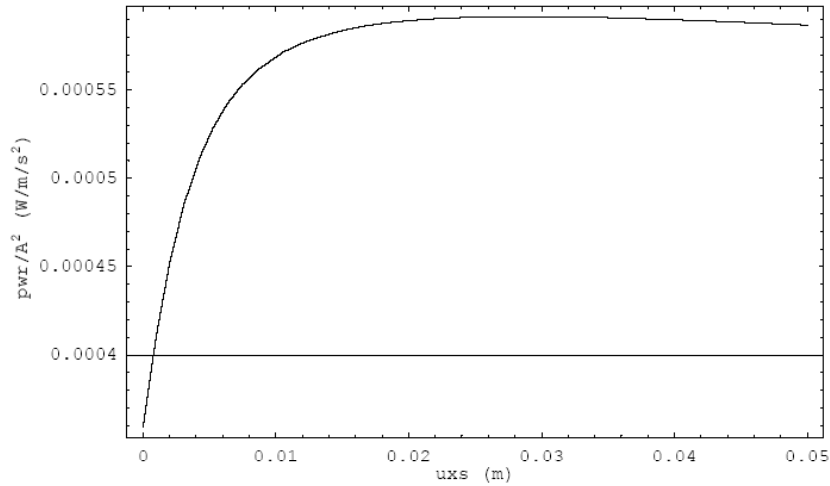
```
In[60] :=
```

```
m = .0823;  
Rm = 1.36;  
s11 = 3.65 10-10;  
d31 = 2.3 10-11;  
ε3 = 1.1 10-10;  
L0 = .022;  
w = .024;  
h = 1.19 10-4;  
up = .00359;
```

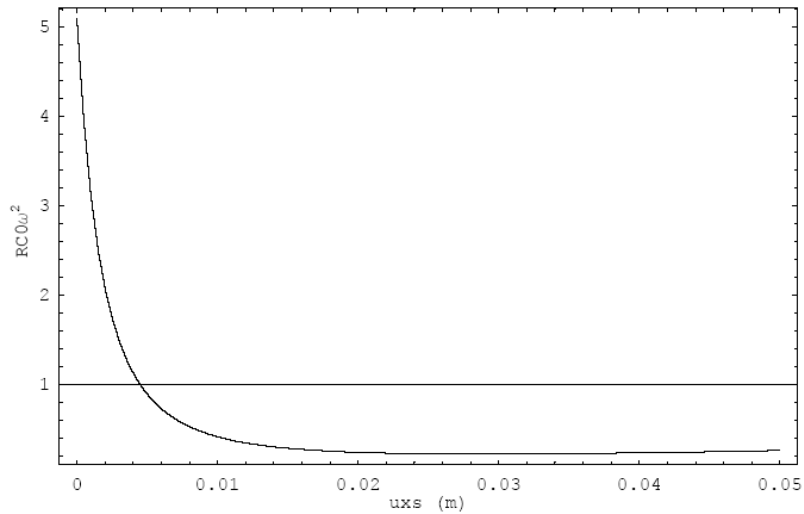
```

In[69]:= plot1 := Plot[fcn1[uxs], {uxs, 0, .05}]
plot2 := Plot[fcn2[uxs], {uxs, 0, .05}]
Show[plot1, Frame → True,
  FrameLabel → {"uxs (m)", " pwr/A2 (W/m/s2)"}, PlotRange → All]
Show[plot2, Frame → True,
  FrameLabel → {"uxs (m)", " RC0ω2"}, PlotRange → All]

```



Out[71]= - Graphics -



Out[72]= - Graphics -

- Plot the variation of ω and Ψ as functions of uxs .
Assign $fcn3 = \omega$ as a function of uxs , $fcn4 = \Psi$ as a function of uxs , and $fcn5 = s$ as a

function of uxs

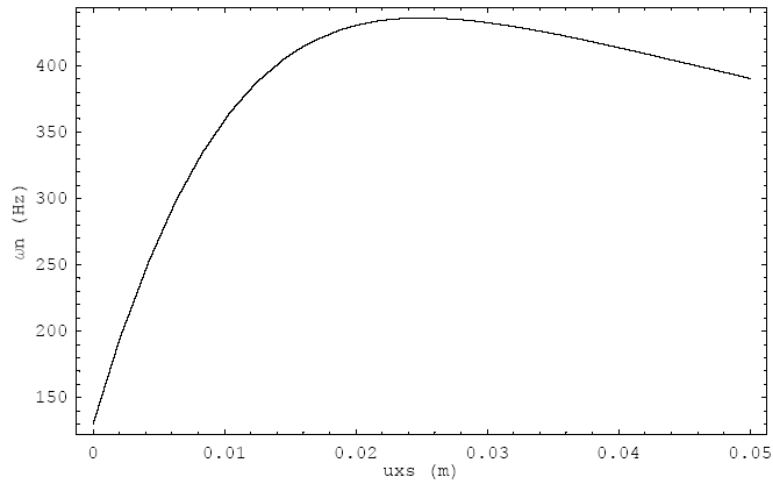
```

In[73]:= fcn3[uxs_] :=  $\frac{1}{2\pi} \sqrt{\frac{s}{m}}$ 
          fcn4[uxs_] :=  $\Psi$ 
          fcn5[uxs_] := s
          plot3 := Plot[fcn3[uxs], {uxs, 0, .05}]

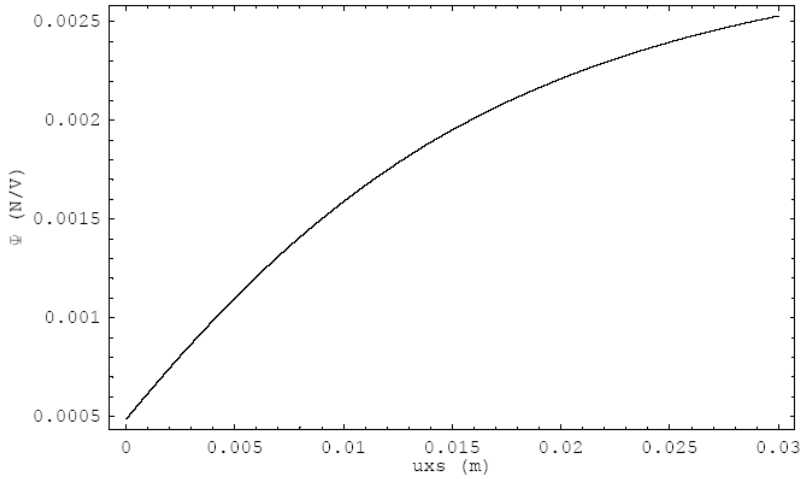
          plot4 := Plot[fcn4[uxs], {uxs, 0, .03}]
          plot5 := Plot[fcn5[uxs], {uxs, 0, .03}]

          Show[plot3, Frame → True,
               FrameLabel → {"uxs (m)", " $\omega_n$  (Hz)"}, PlotRange → All]
          Show[plot4, Frame → True,
               FrameLabel → {"uxs (m)", " $\Psi$  (N/V)"}, PlotRange → All]
          Show[plot5, Frame → True,
               FrameLabel → {"uxs (m)", "s (N/m)"}, PlotRange → All]

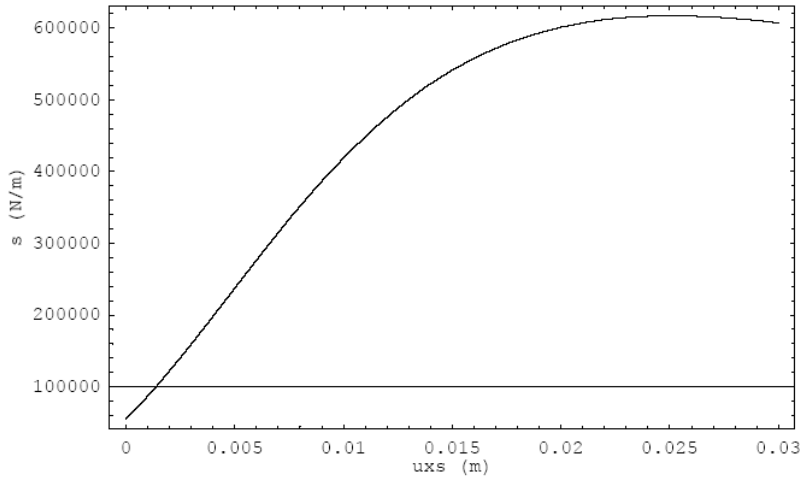
```



```
Out[79]= - Graphics -
```



Out[80]= - Graphics -



Out[81]= - Graphics -

```
In[82]:= uxs = 0  
s  
 $\Phi$   
 $\Phi^2$   
 $\omega n / (2 \pi)$ 
```

```
Out[82]= 0
```

```
Out[83]= 54990.4
```

```
Out[84]= 0.000487126
```

```
Out[85]=  $2.37292 \times 10^{-7}$ 
```

```
Out[86]= 130.096
```

■
Because of the idiosyncracies of Mathematica, let replace

$$\frac{d1t1}{L0} \text{ csa1} = x1$$

and

$$\frac{d1t1}{L0} \text{ csa2} = x2$$

```
Clear[Fu, F1, Ft, up, uxs, L0, csa1, csa2, Vu, V1, d31, w, s11, d1t1, x1, x2]
```

$$Fu = \frac{wh}{s11} * x1 + \frac{d31 w}{s11} * csa1 * Vu$$

$$F1 = -\frac{wh}{s11} * x2 + \frac{d31 w}{s11} * csa2 * V1$$

$$\frac{csa1 d31 Vu w}{s11} + \frac{h w x1}{s11}$$

$$\frac{csa2 d31 V1 w}{s11} - \frac{h w x2}{s11}$$

- using the results for the Taylor approxiamtoions from "RXMR Tlr App cas a total strain xs.nb" make the following linear term substitutions:

$$\begin{aligned}
 \mathbf{x1} &= \frac{(\mathbf{up} + \mathbf{uxs}) \left(-\sqrt{\mathbf{L0}^2 + \mathbf{uxs}^2} + \sqrt{\mathbf{L0}^2 + \mathbf{up}^2 + 2 \mathbf{up} \mathbf{uxs} + \mathbf{uxs}^2} \right)}{\sqrt{\mathbf{L0}^2 + \mathbf{uxs}^2} \sqrt{\mathbf{L0}^2 + \mathbf{up}^2 + 2 \mathbf{up} \mathbf{uxs} + \mathbf{uxs}^2}} + \\
 &\frac{1}{\sqrt{\mathbf{L0}^2 + \mathbf{uxs}^2}} \left(\left(-\frac{\sqrt{\mathbf{L0}^2 + \mathbf{uxs}^2} + \sqrt{\mathbf{L0}^2 + \mathbf{up}^2 + 2 \mathbf{up} \mathbf{uxs} + \mathbf{uxs}^2}}{\sqrt{\mathbf{L0}^2 + \mathbf{up}^2 + 2 \mathbf{up} \mathbf{uxs} + \mathbf{uxs}^2}} + \right. \right. \\
 &\quad \left. \left. (\mathbf{up} + \mathbf{uxs}) \left(\frac{-\frac{\mathbf{up}}{\sqrt{\mathbf{L0}^2 + \mathbf{up}^2 + 2 \mathbf{up} \mathbf{uxs} + \mathbf{uxs}^2}} - \frac{\mathbf{uxs}}{\sqrt{\mathbf{L0}^2 + \mathbf{up}^2 + 2 \mathbf{up} \mathbf{uxs} + \mathbf{uxs}^2}}}{\sqrt{\mathbf{L0}^2 + \mathbf{up}^2 + 2 \mathbf{up} \mathbf{uxs} + \mathbf{uxs}^2}} + \right. \right. \right. \\
 &\quad \left. \left. \left(\frac{\mathbf{up}}{(\mathbf{L0}^2 + \mathbf{up}^2 + 2 \mathbf{up} \mathbf{uxs} + \mathbf{uxs}^2)^{3/2}} + \frac{\mathbf{uxs}}{(\mathbf{L0}^2 + \mathbf{up}^2 + 2 \mathbf{up} \mathbf{uxs} + \mathbf{uxs}^2)^{3/2}} \right) \right) \right) \Delta \mathbf{u} \Bigg); \\
 \mathbf{x2} &= \frac{(\mathbf{up} + \mathbf{uxs}) \left(-\sqrt{\mathbf{L0}^2 + \mathbf{uxs}^2} + \sqrt{\mathbf{L0}^2 + \mathbf{up}^2 + 2 \mathbf{up} \mathbf{uxs} + \mathbf{uxs}^2} \right)}{\sqrt{\mathbf{L0}^2 + \mathbf{uxs}^2} \sqrt{\mathbf{L0}^2 + \mathbf{up}^2 + 2 \mathbf{up} \mathbf{uxs} + \mathbf{uxs}^2}} + \frac{1}{\sqrt{\mathbf{L0}^2 + \mathbf{uxs}^2}} \\
 &\left(\left(\frac{(\mathbf{up} + \mathbf{uxs}) \left(\frac{\mathbf{up}}{\sqrt{\mathbf{L0}^2 + \mathbf{up}^2 + 2 \mathbf{up} \mathbf{uxs} + \mathbf{uxs}^2}} + \frac{\mathbf{uxs}}{\sqrt{\mathbf{L0}^2 + \mathbf{up}^2 + 2 \mathbf{up} \mathbf{uxs} + \mathbf{uxs}^2}} \right)}{\sqrt{\mathbf{L0}^2 + \mathbf{up}^2 + 2 \mathbf{up} \mathbf{uxs} + \mathbf{uxs}^2}} + \left(-\frac{(\mathbf{up} + \mathbf{uxs}) (2 \mathbf{up} + 2 \mathbf{uxs})}{2 (\mathbf{L0}^2 + \mathbf{up}^2 + 2 \mathbf{up} \mathbf{uxs} + \mathbf{uxs}^2)^{3/2}} + \right. \right. \right. \\
 &\quad \left. \left. \left. \frac{1}{\sqrt{\mathbf{L0}^2 + \mathbf{up}^2 + 2 \mathbf{up} \mathbf{uxs} + \mathbf{uxs}^2}} \right) \left(-\sqrt{\mathbf{L0}^2 + \mathbf{uxs}^2} + \sqrt{\mathbf{L0}^2 + \mathbf{up}^2 + 2 \mathbf{up} \mathbf{uxs} + \mathbf{uxs}^2} \right) \right) \right) \Delta \mathbf{u} \Bigg); \\
 \mathbf{csa1} &= \left(\frac{\mathbf{up}}{\sqrt{\mathbf{L0}^2 + \mathbf{up}^2 + 2 \mathbf{up} \mathbf{uxs} + \mathbf{uxs}^2}} + \frac{\mathbf{uxs}}{\sqrt{\mathbf{L0}^2 + \mathbf{up}^2 + 2 \mathbf{up} \mathbf{uxs} + \mathbf{uxs}^2}} \right) + \\
 &\left(\frac{\mathbf{up}^2}{(\mathbf{L0}^2 + \mathbf{up}^2 + 2 \mathbf{up} \mathbf{uxs} + \mathbf{uxs}^2)^{3/2}} + \frac{2 \mathbf{up} \mathbf{uxs}}{(\mathbf{L0}^2 + \mathbf{up}^2 + 2 \mathbf{up} \mathbf{uxs} + \mathbf{uxs}^2)^{3/2}} + \right. \\
 &\quad \left. \frac{\mathbf{uxs}^2}{(\mathbf{L0}^2 + \mathbf{up}^2 + 2 \mathbf{up} \mathbf{uxs} + \mathbf{uxs}^2)^{3/2}} - \frac{1}{\sqrt{\mathbf{L0}^2 + \mathbf{up}^2 + 2 \mathbf{up} \mathbf{uxs} + \mathbf{uxs}^2}} \right) \Delta \mathbf{u}; \\
 \mathbf{csa2} &= \frac{\mathbf{up} + \mathbf{uxs}}{\sqrt{\mathbf{L0}^2 + \mathbf{up}^2 + 2 \mathbf{up} \mathbf{uxs} + \mathbf{uxs}^2}} + \\
 &\left(-\frac{(\mathbf{up} + \mathbf{uxs}) (2 \mathbf{up} + 2 \mathbf{uxs})}{2 (\mathbf{L0}^2 + \mathbf{up}^2 + 2 \mathbf{up} \mathbf{uxs} + \mathbf{uxs}^2)^{3/2}} + \frac{1}{\sqrt{\mathbf{L0}^2 + \mathbf{up}^2 + 2 \mathbf{up} \mathbf{uxs} + \mathbf{uxs}^2}} \right) \Delta \mathbf{u};
 \end{aligned}$$

Fu

F1

$$\begin{aligned}
 & \frac{1}{s11} \left(d31 \vee u w \left(\frac{up}{\sqrt{L0^2 + up^2 + 2 up uxs + uxs^2}} + \frac{uxs}{\sqrt{L0^2 + up^2 + 2 up uxs + uxs^2}} + \right. \right. \\
 & \quad \left(\frac{up^2}{(L0^2 + up^2 + 2 up uxs + uxs^2)^{3/2}} + \frac{2 up uxs}{(L0^2 + up^2 + 2 up uxs + uxs^2)^{3/2}} + \right. \\
 & \quad \left. \left. \frac{uxs^2}{(L0^2 + up^2 + 2 up uxs + uxs^2)^{3/2}} - \frac{1}{\sqrt{L0^2 + up^2 + 2 up uxs + uxs^2}} \right) \Delta u \right) + \\
 & \frac{1}{s11} \left(h w \left(\frac{(up + uxs) (-\sqrt{L0^2 + uxs^2} + \sqrt{L0^2 + up^2 + 2 up uxs + uxs^2})}{\sqrt{L0^2 + uxs^2} \sqrt{L0^2 + up^2 + 2 up uxs + uxs^2}} + \right. \right. \\
 & \quad \frac{1}{\sqrt{L0^2 + uxs^2}} \left(\left(-\frac{\sqrt{L0^2 + uxs^2} + \sqrt{L0^2 + up^2 + 2 up uxs + uxs^2}}{\sqrt{L0^2 + up^2 + 2 up uxs + uxs^2}} + \right. \right. \\
 & \quad \left. \left. (up + uxs) \left(\frac{-\frac{up}{\sqrt{L0^2 + up^2 + 2 up uxs + uxs^2}} - \frac{uxs}{\sqrt{L0^2 + up^2 + 2 up uxs + uxs^2}}}{\sqrt{L0^2 + up^2 + 2 up uxs + uxs^2}} + \right. \right. \right. \\
 & \quad \left. \left. \left(\frac{up}{(L0^2 + up^2 + 2 up uxs + uxs^2)^{3/2}} + \frac{uxs}{(L0^2 + up^2 + 2 up uxs + uxs^2)^{3/2}} \right) \right) \right) \Delta u \right) \left. \right) \\
 & \frac{1}{s11} \left(d31 \vee l w \left(\frac{up + uxs}{\sqrt{L0^2 + up^2 + 2 up uxs + uxs^2}} + \right. \right. \\
 & \quad \left. \left(-\frac{(up + uxs) (2 up + 2 uxs)}{2 (L0^2 + up^2 + 2 up uxs + uxs^2)^{3/2}} + \frac{1}{\sqrt{L0^2 + up^2 + 2 up uxs + uxs^2}} \right) \Delta u \right) - \\
 & \frac{1}{s11} \left(h w \left(\frac{(up + uxs) (-\sqrt{L0^2 + uxs^2} + \sqrt{L0^2 + up^2 + 2 up uxs + uxs^2})}{\sqrt{L0^2 + uxs^2} \sqrt{L0^2 + up^2 + 2 up uxs + uxs^2}} + \right. \right. \\
 & \quad \frac{1}{\sqrt{L0^2 + uxs^2}} \left(\left(\frac{(up + uxs) \left(\frac{up}{\sqrt{L0^2 + up^2 + 2 up uxs + uxs^2}} + \frac{uxs}{\sqrt{L0^2 + up^2 + 2 up uxs + uxs^2}} \right)}{\sqrt{L0^2 + up^2 + 2 up uxs + uxs^2}} + \right. \right. \\
 & \quad \left. \left(-\frac{(up + uxs) (2 up + 2 uxs)}{2 (L0^2 + up^2 + 2 up uxs + uxs^2)^{3/2}} + \frac{1}{\sqrt{L0^2 + up^2 + 2 up uxs + uxs^2}} \right) \right) \right) \Delta u \left. \right) \\
 & \quad \left(-\sqrt{L0^2 + uxs^2} + \sqrt{L0^2 + up^2 + 2 up uxs + uxs^2} \right) \left. \right) \left. \right)
 \end{aligned}$$

A2.4 Variation of ω_n with u_p , u_{xs} low freq.nb
 Variation of ω_n with u_p , u_{xs} low freq.nb

In[1553]:=

(* This sheet shows the variation of frequency with changes to two adjustable parameters u_{xs} and u_p . The stiffness s is defined as a function of u_p and u_{xs} : $s = s(u_{xs}, u_p)$. In this treatment the goal is to achieve a low frequency natural resonance and as such the mass and geometric term L_0 are modified from the initial RXMR (81 g) model. The mass changes from 81 g to 800 g and L_0 changes from 22 mm to 42 mm. The value for u_p is changed to maintain the stiffness term similar to the previous treatment. The range of u_{xs} is enough to capture the peak at about 45 degrees. *)

Clear[u_p , u_{xs} , L_0 , d_{31} , w , s_{11} , ϵ_3 , s , ω_n , h , f_{cn3} , f_{cn31} , f_{cn32} , m]

(* Define the stiffness s as a function of u_{xs} and u_p *)

$$s[u_p, u_{xs}] := -\frac{4wh}{s_{11}} \left(\left(-(u_p + u_{xs})^2 \sqrt{L_0^2 + (u_p + u_{xs})^2} + L_0^2 \left(\sqrt{L_0^2 + u_{xs}^2} - \sqrt{L_0^2 + (u_p + u_{xs})^2} \right) \right) / \left(\sqrt{L_0^2 + u_{xs}^2} (L_0^2 + (u_p + u_{xs})^2)^{3/2} \right) \right)$$

(* Assign values to the terms in the equation. These are the values from "1st 119 micron film excel spreadsheet" except m and L_0 *)

$m = .8$;
 $R_m = 1.36$;
 $s_{11} = 3.65 \cdot 10^{-10}$;
 $d_{31} = 2.3 \cdot 10^{-11}$;
 $\epsilon_3 = 1.1 \cdot 10^{-10}$;
 $L_0 = .042$;
 $w = .024$;
 $h = 1.19 \cdot 10^{-4}$;

(* f_{cn3} , f_{cn31} , and f_{cn32} are calculations for natural frequency defined as functions of u_{xs} and u_p *)

$$f_{cn3}[u_{xs}, u_p] := \frac{1}{2\pi} \sqrt{\frac{s[u_p, u_{xs}]}{m}}$$

$$f_{cn31}[u_{xs}, u_p] := \frac{1}{2\pi} \sqrt{\frac{s[u_p, u_{xs}]}{m}}$$

$$f_{cn32}[u_{xs}, u_p] := \frac{1}{2\pi} \sqrt{\frac{s[u_p, u_{xs}]}{m}}$$

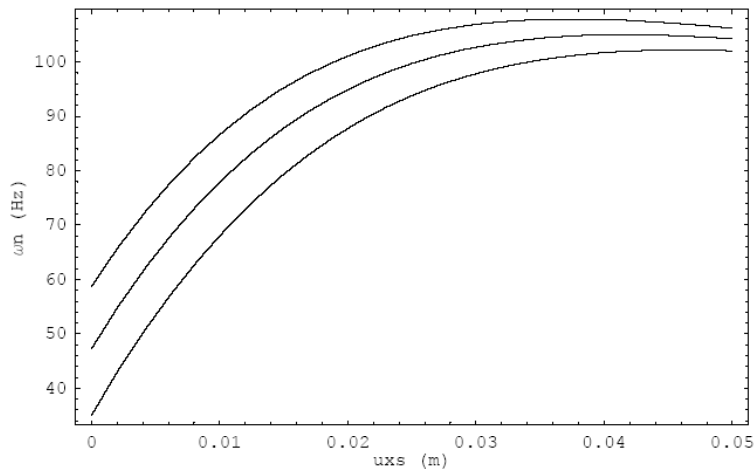
(* plot definitions in which u_{xs} ranges between 0 and 5 mm and u_p is assigned a particular value; in plot3 $u_p = 8$ mm, in plot31 $u_p = 11$ mm etc. *)

plot3 := Plot[fcn3[u_{xs} , .008], { u_{xs} , 0, .05}]

```

plot31 := Plot[fcn31[uxs, .011], {uxs, 0, .05}]
plot32 := Plot[fcn32[uxs, .014], {uxs, 0, .05}]
Show[plot3, plot31, plot32, Frame → True,
FrameLabel → {"uxs (m)", " $\omega_n$  (Hz)"}, PlotRange → All]

```



Out[1569]=

- Graphics -

In[1570]:=

(* results for the stiffness are shown below for the various input conditions shown with $u_{xs}=0$ and u_p varying as .008, .011, and .014. The values for u_p were chosen to maintain a similar stiffness term compared to the RXMR model (81 g $L_0=22$ mm) *)

s[0, 0.008]

s[0, 0.011]

s[0, 0.014]

Out[1570]=

25629.6

Out[1571]=

46274.7

Out[1572]=

70696.4

```
In[1573]:=
(* The following are calculations are for the resonant frequency
   using the defined functions with the values for  $u_x$  and  $u_p$  shown. *)

   $u_x = 0$ ;
  fcn3[ $u_x$ , .008]
  fcn31[ $u_x$ , .011]
  fcn32[ $u_x$ , .014]

Out[1574]=
  35.0462

Out[1575]=
  47.2764

Out[1576]=
  58.7306

In[1577]:=
   $u_x = .025$ ;
  fcn3[ $u_x$ , .008]
  fcn31[ $u_x$ , .011]
  fcn32[ $u_x$ , .014]

Out[1578]=
  93.8284

Out[1579]=
  99.7391

Out[1580]=
  104.836

In[1581]:=
   $u_x = .04$ ;
  fcn3[ $u_x$ , .008]
  fcn31[ $u_x$ , .011]
  fcn32[ $u_x$ , .014]

Out[1582]=
  101.729

Out[1583]=
  104.998

Out[1584]=
  107.825
```

(* This sheet shows the variation of frequency with changes to two adjustable parameters u_{xs} and u_p . The stiffness s is defined as a function of u_p and u_{xs} : $s = s(u_{xs}, u_p)$. In this treatment the goal is to demonstrate the expected tuning range of the RXMR in its current configuration. The value for u_p is changed to report similar values to experimental data. The range of u_{xs} is enough to capture the peak at about 45 degrees. *)

Clear[u_p , u_{xs} , L_0 , d_{31} , w , s_{11} , ϵ , s , ω_n , h , f_{cn3} , f_{cn31} , f_{cn32} , m]

(* Define the stiffness s as a function of u_{xs} and u_p *)

$$s[u_p, u_{xs}] := \frac{4wh}{s_{11}} \left(\left(-(u_p + u_{xs})^2 \sqrt{L_0^2 + (u_p + u_{xs})^2} + L_0^2 \left(\sqrt{L_0^2 + u_{xs}^2} - \sqrt{L_0^2 + (u_p + u_{xs})^2} \right) \right) / \left(\sqrt{L_0^2 + u_{xs}^2} (L_0^2 + (u_p + u_{xs})^2)^{3/2} \right) \right)$$

(* Assign values to the terms in the equation. These are the values from "1st 119 micron film excel spreadsheet" *)

$m = .0823$;
 $Rm = 1.36$;
 $s_{11} = 3.65 \cdot 10^{-10}$;
 $d_{31} = 2.3 \cdot 10^{-11}$;
 $\epsilon_3 = 1.1 \cdot 10^{-10}$;
 $L_0 = .022$;
 $w = .024$;
 $h = 1.19 \cdot 10^{-4}$;

(* f_{cn3} , f_{cn31} , and f_{cn32} are calculations for natural frequency defined as functions of u_{xs} and u_p *)

$$f_{cn3}[u_{xs}, u_p] := \frac{1}{2\pi} \sqrt{\frac{s[u_p, u_{xs}]}{m}}$$

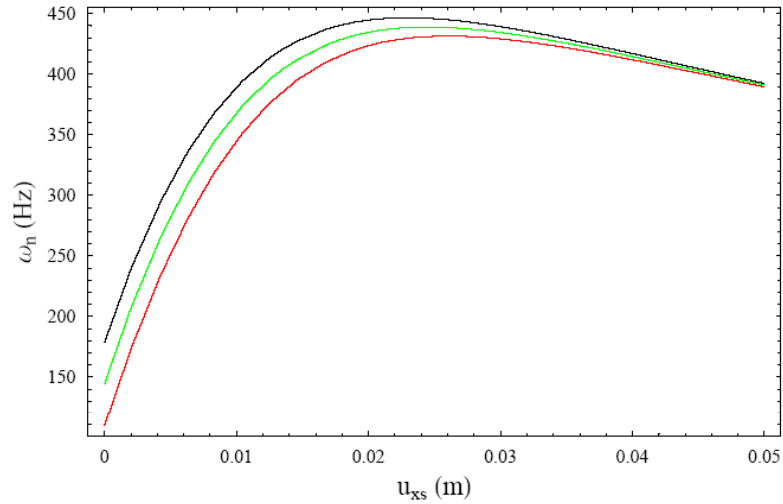
$$f_{cn31}[u_{xs}, u_p] := \frac{1}{2\pi} \sqrt{\frac{s[u_p, u_{xs}]}{m}}$$

$$f_{cn32}[u_{xs}, u_p] := \frac{1}{2\pi} \sqrt{\frac{s[u_p, u_{xs}]}{m}}$$

(* plot definitions in which u_{xs} ranges between 0 and 5 mm and u_p is assigned a particular value; in plot3 $u_p=3$ mm, in plot31 $u_p=4$ mm etc. *)

$plot3 := Plot[f_{cn3}[u_{xs}, .003], \{u_{xs}, 0, .05\}, PlotStyle \rightarrow \{RGBColor[1, 0, 0]\}$
 $plot31 := Plot[f_{cn31}[u_{xs}, .004], \{u_{xs}, 0, .05\}, PlotStyle \rightarrow \{RGBColor[0, 1, 0]\}$
 $plot32 := Plot[f_{cn32}[u_{xs}, .005], \{u_{xs}, 0, .05\}$
 $Show[plot3, plot31, plot32, Frame \rightarrow True,$

```
FrameLabel -> {FontForm[" $u_{xs}$  (m)", {"Times", 14}], FontForm[" $\omega_n$  (Hz)", {"Times", 14}]},
PlotRange -> All]
```



- Graphics -

(* results for the stiffness are shown below for the various input conditions shown with $u_{xs}=0$ and u_p varying as .003, .004, and .005. The values for u_p were chosen to be similar to experimental data form "1st 119 micron" experiment *)

```
s[0, 0.003]
s[0, 0.004]
s[0, 0.005]
```

25733.4

44791.

68137.9

(* The following are calculations are for the resonant frequency
using the defined functions with the values for u_{xs} and up shown. *)

```
uxs = 0;  
fcn3[uxs, .003]  
fcn31[uxs, .004]  
fcn32[uxs, .005]
```

109.249

144.39

178.494

```
uxs = .01;  
fcn3[uxs, .003]  
fcn31[uxs, .004]  
fcn32[uxs, .005]
```

345.269

368.355

389.425

```
uxs = .02;  
fcn3[uxs, .003]  
fcn31[uxs, .004]  
fcn32[uxs, .005]
```

423.54

434.623

444.692

A 2.6 Variation of ω_n with u_p variation of u_p .nb

Variation of ω_n with u_p variation of u_p .nb

1

```
(* This sheet shows the variation of frequency with changes to two adjustable
parameters uxs and up. The stiffness s is defined as a function of up and uxs: s =
s (uxs,up). In this treatment the goal is to demonstrate the expected
tuning range of the RXMR in its current configuration. This version
sweeps up while uxs is increased incrementally. The value for up
is changed to report similar values to experimental data. The range
of uxs is enough to capture the peak at about 45 degrees. *)
```

```
Clear[up, uxs, L0, d31, w, s11, ε, s, ωn, h, fcn3, fcn31, fcn32, m]
```

```
(* Define the stiffness s as a function of uxs and up *)
```

```
s[up_, uxs_] :=
-  $\frac{4wh}{s11} \left( \left( - (up + uxs)^2 \sqrt{L0^2 + (up + uxs)^2} + L0^2 \left( \sqrt{L0^2 + uxs^2} - \sqrt{L0^2 + (up + uxs)^2} \right) \right) \right) /$ 
 $\left( \sqrt{L0^2 + uxs^2} (L0^2 + (up + uxs)^2)^{3/2} \right)$ 
```

```
(* Assign values to the terms in the equation. These
are the values from "1st 119 micron film excel spreadsheet" *)
```

```
m = .0823;
Rm = 1.36;
s11 = 3.65 10-10;
d31 = 2.3 10-11;
ε3 = 1.1 10-10;
L0 = .022;
w = .024;
h = 1.19 10-4;
```

```
(* fcn3, fcn31, and fcn32 are calculations for
natural frequency defined as functions of uxs and up *)
```

```
fcn3[uxs_, up_] :=  $\frac{1}{2\pi} \sqrt{\frac{s[up, uxs]}{m}}$ 
```

```
fcn31[uxs_, up_] :=  $\frac{1}{2\pi} \sqrt{\frac{s[up, uxs]}{m}}$ 
```

```
fcn32[uxs_, up_] :=  $\frac{1}{2\pi} \sqrt{\frac{s[up, uxs]}{m}}$ 
```

```
(* plot definitions in which uxs ranges between 0 and 5 mm and up is
assigned a particular value; in plot3 up=3mm, in plot31 up=4 mm etc. *)
```

```
$DefaultFont = {"Times", 10}
```

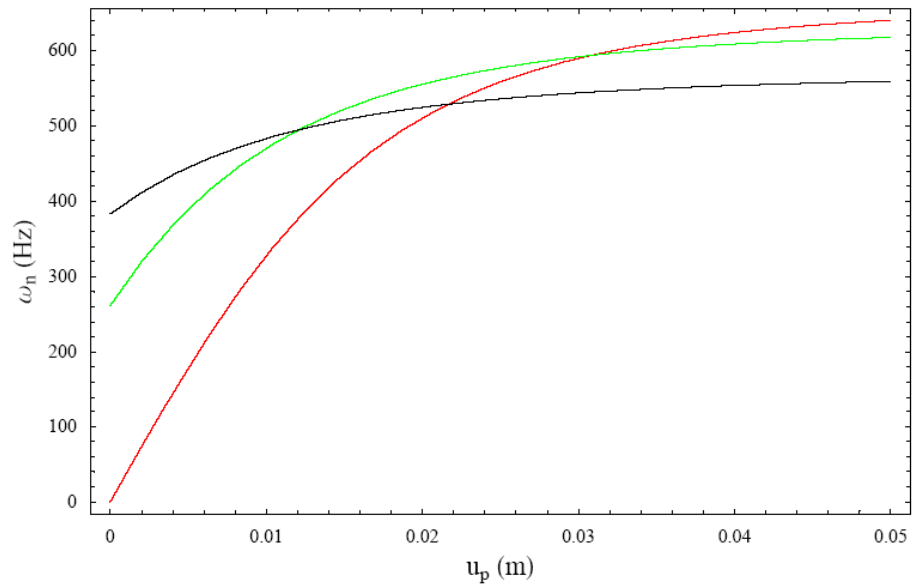
```
plot3 := Plot[fcn3[0, up], {up, 0, .05}, PlotStyle -> {RGBColor[1, 0, 0]}
```

```
plot31 := Plot[fcn31[.010, up], {up, 0, .05}, PlotStyle -> {RGBColor[0, 1, 0]}
```

```
plot32 := Plot[fcn32[.020, up], {up, 0, .05}]
```

```
Show[plot3, plot31, plot32, Frame → True,
  FrameLabel → {FontForm[" $u_p$  (m)", {"Times", 14}], FontForm[" $\omega_n$  (Hz)", {"Times", 14}]},
  PlotRange → All]
```

```
{Times, 10}
```



```
- Graphics -
```

```
(* results for the stiffness are shown below for the
  various input conditions shown with  $u_{xs}=0$  and  $u_p$  varying as .003,
  .004, and .005. The values for  $u_p$  were chosen to be similar to
  experimental data form "1st 119 micron" experiment *)
```

```
s[0, 0.003]
s[0, 0.004]
s[0, 0.005]
```

```
25733.4
```

```
44791.
```

```
68137.9
```

(* The following are calculations are for the resonant frequency
using the defined functions with the values for u_x and u_p shown. *)

```
uxs = 0;  
fcn3[uxs, .003]  
fcn31[uxs, .004]  
fcn32[uxs, .005]
```

109.249

144.39

178.494

```
uxs = .01;  
fcn3[uxs, .003]  
fcn31[uxs, .004]  
fcn32[uxs, .005]
```

345.269

368.355

389.425

```
uxs = .02;  
fcn3[uxs, .003]  
fcn31[uxs, .004]  
fcn32[uxs, .005]
```

423.54

434.623

444.692

A3 Composite Material Thickness Derivation

Derivation for composite substrate: PZT on brass foil for example.

Mechanical Portion

h_a is the thickness of the piezo electric (active) material.

h_c is the thickness of the composite structure.

$s_{11_c}^E$ is the compliance of the composite structure.

Starting with

$$S_1 = d_{31} E_3 + s_{11_c}^E T_1$$

and

$$T_1 = \frac{N_x}{wh_c}$$

where h_c is the thickness of the composite structure.

Write the strain equation converting field to voltage realizing that the passive foil layer has $d_{31}=0$:

$$S_1 \int_0^{h_c} dz = d_{31_{active}} \int_{h_c-h_a}^{h_c} E_3 dz + d_{31_{passive}} \int_0^{h_a} E_3 dz + s_{11_c}^E T_1 \int_0^{h_c} dz$$

Results in

$$S_1 h_c = -d_{31} V + s_{11_c}^E T_1 h_c$$

Using the general form of the derivation from the JSV submission the tension in a film element is

$$N_x = \frac{wh_c}{s_{11_c}^E} \left(\frac{\Delta L}{L_o} + \frac{d_{31} V}{h_c} \right)$$

Using the dynamic Taylor approximation for $\cos\alpha \approx \Delta L/L_o$ the vertical force for the top and bottom film are written

$$approxfortop = \frac{wh_c u_p}{s_{11c}^E L_o} \left(1 - \frac{1}{\sqrt{1 + \left(\frac{u_p}{L_o}\right)^2}} \right) - \frac{wh_c}{s_{11c}^E L_o} \frac{1}{\left(1 + \left(\frac{u_p}{L_o}\right)^2 \right)^{3/2}}$$

$$approxforbottom = -\frac{wh_c u_p}{s_{11c}^E L_o} \left(1 - \frac{1}{\sqrt{1 + \left(\frac{u_p}{L_o}\right)^2}} \right) - \frac{wh_c}{s_{11c}^E L_o} \frac{1}{\left(1 + \left(\frac{u_p}{L_o}\right)^2 \right)^{3/2}}$$

From the total force equation

$$F_T = 2N_x^+ \cos \alpha + 2N_x^- \cos \alpha$$

Write the force equation using the approximations above recognizing that the first term in both approximation equations will cancel:

$$F_T = -4 \frac{wh_c}{s_{11c}^E L_o} \left(1 - \frac{1}{\left(1 + \left(\frac{u_p}{L_o}\right)^2 \right)^{3/2}} \right) \Delta u - 2 \frac{d_{31} w u_p}{s_{11c}^E L_o} \frac{1}{\sqrt{1 + \left(\frac{u_p}{L_o}\right)^2}} (\Delta V_U - \Delta V_L)$$

From this define the coefficients of the terms as:

$$s = 4 \frac{wh_c}{s_{11c}^E L_o} \left(1 - \frac{1}{\left(1 + \left(\frac{u_p}{L_o}\right)^2 \right)^{3/2}} \right) \text{ and } \Psi = 2 \frac{d_{31} w u_p}{s_{11c}^E L_o} \frac{1}{\sqrt{1 + \left(\frac{u_p}{L_o}\right)^2}}$$

Electrical Portion

From piezo constitutive equations solve for stress T:

$$T_1 = \frac{S_1 - d_{31}E_3}{s_{11_c}^E}$$

Sub into D_3 equation and write

$$D_3 = \varepsilon_3^T E_3 + d_{31} \left(\frac{S_1 - d_{31}E_3}{s_{11_c}^E} \right)$$

$$D_3 = \varepsilon_3^T E_3 + \frac{d_{31}S_1}{s_{11_c}^E} - \frac{d_{31}^2 E_3}{s_{11_c}^E L_o}$$

Collecting terms

$$D_3 = \varepsilon_3^T \left(1 - \frac{d_{31}^2}{\varepsilon_3^T s_{11_c}^E} \right) E_3 + \frac{d_{31}}{s_{11_c}^E} \frac{\Delta L}{L_o}$$

Convert field to voltage

$$D_3 \int_0^{h_a} dz = \varepsilon_3^T \left(1 - \frac{d_{31}^2}{\varepsilon_3^T s_{11_c}^E} \right) \int_0^{h_a} E_3 dz + \frac{\Delta L}{L_o} \frac{d_{31}}{s_{11_c}^E} \int_0^{h_a} dz$$

Limits are of the active piezoelectric material only.

This results in

$$D_3 h_a = \varepsilon_3^T \left(1 - \frac{d_{31}^2}{\varepsilon_3^T s_{11_c}^E} \right) V + \frac{\Delta L}{L_o} \frac{d_{31}}{s_{11_c}^E} h_a$$

Now integrate over a single electrode

$$D_3 h_a \int_0^{L_o} \int_0^w dx dy = \varepsilon_3^T \left(1 - \frac{d_{31}^2}{\varepsilon_3^T s_{11_c}^E} \right) V \int_0^{L_o} \int_0^w dx dy + \frac{\Delta L}{L_o} \frac{d_{31}}{s_{11_c}^E} h_a \int_0^{L_o} \int_0^w dx dy$$

Which results in the displacement equation written as

$$D_3 h_a L_o w = \varepsilon_3^T \left(1 - \frac{d_{31}^2}{\varepsilon_3^T s_{11_c}^E} \right) L_o w V + \frac{\Delta L}{L_o} \frac{d_{31}}{s_{11_c}^E} L_o w h_a$$

Substituting the approximation for $\Delta L/L_o$

$$\frac{\Delta L}{L_o} = - \frac{u_p \Delta u}{L_o^2 \sqrt{1 + \left(\frac{u_p}{L_o} \right)^2}}$$

Results in

$$D_3 h_a L_o w = \varepsilon_3^T \left(1 - \frac{d_{31}^2}{\varepsilon_3^T s_{11c}^E} \right) L_o w V - \frac{u_p \Delta u}{L_o^2 \sqrt{1 + \left(\frac{u_p}{L_o} \right)^2}} \frac{d_{31}}{s_{11c}^E} L_o w h_a$$

Now equate $wL_o D_3$ to the total free charge attracted to the electrode when connected in series with the lower film, divide through by h_a and multiply by 2 for the two elements then:

$$D_3 h_a L_o w = 2 \varepsilon_3^T L_o w \left(1 - \frac{d_{31}^2}{\varepsilon_3^T s_{11c}^E} \right) V - 2 \frac{u_p L_o w h_a}{L_o^2 \sqrt{1 + \left(\frac{u_p}{L_o} \right)^2}} \frac{d_{31}}{s_{11c}^E} \Delta u$$

$$-Q_U = -\bar{C} \Delta V_U + \Psi \Delta u$$

Define the coefficients as

$$-\bar{C} = 2 \frac{\varepsilon_3^T L_o w}{h_a} \left(1 - \frac{d_{31}^2}{\varepsilon_3^T s_{11c}^E} \right)$$

And

$$\Psi = -2 \frac{u_p w}{L_o \sqrt{1 + \left(\frac{u_p}{L_o} \right)^2}} \frac{d_{31}}{s_{11c}^E}$$

Where

$$C_o = \frac{\bar{C}}{2} = \frac{\varepsilon_3^T L_o w}{h_a} \left(1 - \frac{d_{31}^2}{\varepsilon_3^T s_{11c}^E} \right)$$

A4 Uncertainty Analysis

A4.1 Uncertainty analysis for s and Ψ in the regular model using all terms

Stiffness and psi uncertainty all terms.nb

1

- **This sheet show the regular model error analysis for the stiffness and electromechanical coupling terms s and ψ . The analysis contains all the geometric and materials terms.**

```
Clear[w, h, s11, Lo, up, d31, s, psi, us, upsi, Δw, ΔLo, Δup, Δs11, Δd31, Δh]
```

- **Define the equations for s and ψ .**

$$s := 4 \frac{wh}{s_{11} L_0} \left(1 - \frac{1}{\left(1 + \left(\frac{up}{L_0}\right)^2\right)^{\frac{3}{2}}} \right)$$

$$\psi := 2 \frac{d_{31} w up}{s_{11} L_0} \frac{1}{\left(1 + \left(\frac{up}{L_0}\right)^2\right)^{\frac{1}{2}}}$$

Uncertainty is calculated using the following form

$$u^2 = \left(\frac{df}{dx} \Delta x \right)^2 + \left(\frac{df}{dy} \Delta y \right)^2 + \left(\frac{df}{dz} \Delta z \right)^2 + \dots$$

where $f = f(x, y, z)$ is the function composed of variables x, y, z and u is the uncertainty.

Write the uncertainty equations for s and ψ :

$$us = ((D[s, w] \Delta w)^2 + (D[s, h] \Delta h)^2 + (D[s, s11] \Delta s11)^2 + (D[s, Lo] \Delta Lo)^2 + (D[s, up] \Delta up)^2)^{\frac{1}{2}}$$

$$\sqrt{\left(\frac{16 \left(1 - \frac{1}{\left(1 + \frac{up^2}{Lo^2} \right)^{3/2}} \right)^2 w^2 \Delta h^2}{Lo^2 s11^2} + \left(-\frac{12 h up^2 w}{Lo^4 s11 \left(1 + \frac{up^2}{Lo^2} \right)^{5/2}} - \frac{4 h \left(1 - \frac{1}{\left(1 + \frac{up^2}{Lo^2} \right)^{3/2}} \right) w}{Lo^2 s11} \right)^2 \Delta Lo^2 + \frac{16 h^2 \left(1 - \frac{1}{\left(1 + \frac{up^2}{Lo^2} \right)^{3/2}} \right)^2 w^2 \Delta s11^2}{Lo^2 s11^4} + \frac{144 h^2 up^2 w^2 \Delta up^2}{Lo^6 s11^2 \left(1 + \frac{up^2}{Lo^2} \right)^5} + \frac{16 h^2 \left(1 - \frac{1}{\left(1 + \frac{up^2}{Lo^2} \right)^{3/2}} \right)^2 \Delta w^2}{Lo^2 s11^2} \right)}$$

$$upsi = ((D[\psi, d31] \Delta d31)^2 + (D[\psi, w] \Delta w)^2 + (D[\psi, up] \Delta up)^2 + (D[\psi, s11] \Delta s11)^2 + (D[\psi, Lo] \Delta Lo)^2 + (D[\psi, up] \Delta up)^2)^{\frac{1}{2}}$$

$$\sqrt{\left(\frac{4 up^2 w^2 \Delta d31^2}{Lo^2 s11^2 \left(1 + \frac{up^2}{Lo^2} \right)} + \left(\frac{2 d31 up^3 w}{Lo^4 s11 \left(1 + \frac{up^2}{Lo^2} \right)^{3/2}} - \frac{2 d31 up w}{Lo^2 s11 \sqrt{1 + \frac{up^2}{Lo^2}}} \right)^2 \Delta Lo^2 + \frac{4 d31^2 up^2 w^2 \Delta s11^2}{Lo^2 s11^4 \left(1 + \frac{up^2}{Lo^2} \right)} + 2 \left(-\frac{2 d31 up^2 w}{Lo^3 s11 \left(1 + \frac{up^2}{Lo^2} \right)^{3/2}} + \frac{2 d31 w}{Lo s11 \sqrt{1 + \frac{up^2}{Lo^2}}} \right)^2 \Delta up^2 + \frac{4 d31^2 up^2 \Delta w^2}{Lo^2 s11^2 \left(1 + \frac{up^2}{Lo^2} \right)} \right)}$$

■ **Input device measurements and values for variable uncertainties:**

```
w = .024;  
Δw = .0005 ; (* m *)  
Lo = .022;  
ΔLo = .0001 ; (* m *)  
h = 1.19 10-4;  
Δh = .00002 ; (* m *)  
up = 0.00359;  
Δup = .0002 ; (* m *)  
s11 = 3.65 10-10;  
Δs11 = 1 10-10 ; (* m2/N *)  
d31 = 2.3 10-11;  
Δd31 = 1 10-11 ; (* C/N *)
```

■ **Calculate uncertainties:**

us

18692.2

upsi

0.000253324

A4.2 Uncertainty analysis for s and Ψ in the regular model using all terms except d_{31}

Stiffness and psi uncertainty all terms except d31.nb

1

- This sheet show the regular model error analysis for the stiffness and electromechanical coupling terms s and ψ . The analysis contains all the geometric and materials terms except d_{31} .

```
Clear[w, h, s11, Lo, up, d31, s, psi, us, upsi, Δw, ΔLo, Δup, Δs11, Δd31, Δh]
```

- Define the equations for s and ψ .

$$s := 4 \frac{w h}{s_{11} L_0} \left(1 - \frac{1}{\left(1 + \left(\frac{u_p}{L_0} \right)^2 \right)^{\frac{3}{2}}} \right)$$

$$\psi := 2 \frac{d_{31} w u_p}{s_{11} L_0} \frac{1}{\left(1 + \left(\frac{u_p}{L_0} \right)^2 \right)^{\frac{1}{2}}}$$

■

Uncertainty is calculated using the following form

$$u^2 = \left(\frac{df}{dx} \Delta x \right)^2 + \left(\frac{df}{dy} \Delta y \right)^2 + \left(\frac{df}{dz} \Delta z \right)^2 + \dots$$

where $f = f(x, y, z)$ is the function composed of variables x, y, z and u is the uncertainty.

Write the uncertainty equations for s and ψ :

$$u_s = ((D[s, w] \Delta w)^2 + (D[s, h] \Delta h)^2 + (D[s, s11] \Delta s11)^2 + (D[s, Lo] \Delta Lo)^2 + (D[s, up] \Delta up)^2)^{\frac{1}{2}}$$

$$\sqrt{\left(\frac{16 \left(1 - \frac{1}{\left(1 + \frac{up^2}{Lo^2} \right)^{3/2}} \right)^2 w^2 \Delta h^2}{Lo^2 s11^2} + \left(-\frac{12 h up^2 w}{Lo^4 s11 \left(1 + \frac{up^2}{Lo^2} \right)^{5/2}} - \frac{4 h \left(1 - \frac{1}{\left(1 + \frac{up^2}{Lo^2} \right)^{3/2}} \right) w}{Lo^2 s11} \right)^2 \Delta Lo^2 + \frac{16 h^2 \left(1 - \frac{1}{\left(1 + \frac{up^2}{Lo^2} \right)^{3/2}} \right)^2 w^2 \Delta s11^2}{Lo^2 s11^4} + \frac{144 h^2 up^2 w^2 \Delta up^2}{Lo^6 s11^2 \left(1 + \frac{up^2}{Lo^2} \right)^5} + \frac{16 h^2 \left(1 - \frac{1}{\left(1 + \frac{up^2}{Lo^2} \right)^{3/2}} \right)^2 \Delta w^2}{Lo^2 s11^2} \right)}$$

$$u_\psi = ((D[\psi, w] \Delta w)^2 + (D[\psi, up] \Delta up)^2 + (D[\psi, s11] \Delta s11)^2 + (D[\psi, Lo] \Delta Lo)^2 + (D[\psi, up] \Delta up)^2)^{\frac{1}{2}}$$

$$\sqrt{\left(\left(\frac{2 d31 up^3 w}{Lo^4 s11 \left(1 + \frac{up^2}{Lo^2} \right)^{3/2}} - \frac{2 d31 up w}{Lo^2 s11 \sqrt{1 + \frac{up^2}{Lo^2}}} \right)^2 \Delta Lo^2 + \frac{4 d31^2 up^2 w^2 \Delta s11^2}{Lo^2 s11^4 \left(1 + \frac{up^2}{Lo^2} \right)} + 2 \left(-\frac{2 d31 up^2 w}{Lo^3 s11 \left(1 + \frac{up^2}{Lo^2} \right)^{3/2}} + \frac{2 d31 w}{Lo s11 \sqrt{1 + \frac{up^2}{Lo^2}}} \right)^2 \Delta up^2 + \frac{4 d31^2 up^2 \Delta w^2}{Lo^2 s11^2 \left(1 + \frac{up^2}{Lo^2} \right)} \right)}$$

■ **Input device measurements and values for variable uncertainties:**

```
w = .024;  
Δw = .0005 ; (* m *)  
Lo = .022;  
ΔLo = .0001 ; (* m *)  
h = 1.19 10-4;  
Δh = .00002 ; (* m *)  
up = 0.00359;  
Δup = .0002 ; (* m *)  
s11 = 3.65 10-10;  
Δs11 = 1 10-10 ; (* m2/N *)  
d31 = 2.3 10-11;  
Δd31 = 1 10-11 ; (* C/N *)
```

■ **Calculate uncertainties:**

```
us  
  
18692.2  
  
upsi  
  
0.000138984
```

A4.3 Uncertainty analysis for s and Ψ in the regular model using only geometry terms

■

This sheet show the regular model error analysis for the stiffness and electromechanical coupling terms s and ψ . The analysis contains only the geometric terms.

```
In[64]:= Clear[w, h, s11, Lo, up, d31, s, psi, us, upsi, Δw, ΔLo, Δup, Δs11, Δd31, Δh]
```

■

Define the equations for s and ψ .

```
In[65]:=
```

$$s := 4 \frac{w h}{s_{11} L_0} \left(1 - \frac{1}{\left(1 + \left(\frac{u_p}{L_0} \right)^2 \right)^{\frac{3}{2}}} \right)$$

$$\psi := 2 \frac{d_{31} w u_p}{s_{11} L_0} \frac{1}{\left(1 + \left(\frac{u_p}{L_0} \right)^2 \right)^{\frac{1}{2}}}$$

■

Uncertainty is calculated using the following form

$$u^2 = \left(\frac{df}{dx} \Delta x \right)^2 + \left(\frac{df}{dy} \Delta y \right)^2 + \left(\frac{df}{dz} \Delta z \right)^2 + \dots$$

where $f = f(x, y, z)$ is the function composed of variables x, y, z and u is the uncertainty.

Write the uncertainty equations for s and ψ :

In[67]:=

$$us = ((D[s, w] \Delta w)^2 + (D[s, h] \Delta h)^2 + (D[s, Lo] \Delta Lo)^2 + (D[s, up] \Delta up)^2)^{\frac{1}{2}}$$

$$Out[67]= \sqrt{\left(\frac{16 \left(1 - \frac{1}{\left(1 + \frac{up^2}{Lo^2} \right)^{3/2}} \right)^2 w^2 \Delta h^2}{Lo^2 s11^2} + \left(-\frac{12 h up^2 w}{Lo^4 s11 \left(1 + \frac{up^2}{Lo^2} \right)^{5/2}} - \frac{4 h \left(1 - \frac{1}{\left(1 + \frac{up^2}{Lo^2} \right)^{3/2}} \right) w}{Lo^2 s11} \right)^2 \Delta Lo^2 + \frac{144 h^2 up^2 w^2 \Delta up^2}{Lo^6 s11^2 \left(1 + \frac{up^2}{Lo^2} \right)^5} + \frac{16 h^2 \left(1 - \frac{1}{\left(1 + \frac{up^2}{Lo^2} \right)^{3/2}} \right)^2 \Delta w^2}{Lo^2 s11^2} \right)}$$

$$In[68]:= \psi psi = ((D[psi, w] \Delta w)^2 + (D[psi, up] \Delta up)^2 + (D[psi, Lo] \Delta Lo)^2 + (D[psi, up] \Delta up)^2)^{\frac{1}{2}}$$

$$Out[68]= \sqrt{\left(\left(\frac{2 d31 up^3 w}{Lo^4 s11 \left(1 + \frac{up^2}{Lo^2} \right)^{3/2}} - \frac{2 d31 up w}{Lo^2 s11 \sqrt{1 + \frac{up^2}{Lo^2}}} \right)^2 \Delta Lo^2 + 2 \left(-\frac{2 d31 up^2 w}{Lo^3 s11 \left(1 + \frac{up^2}{Lo^2} \right)^{3/2}} + \frac{2 d31 w}{Lo s11 \sqrt{1 + \frac{up^2}{Lo^2}}} \right)^2 \Delta up^2 + \frac{4 d31^2 up^2 \Delta w^2}{Lo^2 s11^2 \left(1 + \frac{up^2}{Lo^2} \right)} \right)}$$

■

Input device measurements and values for variable uncertainties:

```
In[69]:=
  w = .024;
  Δw = .0005 ; (* m *)
  Lo = .022;
  ΔLo = .0001 ; (* m *)
  h = 1.19 10-4;
  Δh = .00002 ; (* m *)
  up = 0.00359;
  Δup = .0002 ; (* m *)
  s11 = 3.65 10-10;
  Δs11 = 1 10-10 ; (* m2/N *)
  d31 = 2.3 10-11;
  Δd31 = 1 10-11 ; (* C/N *)
```

■

Calculate uncertainties:

```
In[79]:=
  us

Out[79]= 11064.3

In[80]:= upsi
Out[80]= 0.0000387964
```